Collective behavior of asperities as a model for friction and adhesion

Thesis by

Srivatsan Hulikal

In Partial Fulfillment of the Requirements
for the Degree of
Doctor of Philosophy

California Institute of Technology
Pasadena, California

2015
(Defended 14th April 2015)

ಸಂದೇಹವೀಕೃತಿಯೊಳಿನ್ನಿಲ್ಲವೆಂದಲ್ಲ
ಇಂದು ನಂಬಿಹುದೆ ಮುಂದೆಂದುಮೆಂದಲ್ಲ
ಕುಂದು ತೋರ್ದಂದದನು ತಿದ್ದಿಕೊಳೆ ಮನಸುಂಟು
ಇಂದಿಗೀ ಮತವುಚಿತ ಮಂಕುತಿಮ್ಮ
- ಡಿವಿಜಿ

To my parents and my sister for giving me an idyllic childhood

Acknowledgments

It gives me great pleasure to thank the many people who have made this thesis possible.

First, I would like to thank my advisors Prof. Nadia Lapusta and Prof. Kaushik Bhattacharya. One is lucky to find one good advisor, I consider myself doubly fortunate to have been able to work with two wonderful people. I was given all the freedom in the world to pursue anything that interested me. It is nice when you can just say "why?", and there is someone who is willing, patient, and even happy to answer your questions. Kaushik has been that person for me the last few years. His ability to distill a problem to its essence is remarkable, and I hope I have developed some of it over the years. A PhD is not without its hard times, and on many occasions when I have been despondent, meeting Nadia has helped me look at the situation in a more positive light. I hope I can carry the attitude for the rest of my life. I should also thank Nadia for asking me to smile more. Nadia, I promise to try.

I would like to thank Prof. Guruswami Ravichandran and Prof. Jose Andrade for serving on my committee and their suggestions with respect to this work. In spite of his busy schedule, Ravi has always found time to meet with me any time I asked. Thank you Ravi for your invaluable advice.

My life at Caltech has also given some of the best friendships which I hope will last the rest of my life. Ninja, B, Teja, Maha, Batuk, and Gopi, your friendship is one of the most valuable things I take away from Caltech, thank you guys. I will forever cherish the time I have spent with Jeff, Aubrie, Ellie, Cindy, Theva, Mythili, Navaneet, and Swetha. Most of the C++ and parallel programming I know, I learnt in a few sessions with Jeff. I cannot thank him enough for his patience and helpful nature. Mauri, Gal, Zubaer, thank you guys for being amazing friends and sharing your experience and advice with me, I miss walking periodically to your office and disturbing you. I would also like to thank all members of Kaushik's and Nadia's groups for being great colleagues. To Ashish, Subbu, Phanish, Naresh, Bharat, Piya, Mike Mello, Aaron, Gerry, Asghar, and many other friends who made my stay at Caltech enjoyable, thank you. I also want to thank Shalva, Shashi, Sanju, Sonu, Venkatesh, Prabha, Neha, Sahana, Raghunandan, Kiran, and Nishita for all their warmth and being my family in this country. I also thank Carolina, Leslie, Lynn, Cheryl, Chris, and Maria for all their help over the years.

Looking back, I realize I had an idyllic childhood, one that could have been straight out of an RK Narayan book. I find it hard to even imagine how it could have been better. For this and their unwavering love and support, I am very grateful to my parents, Sampath Kumaran and Sumithra, and my sister, Srilatha.

Contents

Abstract

Understanding friction and adhesion in static and sliding contact of surfaces is important in numerous physical phenomena and technological applications. Most surfaces are rough at the microscale, and thus the real area of contact is only a fraction of the nominal area. The macroscopic frictional and adhesive response is determined by the collective behavior of the population of evolving and interacting microscopic contacts. This collective behavior can be very different from the behavior of individual contacts. It is thus important to understand how the macroscopic response emerges from the microscopic one.

In this thesis, we develop a theoretical and computational framework to study the collective behavior. Our philosophy is to assume a simple behavior of a single asperity and study the collective response of an ensemble. Our work bridges the existing well-developed studies of single asperities with phenomenological laws that describe macroscopic rate-and-state behavior of frictional interfaces. We find that many aspects of the macroscopic behavior are robust with respect to the microscopic response. This explains why qualitatively similar frictional features are seen for a diverse range of materials.

We first show that the collective response of an ensemble of one-dimensional independent viscoelastic elements interacting through a mean field reproduces many qualitative features of static and sliding friction evolution. The resulting macroscopic behavior is different from the microscopic one: for example, even if each contact is velocity-strengthening, the macroscopic behavior can be velocity-weakening. The framework is then extended to incorporate three-dimensional rough surfaces, long-range elastic interactions between contacts, and time-dependent material behaviors such as viscoelasticity and viscoplasticity. Interestingly, the mean field behavior dominates and the elastic interactions, though important from a quantitative perspective, do not change the qualitative macroscopic response. Finally, we examine the effect of adhesion on the frictional response as well as develop a force threshold model for adhesion and mode I interfacial cracks.

Chapter 1

Introduction

1.1 Motivation and background

1.1.1 Motivation

Friction is ubiquitous: it allows us to walk and drive, and it plays a key role in the working of many machines and technologies. The history of humankind is closely intervowen with the progress of tribology. Fire, a significant discovery in the evolution of humans, was one of our ancestors' first experiments in tribochemistry. The making of tools, another milestone that sets us apart from other species, started as experiments with wear. In more recent times, the early civilizations also understood the significance of tribology. For example, during the Egyptian civilization, lubricants were used to reduce friction in transporting large stone blocks [1].

In the 18th and 19th centuries, the main impetus driving the advances in tribology was the industrial revolution, with knowledge from tribology being used in the development of better bearings and other machine tools. In the 20th and 21st centuries, tribology has found numerous applications in diverse fields including engineering, biology, and geology [2, 3].

At small length scales, the ratio of surface area to volume being large, surface forces play a dominant role. With advances in micro and nano fabrication techniques, development of small scale technologies like MEMS, NEMS and magnetic disk drives depends on our understanding of the surface forces at these scales [4, 5, 6]. For a discussion of some of the tribological issues in the design of micromotors, Digital Micro-mirror Devices, slider-disk interfaces in disk drives, nanoimprinting, and high density storage, see [7].

At the other end of the length scale spectrum, at very large length scales, various aspects of earthquakes are known to be sensitive to the frictional properties on faults [3, 8, 9, 10, 11, 12, 13].

While friction is desirable in many scenarios, it can also have undesired effects. In 1966, a report by Jost in Britian estimated that significant economic savings, of the order of 1% of the GNP, could be made through better triblogical practices [14] (this report also coined the word “Tribology”). Similar estimates have been made by other agencies since [15]. Thus, the study of friction potentially entails great economic benefits.

Another example of an application of the study of friction is tactile sensing. The goal here is to endow machines with a sense of touch [16, 17, 18, 19]. Think of the simple act of picking up an object. The forces applied should be large enough to overcome gravity but small enough to not cause any damage to the object. Apart from sophisticated feedback mechanisms, this also requires an understanding of the frictional forces involved based on the materials and the surface texture of the interacting objects (humans are apparently fairly efficient in doing this, applying between $10\% - 40\%$ more than the minimum force necessary [20]).

1.1.2 Overview of historical studies of friction

The scientific study of friction begins with the Italian polymath, Leonardo da Vinci. With his experiments, sliding objects on horizontal and inclined surfaces, and measuring forces using pulleys and weights, he made the following observations:

1. The frictional force is proportional to the normal force.
2. The frictional force is independent of the area of contact.

He also introduced the concept of friction coefficient as the ratio of the frictional and normal forces. It is interesting to consider Leonardo’s insight in the historical context.

In the 15th century, the concept of force had not developed sufficiently and the frictional and normal forces were not seen as two different manifestations of the same "force". Leonardo's work remained unnoticed and his findings were independently rediscovered by the 17th century French physicist Guillaume Amontons. The friction laws (1) and (2) stated above now bear his name.

Euler was the first to distinguish between static and sliding friction. He calculated that if the friction coefficient is μ (incidentally, he also introduced the symbol μ for the friction coefficient) and if a body placed on an inclined slope such that it is in equilibrium and if the slope is increased gradually, at some point, the equilibrium is disturbed, and after this the sliding speed should increase gradually with the slope. He observed, however, that the body moved faster than his predictions and concluded that the sliding friction must be smaller than the static friction.

The industrial revolution led to the advancement of studies in friction, lubrication, and wear. The French physicist Charles-Augustin de Coulomb, more well known for his work in electrostatics, made two important contributions to the study of friction. He observed that, the static friction coefficient is not a constant but increases with the time of contact. He also concluded, albeit wrongly, that the sliding friction coefficient is independent of the sliding speed. In the last few decades, there has been a resurgence in interest in friction which, accompanied by the development of new experimental techniques and increased computational power, has resulted in a number of studies of frictional properties of interfaces in different materials at different length and time scales. For a detailed history of tribology, see [1].

To study friction, it is important to first understand the contact of rough surfaces. The study of single asperity contact underlies many models of rough surface contact. The problem of contact of linear elastic parabolic surfaces was first solved by Hertz [21], apparently during his Chrismas vacation in 1880 [22], in his study of optical interference fringes between glass lenses. This has subsequently been extended to include other effects such as tangential loads, sliding, plasticity, viscoelasticity, adhesion, etc. (see [22] and references therein). The book Contact Mechanics by Prof. Johnson [22] is a good reference for problems in contact mechanics. For a review of single asperity contact, and some of the numerical methods that have been used in studying them, see [23]. For a review of single-asperity contact at the nanoscale, see [24].

The idea that the contact of rough surfaces can be approximated by the contact of a collection of spheres is an old and persistent one. The first appearance of this seems to be in the work of Bernard Forrest de Bélidor [1]. Assuming the spherical particles to be rigid, he calculated the force required to slide one collection of particles over another, and obtained a constant friction coefficient of 0.35. More than 200 years later, two different variations of this idea were proposed by Archard [25] and Greenwood and Williamson [26].

Archard proposed a hierarchical contact model in which a single elastic spherical contact is made of multiple contacts at a smaller scale, each of which is in turn made of even smaller contacts and so on [25]. He showed that as the number of levels in the hierarchy increases, the scaling between the macroscopic area and load approaches linearity (Amontons law). With advances in surface characterization techniques and the development of the idea of fractals, we know that rough surfaces do have features at many length scales and can be modeled as fractals. Several models of fractal rough surface contact have since been proposed [27, 28, 29] and the Archard model can be seen as a precursor to these.

In the Greenwood and Williamson model, each asperity is assumed to be spherical and a single contact is modeled according to Hertzian theory [26]. This is fitted within a statistical description of the rough surface. The macroscopic force and area are calculated as moments with respect to the probability distribution of heights. Greenwood and Williamson show that for an exponential height distribution, the force and area are exactly proportional, while for a Gaussian height distribution the linearity holds approximately over a large range of loads. In this model, interaction between contacts and the spatial structure of surface roughness are not considered.

Bowden and Tabor proposed that because of surface roughness, the real and nominal areas of contact are different and the real area is only a small fraction of the nominal area [30]. Since the applied load is sustained by this small area, the stresses at the contacts can be very high and cause yielding of the material. The frictional resistance is the force required to shear these contacts. Using this, they estimated the coefficient of friction as the ratio of shear strength of contacts to the indentation hardness of the material:

$$F_N = \sigma_c A_r, \quad F_S = \tau_c A_r, \quad \mu = F_S/F_N = \tau_c/\sigma_c, \tag{1.1}$$

where F_N and F_S are the macroscopic normal and shear loads, A_r is the real area of contact, σ_c is the indentation hardness, τ_c is the asperity shear strength, and μ is the friction coefficient. This model explains the Amontons laws since both the normal and the shear forces depend linearly on the real area of contact A_r and are independent of the nominal area. The above framework is helpful in explanining another feature of friction. The variation of the friction coefficient μ across many materials is fairly narrow and is usually of the order of 1 (one doesn't often see friction coefficients of the order of 0.01 or 100). Since $\mu = \tau_c/\sigma_c$, and materials with high shear strength usually have high indentation hardness, the ratio of these two does not vary too much.

1.1.3 Rate and state effects

The motivation for this thesis comes from the fascinating experimental discoveries of the last few decades. In the classical picture of friction, the static friction coefficient is a constant. Coulomb, however, had already observed that the static friction coefficient (μ_s) is not a constant but depends on how long surfaces are in contact before sliding begins [31]. He proposed an empirical power law to fit his experimental results. Classically, the sliding friction coefficient is also a constant that is independent of the sliding speed. In the last few decades, careful experiments have shown that the sliding friction coefficient (μ_k) depends on the sliding speed [32, 33, 9, 34, 35]. Furthermore, the frictional resistance depends not only on the current sliding velocity, but also on the velocity history of the system [33, 36, 9, 35]. The independence of the friction coefficients with respect to the normal force and the nominal area of contact has been observed to be a good approximation, except when the normal force varies rapidly

[37, 38].

Several studies have the observed the increase of μ_s with the time of contact. Rabinowicz [32], Richardson et al. [39] (Figure 1.1), and Dieterich [40] (Figure 1.2) observed a strengthening in their experiments on metals and rocks. In Dieterich's experiments [40], rocks were held at constant normal and shear forces for varying lengths of time before the shear force was suddenly increased to induce sliding. The coefficient of static friction was calculated as the ratio of the shear force required to initiate sliding to the applied normal force. μ_s was observed to increase logarithmically with the time of contact (Figure 1.2).

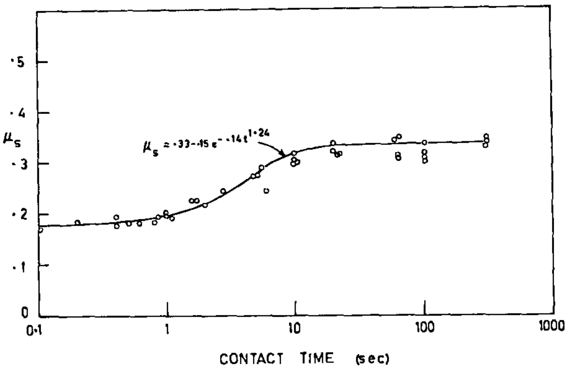

Figure 1.1: Evolution of friction coefficient of mild steel with time (reproduced with permission from [39]).

Dieterich proposed an empirical law to fit these results [33]:

$$\mu_s(t) = \mu_0 + A \log(Bt + 1), \tag{1.2}$$

where t is the time of stationary contact, and μ_0, A, and B are constants dependent on the two materials and surfaces across the interface. Typically, for rocks, μ_0 is 0.7-0.8, A is 0.01-0.02, and B is of the order of 1 second^{-1} [33].

Two physical processes are conjectured to be the origin of the strengthening. First, because of high stresses, creep at contacts might result in increased area of contact, leading to increased strength [41]. Second, even if the area of contact does not change, the strength of each contact might increase with time [30].

Experiments have shown that the sliding friction coefficient μ_k depends on the

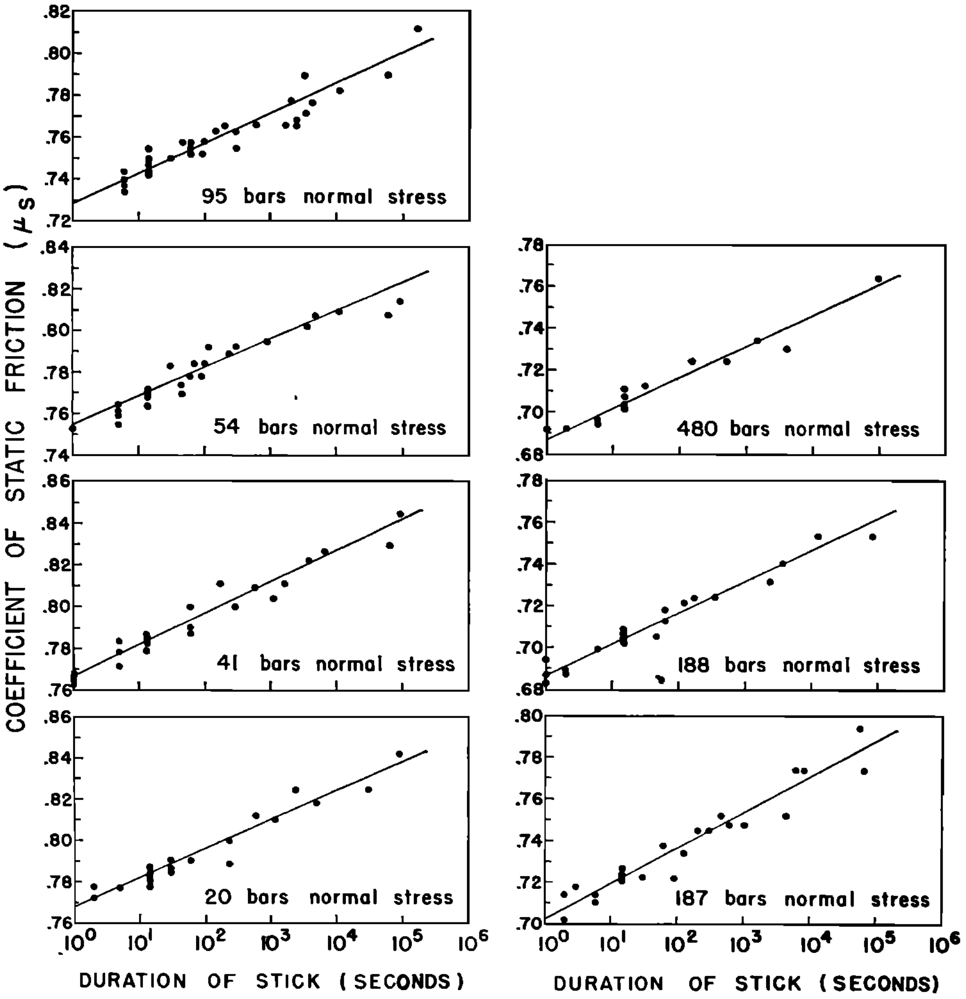

Figure 1.2: Evolution of the static friction coefficient with time at a constant normal force for quartz sandstone. Different panels correspond to different values of the normal force. Reproduced with permission from [40].

sliding velocity. In a common type of experiments called velocity jump tests, two surfaces are slid at a constant velocity till the system reaches steady state. Then, a step change in sliding velocity is induced and the shear force required to sustain this new velocity is monitored. Since the velocity is constant, by equilibrium, this force must equal the frictional force at the interface. This shear force divided by the applied normal force is the sliding friction coefficient. Experiments on different materials show that, with a jump in velocity, μ_k also jumps (called direct effect), and the jump is followed by an evolution to a new steady state corresponding to the new sliding velocity [41] (Figure 1.3). The evolution happens over a characteristic length scale, with the time scale of evolution to steady state being the ratio of the length scale to the sliding speed. This length scale, thought to be the slip necessary for the memory of the contacts to fade, is fairly independent of the sliding speed and the normal force but depends on the surface features [42]. Similar properties of the sliding friction coefficient have been found for sliding of thin granular layers [9]. It is interesting that for materials with very different properties, the frictional response is similar. For example, in Figure 1.3, a qualitatively similar behavior is seen in a rock (granite), polymers (lucite and teflon), glass, and wood.

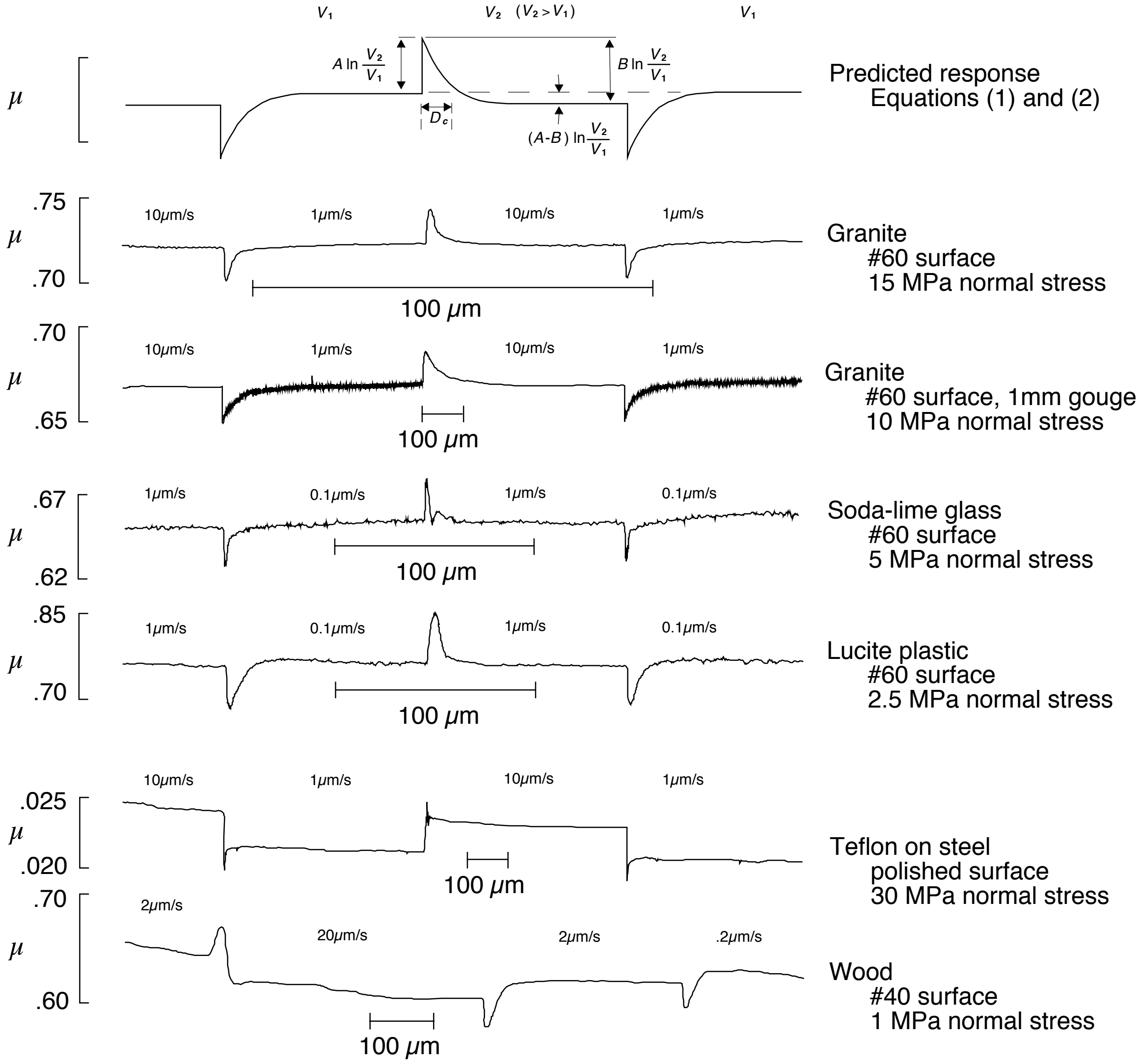

Figure 1.3: Evolution of sliding friction coefficient in velocity jump experiments on different materials. Reproduced with permission from [41].

A class of empirical laws called "rate and state" (RS) laws has been proposed to capture the above experimental observations [42, 36]. "Rate" here refers to the relative speed across the interface and "state" refers to one or more internal variables used to represent the memory in the system. One commonly used RS law with a single state variable takes the form:

$$\mu_k = \mu_0 + a\ln(\frac{v}{v^*}) + b\ln(\frac{v^*\theta}{D_c}), \tag{1.3}$$

where μ_k is the coefficient of friction, v is the sliding velocity, a, b, v^*, μ_0, and D_c are constants, and θ is an internal variable with dimensions of time. An evolution law is prescribed for the internal variable θ. Two well-known laws are the aging law,

$$\dot{\theta} = 1 - \frac{v\theta}{D_c}, \tag{1.4}$$

and the slip law,

$$\dot{\theta} = -\frac{v\theta}{D_c}\ln(\frac{v\theta}{D_c}). \tag{1.5}$$

In these equations, D_c is the characteristic length scale over which the coefficient of friction evolves to its steady state in the jump test. D_c is related to the roughness of the sliding surfaces and is of the order of microns for most engineering surfaces [42, 43]. At steady state, $\dot{\theta} = 0$, and from Equation (1.4) or (1.5), $\theta_{ss}(v) = D_c/v$. Using this in Equation (1.3), the steady state friction coefficient is given by,

$$\mu_{ss}(v) = const + (a-b)\ln(\frac{v}{v^*}). \tag{1.6}$$

If $a-b > 0$, the steady state friction coefficient increases with increasing sliding speed and if $a-b < 0$, the steady state friction coefficient decreases with increasing sliding speed. The two cases are known as velocity-strengthening and velocity-weakening, respectively.

The rate and state laws are used widely in simulations of earthquake phenomena and have been successful in reproducing many of the observed features of earthquakes

[8, 9, 10, 3, 11, 12, 13]. For example, it is known that the condition $a - b < 0$ is necessary for stick-slip [36, 44]. Along the San Andreas fault in California, there is a segment known as the Parkfield segment that is not locked but creeps with the Pacific and North American plates. Measurements of frictional properties of rocks there have shown that, because of the presence of certain minerals along the segment, $a - b$ is positive [45]. Thus, the stable sliding feature of this fault segment concurs with the prediction of the rate and state laws. Another example is the role of temperature dependence of $a - b$ in the depth cutoff of crustal earthquake activity [10].

Given the significance of the described experiments and the empirical laws, it is imperative that we understand how these features arise from a micromechanical perspective and be able to predict velocity-strengthening and velocity-weakening behavior based on the material and surface properties. Attempts have been made in this direction.

Two broad classes of models have been proposed to connect the asperity scale to the experimentally observed features of the macroscopic frictional behavior. The first is an extension of the Bowden and Tabor model. Several subsequent studies have incorporated the time and velocity dependence into that framework by representing the shear force at a contact as the product of the contact shear strength that depends on the sliding velocity and area that depends on the age of the contact [46, 47, 48, 49, 50]. The velocity dependence of the shear strength is attributed to an Arrhenius type activation mechanism while the time dependence of the area results from the creep behavior of the material. The proposed formulations have been able to match various frictional observations. In these models, it is assumed that each contact has the same shear and normal force per unit area and the evolution of the contact population is accounted for only by the evolution of the total contact area. As the total contact area changes, the normal force per unit area adjusts, providing the only interaction between the macroscale and the single asperity. Thus, this class of models is dominated by the behavior of single asperities and does not include the effects of the statistical properties of the contacting rough surfaces.

The other class of models is based on the Archard [25] and Greenwood-Williamson formulations [26]. Since the shear and normal forces are no longer proportional at the microscale for this case, the collective behavior of asperities becomes paramount in explaining the proportionality at the macroscale. These models are capable of explaining the basic observations of proportionality between the shear and normal forces at the macroscale and hence the constant static coefficient. They ignore, however, the spatial features of surface roughness and time-dependent behavior of single asperities. Thus they are unable to explain any evolution of the friction coefficient. This framework has been extended to study the time-dependent behavior of the contact area for the case of static contact [51, 52].

1.2 Overview of the thesis

1.2.1 Point of view

Most surfaces, even those that appear smooth, are rough at the microscale. When two such rough surfaces are pressed against each other, actual contact occurs only at a relatively small fraction – but yet a large number of peaks (asperities) of the surfaces.

When two surfaces are held in static contact or slid against each other, the population of contacts evolves: contacts grow, become smaller, and come into and go out of existence. Concomitantly, the forces on the asperities also evolve, not only because of the time-dependent behavior of each contact, but also because of the statistical properties of the rough contacting surfaces. This evolution at the microscale results in the evolution of friction, normal force, area of contact, etc., at the macroscale. This thesis examines the hypothesis that *it is the collective behavior of this evolving population of contacts that determines critical aspects of rate and state effects of friction.*

We develop a framework where the interaction between two solid surfaces is represented as that between a surface with a collection of discrete deformable elements (representing asperities) and one that is rigid (Figure 1.4). In order to focus on the collective behavior, we assume simple elastic and inelastic constitutive relations for the individual elements. Various observed rate and state aspects of friction that are absent in the microscale emerge as a result of the collective behavior. For example, even if individual asperities have velocity-strengthening local friction (higher resistance when sliding faster), the macroscale behavior can be velocity weakening (lower resistance when sliding faster). Further, many of these features are generic, and we believe that this is the reason they are observed in a wide variety of materials under a range of conditions.

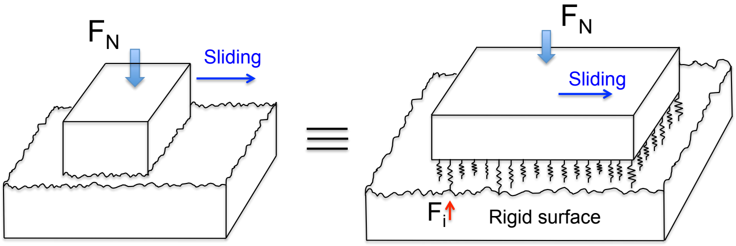

Figure 1.4: Contact of two rough surfaces, one of the rough surfaces is approximated by a set of discrete elements, the other surface is assumed to be rigid.

Our framework also enables us to examine many questions about the collective behavior. One question we answer is the role of elastic interactions between contacts. Contacts interact in two ways, the first is through a mean-field (the dilatation or separation between the surfaces) and the second is through the long-range elastic interactions. We find that within our model, the first is far more important than the second. This has important implications. It follows that relatively simple models with mean-field interactions are sufficient to understand various qualitative aspects of frictional behavior. In other words, the detailed shape and stress distribution of asperities may be less important than the overall statistics.

Existing studies of rate and state behavior do not consider the spatial structure of roughness. Since the sliding behavior is inextricably linked to spatial roughness correlations, these studies are confined to static contact. We present, as far as we know, the first sliding simulations of three-dimensional rough surfaces with long-range elastic interactions. We are thus able to explore the entire rate-and-state frictional response from the perspective of collective asperity behavior.

The approach we propose provides a bridge between existing well-developed studies of single asperities with phenomenological laws that describe macroscopic rate-and-state behavior of frictional interfaces.

1.2.2 Outline of the thesis

Chapter 2 examines the collective behavior of an ensemble of one-dimensional viscoelastic elements in contact with a rough rigid surface interacting through a mean field. The state of the system at any instant is described by a probability distribution of normal forces experienced by the elements in the ensemble. The time, velocity, and history dependence of frictional properties at the macroscale are a manifestation of the evolution of the probability density. Consequently, the behavior at the macroscale can be very different from the behavior of single asperities at the microscale. For example, even if individual asperities have velocity-strengthening local friction (higher resistance when sliding faster), the macroscale behavior can be velocity weakening (lower resistance when sliding faster). Many qualitative features of rate-and-state frictional behavior emerge from the collective behavior of the elements.

Chapter 3 makes an important step towards a more realistic representation of the physical system. The independent viscoelastic elements of Chapter 2 are supplemented with spatial structure by generating three-dimensional rough surfaces. Constitutive equations based on elasticity solutions that include long-range elastic interactions are derived. The goal of the chapter is to study the role of surface roughness, viscoelastic material properties, and the long-range elastic interactions in determining macroscopic friction. Many qualitative aspects of macroscopic friction are determined by the viscoelastic properties and the surface roughness. The long-range interactions, though important from a quantitative perspective, are dominated by the mean-field interactions and do not change the qualitative behavior.

Chapter 4 extends the model of Chapter 3 to include viscoplastic material behavior. Simulations show that the qualitative features of friction evolution are robust to the assumptions of the underlying time-dependent behavior. This hints that the reason many materials show similar macroscopic frictional behavior is the minimal restriction it places on the microscopic behavior.

Effects of adhesion can be important, especially at small length scales. In Chapter 5, a framework to incorporate the adhesive interactions is presented. Many aspects of rough surface adhesion and effects of adhesion on friction are discussed.

Chapter 6 develops a threshold force based model for adhesive contact of surfaces. A scaling relation that is very suggestive of linear elastic fracture mechanics is discovered. The model can also be used to study mode I interfacial cracks.

Chapter 7 provides a summary of the thesis and suggests some avenues for future work.

Chapter 2

Collective behavior of independent viscoelastic asperities interacting through a mean field

In this chapter, we propose a statistical model for static and sliding friction between rough surfaces. Approximating the contact between rough surfaces by the contact of an ensemble of one-dimensional viscoelastic elements with a rough rigid surface interacting through a mean field, we study the collective behavior of the elements. We find that collective response of the contacts can lead to macroscopic behavior that is very different from the microscopic behavior. Specifically, various observed features of friction emerge as collective phenomena, without postulating them directly at the microscale. We discuss how parameters in our model can be related to material and surface properties of the contacting surfaces. We compare our results to commonly used rate and state phenomenological models, and propose a new interpretation of the state variable.

This chapter is based on our paper [53].

2.1 Basic ingredients

The ingredients of our model are a constitutive description of single asperities at the microscale, and a stochastic characterization of rough surfaces. We now describe these in detail.

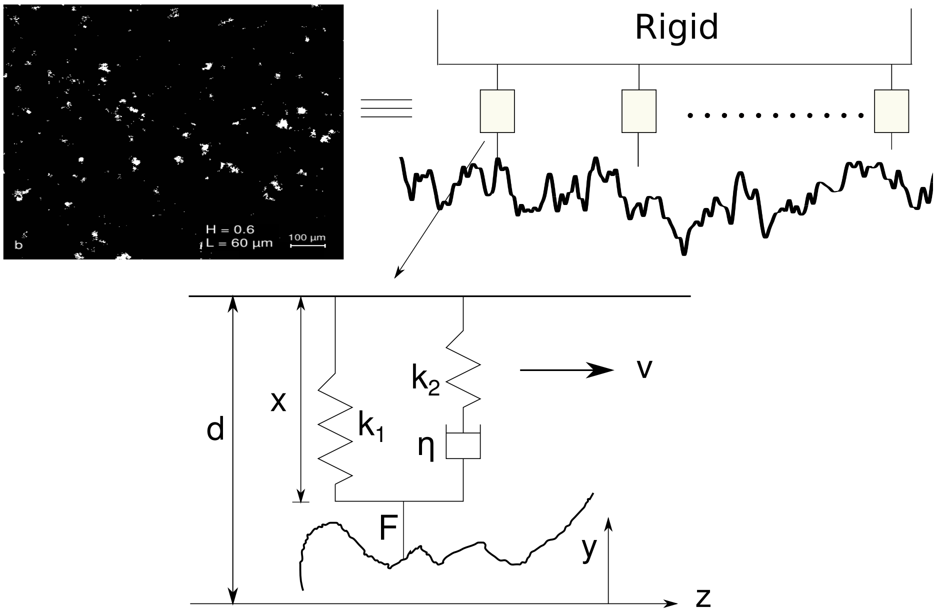

Figure 2.1: (Top left) Microscale image of actual contacts (white spots) between two rough surfaces (adapted with permission from [54]). The contacts form at the peaks (asperities) of the surfaces. (Top right) We model the system as an ensemble of one-dimensional elements in contact with a rigid rough surface. (Bottom) Each asperity is represented by a viscoelastic spring-dashpot element.

2.1.1 Single asperity

The behavior of an asperity depends on various factors, such as material properties, local stresses, sliding speed, etc. As a first step, we model asperities as being viscoelastic, using a spring-dashpot system known as a Standard Linear Solid (SLS, see Figure 2.1). An SLS consists of a spring in parallel with a spring and dashpot in series. The equation for the evolution of the force F on an SLS as a function of its length and the rate of change of its length is:

$$\dot{F} = (k_1 + k_2)\dot{x} - \frac{k_2}{\eta}F + \frac{k_1 k_2}{\eta}(x - x^0), \tag{2.1}$$

where k_1, k_2 are the stiffnesses of springs 1 and 2, respectively, η is the viscosity of the dashpot, x, x^0 are the current and undeformed lengths of spring 1, and dot denotes the time derivative. An asperity can be in two states, in contact or out of contact with the surface it slides on. When in contact, its length evolution is known and the force evolution can be calculated using Equation (2.1). When out of contact, the force on the asperity is zero and, setting $F = 0$ and $\dot{F} = 0$ in the Equation (2.1), the evolution of its length is given by:

$$\dot{x} = -\frac{k_1 k_2}{\eta(k_1 + k_2)}(x - x^0). \tag{2.2}$$

A natural question to ask is whether we can relate the material and geometric properties of the asperities to the parameters k_1, k_2, and η of the SLS. One way to do this would be to solve a viscoelastic Hertzian problem. Assuming that the asperity is spherical and the material is linear viscoelastic, from the solution of the elastic Hertzian problem, the viscoelastic Hertzian problem can be solved using the method of Laplace transforms [55]. The contact, initially at zero force and deformation, is instantaneously brought to a deformation δ_0 and the evolution of the force is computed. The instantaneous force is related to the instantaneous stiffness of the SLS, $k_1 + k_2$, the steady state force is related to k_1, and the rate of relaxation to steady state is related to η. The Hertzian contact problem is nonlinear, whereas the SLS element is linear. The nonlinearity of the Hertzian problem manifests as the dependence of k_1, k_2, and η on the deformation δ_0. We can, however, get an order-of-magnitude estimate of the values of the parameters in our model. Results from such calculations for two materials, Polyvinyl Alcohol (PVOH) and Polystyrene [55], are given below.

PVOH:

$$\frac{k_1}{\sqrt{\rho\delta_0}} = 0.18 \text{ GPa}, \frac{k_2}{\sqrt{\rho\delta_0}} = 0.15 \text{ GPa}, \frac{\eta}{\sqrt{\rho\delta_0}} = 0.48 \text{ GPa-s}.$$

Polystyrene:

$$\frac{k_1}{\sqrt{\rho\delta_0}} = 2.75 \text{ GPa}, \frac{k_2}{\sqrt{\rho\delta_0}} = 0.39 \text{ GPa}, \frac{\eta}{\sqrt{\rho\delta_0}} = 4.51 \text{ GPa-s}.$$

Above, ρ is the radius of curvature of the asperity.

2.1.2 Rough surfaces

Rough surfaces have been characterized by representing the heights from a reference level as a stochastic process [56, 57]. This characterization has been used extensively in exploring various aspects of contact between surfaces [26, 58, 59]. Profile measurements have shown that many types of surfaces can be modeled as a Gaussian noise with an exponential correlation [60]. Such a noise, known as an Ornstein-Uhlenbeck process, satisfies the following stochastic differential equation:

$$\frac{dy}{dz} = -\frac{1}{\lambda}y(z) + \sqrt{\frac{2}{\lambda}}\sigma\zeta(z). \tag{2.3}$$

Here, y is the height of the surface from a reference level (chosen such that the mean height is zero), z is the horizontal spatial variable, λ is the correlation length, σ is the rms roughness of the surface, and $\zeta(z)$ is a Gaussian white noise with unit standard deviation. For typical surfaces, σ and λ are of the order of a few microns [60]. We adopt this description of a rough surface. We also assume that the surface is rigid, since this considerably simplifies our calculations.

2.1.3 Local friction law

To determine the coefficient of friction, we need the macroscopic normal and shear forces. To compute the macroscopic shear force as a moment with respect to the probability distribution of microscopic normal forces, we need to know how the normal and shear forces are related for a single asperity. We assume local friction laws of the form,

$$s(F, v) = f(v)F + c_2F^n, \quad f(v) = \begin{cases} 0 & v \leq v_c \\ \mu_0 + c_1\log(\bar{v}) & v > v_c. \end{cases} \tag{2.4}$$

s here is the shear force at the contact, F is the local normal force, v is the sliding speed, $\bar{v}$ is the nondimensional sliding speed, μ_0, n, c_1, and c_2 are constants, v_c is the cutoff velocity for the velocity dependence of friction, and $2/3 \leq n \leq 1$.

The local friction law depends on the material and geometry of the contacts. If a contact is elastic and its geometry is spherical, then, by the Hertz theory of contact, the area of contact varies as the two-thirds power of the normal force. Further, if the contact has a shear strength τ_{max}, then the local friction law is:

$$A \propto F^{2/3}, \qquad s = \tau_{max} A \propto F^{2/3}.$$

As in the Bowden and Tabor model, if contacts are plastic because of the high local stresses, the area of contact is proportional to the normal force and the local friction law is:

$$A \propto F^{1}, \qquad s = \tau_{max} A \propto F^{1}.$$

An actual contact may be in between these two limiting cases and thus, the power in the local friction law between 2/3 and 1. Also, different contacts in the population may be in different states.

If the surfaces are sliding at a relative speed v, then the asperities in contact are sheared at a strain rate proportional to the sliding speed, and if the shear resistance depends on the strain rate, then the local friction law will be velocity-dependent. Taking cue from experimental results, we assume this velocity dependence to be logarithmic. A theoretical justification for the logarithmic dependence has been proposed by Rice et al [61].

Alternatively, local friction laws can be derived from theoretical and experimental studies of single asperity contacts. For example, Kogut and Etsion [62] consider the inception of sliding of a single spherical elastoplastic contact and conclude that $\mu \propto F^{-0.345}$ when the normal force by itself does not cause any plastic deformation (μ here is the single asperity friction coefficient). Note that this is very close to the Hertzian $s \propto F^{2/3}$ approximation above. Archard [63], using a crossed cylinder apparatus, reports $\mu \propto F^{-0.26}$ for perspex and $\mu \propto F^{-1/3}$ for brass. Wandersman et al [17], looking at texture-induced modulations of friction, report that $s \propto F^{0.87}$ for an elastomer on glass.

To summarize, our model for two rough surfaces in contact consists of an ensemble of independent viscoelastic SLS elements sitting on a rigid rough surface modeled as an Ornstein-Uhlenbeck process. With this model, we simulate the static contact and velocity jump experiments to study the time and velocity dependence of friction.

2.2 Static friction

2.2.1 Formulation

In this section, we study the evolution of an ensemble of independent SLS elements in static contact with a rigid rough Gaussian surface (Figure 2.1) under a global normal force F_N. The evolution of each SLS is governed by Equations (2.1) and (2.2). For simplicity, we assume that the values of k_1, k_2, η, and x^0 are the same for every element in the ensemble. Without loss of generality, we can set $x^0 = 0$, since this corresponds to choosing a particular reference level to measure the length x. Dilatation, which is the distance between the reference planes from which the lengths of the SLS elements x and the heights of the rigid surface y are measured, is denoted by d. At any instant t during the evolution of the system, only a fraction of the elements are in contact with the surface and for these, the contact condition implies:

$$x(t) + y = d(t). \tag{2.5}$$

Since we have assumed the parameters k_1, k_2, η, x^0 to be the same for all the elements in the ensemble, each element can be labeled by the height y of the rigid surface that it sees. At time t, the global normal force is given by:

$$F_N(t) = \mathbb{E}_y(F(t, y)) = \int_{d(t)}^{\infty} F(t, y) P_y(y) \mathrm{d}y, \tag{2.6}$$

where $F(t, y)$ is the force on an SLS corresponding to time t and height y of the rough surface, and $P_y(y)$ is the probability distribution of heights of the rough surface. The limits of integration are from $d(t)$ to ∞ since elements are in contact with the surface only if the height y is greater than $d(t)$ (since $x^0 = 0$). For a Gaussian distribution of surface heights, we have,

$$P_y(y) = \frac{1}{\sqrt{2\pi}\sigma} e^{-\frac{y^2}{2\sigma^2}}, \tag{2.7}$$

where σ is the rms roughness of the surface. The elements being viscoelastic, the force in the ones in contact would decrease with time if the dilatation were constant. To reproduce experimental conditions, we constrain the total normal force to be constant. To satisfy this constraint, dilatation has to decrease with time. Differentiating Equation (2.6) with respect to time gives:

$$\dot{F}_N(t) = \int_{d(t)}^{\infty} \frac{\partial F}{\partial t}(t,y) P_y(y) \mathrm{d}y - F(t,d) P_y(d) \dot{d}(t). \tag{2.8}$$

$F(t,d) = 0$ since $y = d(t)$ implies that the contact is formed at time t. The evolution equation for the force on an SLS (Equation (2.1) with $\dot{x} = \dot{d}$; $\dot{y} = 0$ as the surface is rigid) gives:

$$\frac{\partial F}{\partial t}(t,y) = (k_1 + k_2)\dot{d}(t) - \frac{k_2}{\eta} F(t,y) + \frac{k_1 k_2}{\eta}(d(t) - y). \tag{2.9}$$

Using $F(t,d) = 0$ and Equation (2.9) in Equation (2.8), the evolution equation for the dilatation at constant normal force ($\dot{F}_N = 0$) is:

$$\dot{d}(t) = \frac{\frac{k_2}{\eta} F_N - \frac{k_1 k_2}{\eta} \int_{d(t)}^{\infty} (d(t) - y) P_y(y) \mathrm{d}y}{(k_1 + k_2) \int_{d(t)}^{\infty} P_y(y) \mathrm{d}y}. \tag{2.10}$$

We now turn to the static friction force. Knowing the local friction law, $s = s(F)$, we can determine the global shear force as,

$$F_S(t) = \mathbb{E}_y(s(F(t,y))) = \int_{d(t)}^{\infty} s(F(t,y)) P_y(y) \mathrm{d}y, \tag{2.11}$$

and the coefficient of friction can be calculated as the ratio of the two forces,

$$\mu_s(t) = \frac{F_S(t)}{F_N}. \tag{2.12}$$

Before proceeding further, we nondimensionalize the equations.

2.2.2 Nondimensionalization

To nondimensionalize time, we use η/k_2, which is one of the two characteristic timescales of the SLS. A natural length scale in the problem is the rms roughness of the surface, σ. For forces, we use $k_1\sigma$. Using these characteristic quantities, we define the following nondimensional variables:

$$\bar{t} = \frac{t}{\eta/k_2}, \quad \bar{d} = \frac{d}{\sigma}, \quad \bar{y} = \frac{y}{\sigma}, \quad \bar{F} = \frac{F}{k_1\sigma}. \tag{2.13}$$

Equation (2.9) after nondimensionalization, is:

$$\frac{\partial \bar{F}}{\partial \bar{t}}(\bar{t}, \bar{y}) = R\bar{d}' - \bar{F}(\bar{t}, \bar{y}) + \bar{d}(\bar{t}) - \bar{y}. \tag{2.14}$$

The nondimensional equation for the dilatation evolution is:

$$\bar{d}' = \frac{\bar{F}_N(\bar{t}) - \int_{\bar{d}}^{\infty} (\bar{d} - \bar{y}) P_{\bar{y}}(\bar{y}) \mathrm{d}\bar{y}}{R \int_{\bar{d}}^{\infty} P_{\bar{y}}(\bar{y}) \mathrm{d}\bar{y}}, \tag{2.15}$$

and the coefficient of friction is given by:

$$\mu_s(\bar{t}) = \frac{\bar{F}_S(\bar{t})}{\bar{F}_N}.$$

In the above equations, prime denotes differentiation with respect to nondimensionalized time,

$$R = 1 + \frac{k_2}{k_1}, \tag{2.16}$$

and the probability distribution of the normalized surface heights $P_{\bar{y}}(\bar{y}) = \frac{1}{\sqrt{2\pi}} e^{-\frac{\bar{y}^2}{2}}$.

After nondimensionalization, we have two parameters: R, which is the ratio between the instantaneous and steady state stiffnesses, and n, the power in the local friction law. The local friction exponent n is indicative of the state of the contact, being 2/3 for elastic and 1 for plastic contact.

2.2.3 Static friction evolution

Suppose that, at $t = 0$, an ensemble of SLS elements is instantaneously brought to a dilatation $d = d_0$ against the rigid surface. Some of the SLS elements come into contact with the surface and result in a total normal force F_N. The system is then allowed to evolve at this constant global normal force F_N. The dilatation evolves to satisfy the constraint of constant F_N. This evolution can be calculated using Equation (2.15). From the dilatation history, the evolution of the probability density of the normal forces can be determined using Equation (2.14). Using this and the local friction law, we can determine the evolution of the static friction coefficient.

Figure 2.2 shows the evolution of μ_s for different local friction exponents. At small times, $\frac{t}{\eta/k_2} \ll 1$, μ_s remains constant, since the SLS elements need a finite time to start relaxing. μ_s then starts increasing and, around the relaxation time of the SLS, $\frac{t}{\eta/k_2} = \mathcal{O}(1)$, the increase is approximately logarithmic in time. At large times, $\frac{t}{\eta/k_2} \gg 1$, all the SLS elements have relaxed to their steady state and μ_s evolves to a constant value.

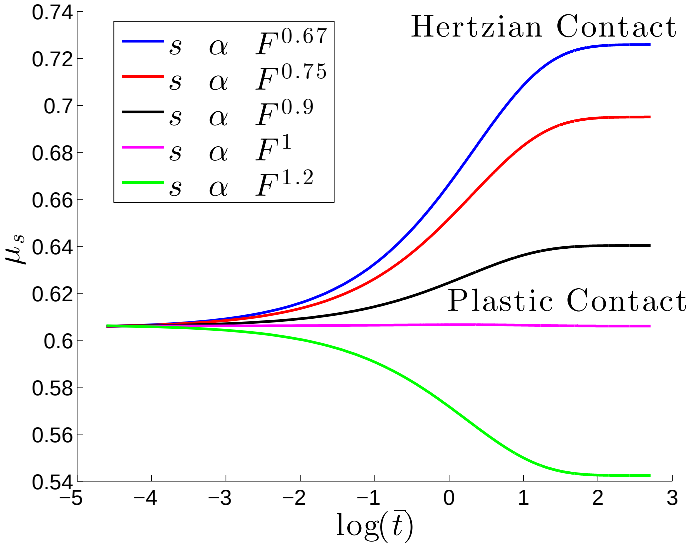

Figure 2.2: Evolution of the static friction coefficient (μ_s) with time at a constant global normal force for different local friction exponents n. For the physically relevant values of $n \in [2/3, 1)$, μ_s increases logarithmically with time for a range of times around the relaxation time of each asperity. For the unphysical case $n > 1$, μ_s decreases with time, a behavior that has not been observed in experiments.

The variation in μ_s is largest for the case of elastic contacts ($n = 2/3$). As the power in the local friction law reaches 1, the case of plastic contacts, we recover the result of the Bowden and Tabor model in which the friction coefficient is a constant given by the ratio of the shear strength to the hardness of the contacts. For $n > 1$, μ_s decreases with the time of contact. As explained in section 2.1.3, we expect $n \in [2/3, 1]$ for real materials. We believe this to be the reason why we only see an increase of μ_s in experiments.

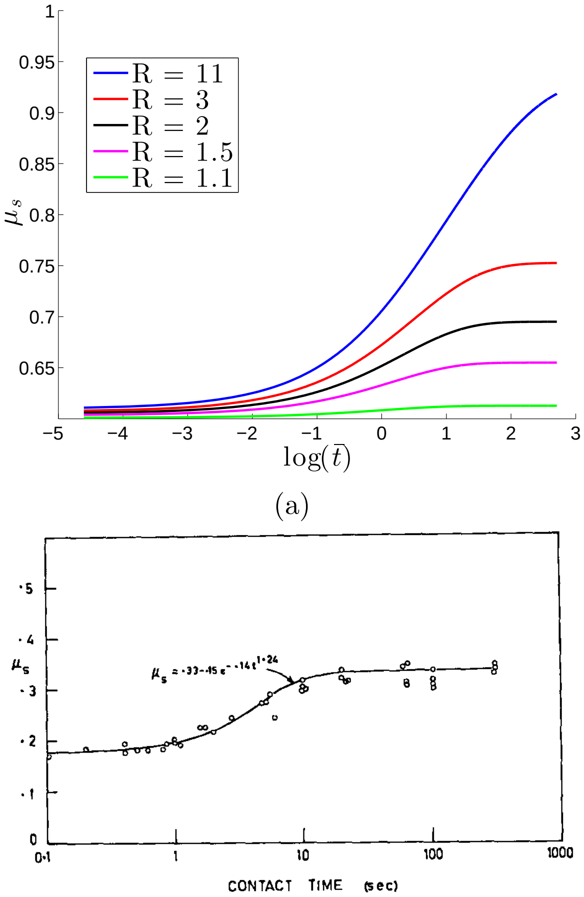

(a)

(b)

Figure 2.3: (a) Evolution of friction coefficient with time at a constant global normal force for different stiffness ratios, $R = 1 + k_2/k_1$. The system reaches steady state faster for smaller R. (b) The saturation at small and large times has also been observed in some experiments (reproduced with permission from [39]).

Figure 2.3a shows the evolution of μ_s for different values of R, using a local friction law $s(F) \propto F^{0.75}$. When $R \approx 1$, or $k_2 \ll k_1$, the instantaneous and steady state stiffnesses are not very different, and hence the growth in the friction coefficient is small. For $k_2 \gg k_1$, the instantaneous and steady state stiffnesses are very different and consequently, we see a larger growth in μ_s. Also, Figure 2.3a shows that the steady state is reached faster when R is smaller. The SLS has two characteristic timescales, η/k_2 and $\frac{\eta}{k_2}(1 + k_2/k_1)$. Since we have nondimensionalized time with η/k_2, R is the second characteristic timescale in nondimensionalized time and thus, for smaller R, the steady state is achieved faster.

The predicted increase of the coefficient of static friction with time has been widely observed in experiments [32, 40, 39]. If η/k_2 is of $\mathcal{O}(1)$ seconds, as it is for the two materials mentioned earlier, we see that the friction coefficient reaches its steady state at around 10^2 seconds and the total variation in μ_s lasts about 3-4 decades in time. In some materials like mild steel, the predicted behavior – linear increase with logarithmic time over a few decades with a lower and upper saturation for small and large times – is also in agreement with experimental observations [64, 39], as shown in the Figure 2.3b. In the experiments on rocks [40, 33], however, the logarithmic growth persists through the duration of the experiment (some experiments have lasted six decades in time). Since μ_s cannot increase indefinitely, it eventually has to reach a steady state. This delayed saturation is not captured by our model. We conjecture that the difference between our model response and the rock experiments could be for the following reasons. The SLS element has only one relaxation time, while a real viscoelastic material has many relaxation timescales. In Figures 2.2 and 2.3a, the x-axis is the nondimensionalized logarithmic time. When plotted with respect to logarithmic time, changing η/k_2 corresponds to translating the curve horizontally by $\log(\eta/k_2)$. Thus, in the case of multiple relaxation timescales (multiple η/k_2), the region of μ_s increase will be wider. Furthermore, if the asperities interact with each other through the bulk, the interactions can result in a continuum of timescales for the response at the macroscopic scale. Exploring this hypothesis remains a topic of current work.

2.3 Kinetic friction

2.3.1 Formulation

Consider a single SLS sliding on a rough rigid surface (Figure 2.1). The slider can be in two states, either in contact or out of contact with the surface. When in contact, its length evolves to conform to the rigid surface, $x(t) = d(t) - y(t)$ and the force evolves according to Equation (2.1). Since we have modeled the rough surface as a stochastic process, the differential equation for force evolution during contact will also be a stochastic one. If the SLS ensemble slides at a constant velocity v, then the horizontal coordinate is $z = vt$. Using chain rule, we can change the independent variable from the horizontal coordinate z to time t in Equation (2.3) for the rough surface:

$$\frac{dy}{dt} = \frac{dy}{dz}\frac{dz}{dt} = v\frac{dy}{dz} = -\frac{v}{\lambda}y(t) + \sqrt{\frac{2v}{\lambda}}\sigma\zeta(t). \tag{2.17}$$

When the slider is in contact with the surface, $\dot{x} = \dot{d} - \dot{y}$. Using this and Equation (2.17) in Equation (2.1), the stochastic differential equation for the evolution of the normal force during contact is:

$$\begin{aligned}\dot{F}(t) = &-\frac{k_2}{\eta}F(t) + (k_1+k_2)\dot{d}(t) + \frac{k_1k_2}{\eta}(d(t) - x^0)\\ &+ \left(\frac{(k_1+k_2)v}{\lambda} - \frac{k_1k_2}{\eta}\right)y(t) - (k_1+k_2)\sqrt{\frac{2v}{\lambda}}\sigma\zeta(t).\end{aligned} \tag{2.18}$$

Here, the terms $y(t)$ and $\zeta(t)$ are the Ornstein-Uhlenbeck and white noise, respectively. Their statistical properties are:

$$< y(t) >= 0, \qquad < y(t_1)y(t_2) >= \sigma^2 e^{-\frac{v|t_1-t_2|}{\lambda}}, \tag{2.19}$$

$$< \zeta(t) >= 0, \qquad < \zeta(t_1)\zeta(t_2) >= \delta(t_1 - t_2),$$

$$< \zeta(t_1)y(t_2) >= \begin{cases} 0, & \text{if } t_1 > t_2,\\ \sqrt{\frac{2v}{\lambda}}\sigma e^{-v|t_2-t_1|/\lambda}, & \text{if } t_1 <= t_2,\end{cases}$$

where <> denotes ensemble average. Since $y(t)$ is driven by $\zeta(t)$ (Equation (2.17)), the cross correlation between the two noises is not zero.

When the slider is not in contact, the normal force is zero and its length evolves according to Equation (2.2). Before proceeding further, we nondimensionalize the above system of equations.

2.3.2 Nondimensionalization

As before, we use σ to nondimensionalize length, η/k_2 to nondimensionalize time and $k_1\sigma$ to nondimensionalize force, and use a bar to denote non-dimensional quantities. Equation (2.18) for an SLS in contact, after nondimensionalization is:

$$\bar{F}' = -\bar{F} + R\bar{d}' + \bar{d} - \bar{x}^0 + \left(\frac{R\bar{v}}{\bar{\lambda}} - 1\right)\bar{y} - R\sqrt{\frac{2\bar{v}}{\bar{\lambda}}}\bar{\zeta}, \tag{2.20}$$

$$< \bar{y} >= 0, \quad < \bar{y}(\bar{t}_1)\bar{y}(\bar{t}_2) >= e^{-\bar{v}|\bar{t}_1-\bar{t}_2|/\bar{\lambda}}, \tag{2.21}$$

$$< \bar{\zeta} >= 0, \quad < \bar{\zeta}(\bar{t}_1)\bar{\zeta}(\bar{t}_2) >= \delta(\bar{t}_1 - \bar{t}_2).$$

After nondimensionalization, Equation (2.2) for an SLS out of contact becomes:

$$\bar{x}' = -\frac{1}{R}(\bar{x} - \bar{x}^0). \tag{2.22}$$

As before prime denotes differentiation with respect to $\bar{t}$.

$\bar{x}^0$, the undeformed length of the viscoelastic sliders, may be set to 0 since this is equivalent to choosing a reference level. $\bar{\lambda}$ is the correlation length of the surface, which we set to 1. In the governing equations, $\bar{\lambda}$ appears only as $\bar{v}/\bar{\lambda}$, thus $\bar{\lambda}$ sets a scale for the sliding speed.

This leaves the following non-trivial parameters in the model. R, as in the static contact case, is the ratio of the instantaneous and steady state stiffnesses of the SLS. $\bar{v} = k_2 v/\eta\sigma$, a nondimensional sliding speed, is the number of rms roughness lengths that the SLS slides in one relaxation time η/k_2. If $\bar{v} \gg 1$, the SLS has little time to relax when in contact and hence its response will be close to its instantaneous elastic response. If $\bar{v} \ll 1$, the SLS has time to relax to its steady state and its response will be similar to its steady state elastic response.

We have four parameters in the local friction law, μ_0, c_1, c_2, n (Equation 2.4). μ_0 sets a reference value for the coefficient of friction, and we choose this to be 0.6. The constant c_1 controls velocity dependence of the local friction and is set to 0.01 unless otherwise mentioned. The constant c_2 describes the evolution of the friction on steady sliding, and is set to 0.2. Unless mentioned otherwise, the local friction exponent n is set to 0.67 since the transient is most pronounced in this case.

2.3.3 From one to many

As the surfaces slide, each asperity sees a different profile. If two asperities are close to each other, the profiles they see will be correlated. We neglect this correlation and associate an independent realization of the noise $\bar{y}(\bar{t})$ as the profile on which an SLS element slides. The question we seek to answer is: given the statistical properties of $\bar{y}(\bar{t})$, what are the statistical properties of the force $\bar{F}$? In particular, what is the probability density of force $P(\bar{F})$? A stochastic equation such as Equation (2.20) is known as a Langevin equation. Averaging this equation over the ensemble of realizations of the noise $\bar{y}(\bar{t})$, one can derive a partial differential equation for the evolution of the probability density $P(\bar{t}, \bar{F})$ [65]. An example of this is the heat equation, which results from the averaging of the stochastic equation corresponding to the Brownian motion of a single particle. We would like to do a similar ensemble averaging of Equation (2.20). The problem, however, is that we have two sources of noise, $\bar{y}(\bar{t})$ and $\bar{\zeta}(\bar{t})$, and the two are correlated (Equation (2.19)). In such a case, there is no known method of deriving the partial differential equation for the evolution of probability density. Hence, we resort to a numerical Monte Carlo method where we generate an ensemble of sliders and surface profile realizations, evolve the system at the microscale, and compute statistics of the ensemble to determine macroscopic properties. There is, however, a particular case of pure white noise, where we can derive a partial differential equation for the evolution of $P(\bar{t}, \bar{F})$.

2.3.4 The case of pure white noise

In Equation (2.20), if the velocity $\bar{v} = \bar{\lambda}/R$, the coefficient of $\bar{y}$ becomes zero. We are then left with only the white noise term and we can derive a partial differential equation (Fokker-Planck equation) for the evolution of $P(\bar{t}, F)$. The Fokker-Planck equation corresponding to the Langevin equation (2.20) when $\bar{v} = \bar{\lambda}/R$ is [65]:

$$\frac{\partial P}{\partial \bar{t}} + \frac{\partial S}{\partial \bar{F}} = 0, \tag{2.23}$$

$$S(\bar{t}, \bar{F}) = \left[-\bar{F} + R\bar{d}' + \bar{d} - \bar{x}^0 - R\frac{\partial}{\partial \bar{F}} \right] P(\bar{t}, \bar{F}). \tag{2.24}$$

Here, $S(\bar{t}, \bar{F})$ is the flux of $P(\bar{t}, \bar{F})$. To complete the problem, we need boundary conditions at $\bar{F} = 0$ and $\bar{F} = -\infty$ $\big(\bar{F} \in (-\infty, 0]$, no tension at contacts$\big)$. At $\bar{F} = -\infty$, both the probability density and flux have to vanish. The boundary condition at $\bar{F} = 0$ is nontrivial. The flux there depends on the sliders coming into and going out of contact, since this corresponds to the force changing between zero and nonzero values. We know of no way of explicitly deriving this boundary condition.

Let us look at the steady state. At steady state, $\frac{\partial P}{\partial \bar{t}} = 0$ and $\bar{d}' = 0$. From Equation (2.23), the flux is uniform in the domain and $S(-\infty) = 0$ implies it is zero everywhere. Setting Equation (2.24) to zero, the probability density at steady state is:

$$P(\bar{F}) = ce^{-\frac{\bar{F}^2}{2R} + \frac{(\bar{d} - \bar{x}^0)\bar{F}}{R}}. \tag{2.25}$$

There are two unknowns here: the constant c and the steady state dilatation $\bar{d}$. We have one constraint: that the first moment of the probability density be equal to the applied normal force. Using the constraint, we can relate the constant c and the dilatation $\bar{d}$ as,

$$c = \frac{\bar{F}_N}{\int_{\bar{d}}^{\infty} \bar{F} e^{-\frac{\bar{F}^2}{2R} + \frac{(\bar{d} - \bar{x}^0)\bar{F}}{R}} \mathrm{d}\bar{F}}. \tag{2.26}$$

The other constraint comes from the boundary condition at $\bar{F} = 0$, which cannot be determined explicitly.

2.3.5 Monte Carlo method

Since the Fokker-Planck equation can be derived only for a particular velocity, we resort to Monte Carlo simulation in the general case. We generate an ensemble of sliders, each sliding on an independent realization of the noise $\bar{y}(\bar{t})$ with the given statistical properties of Gaussian height distribution and exponential correlation. Again, we assume the parameters k_1, k_2, η, x^0 to be the same for all the sliders. The noise is generated at a finite discretization size and this introduces a low-wavelength cutoff in the surface features. The power spectrum of the Ornstein-Uhlenbeck noise is given by:

$$S(\omega) = \frac{\lambda\sigma^2}{\pi}\frac{1}{1+\omega^2\lambda^2},$$

where ω is the spatial frequency. The power in frequencies beyond 10 times the inverse correlation length is small. Therefore, we discretize the surface to resolve this frequency [66]. For heights of the surface between the discretization points, and the derivative of the surface height, we use spline interpolation.

At $\bar{t} = 0$, the ensemble of sliders is brought into contact with the rigid surface and this results in a global normal force $\bar{F}_N$. In experiments, the surfaces slide at a constant global normal force. As in the static contact case, the dilatation $\bar{d}$ evolves to satisfy the constant normal force constraint. At each time step, the rate of dilatation is determined to ensure that the global normal force remains constant. Once the rate of dilatation is known, the forces and lengths of all the sliders can be updated. For time stepping, we use a first order Euler method. Since, at any instant, the state of all the sliders and thus the force $\bar{F}$ on each of them is known, we can determine the local shear forces using the local friction law, and, adding them, the global shear force $\bar{F}_S$. The friction coefficient is then determined to be, $\mu_k(t) = F_S(t)/F_N$.

2.3.6 Test of Monte Carlo method

We use the Fokker-Planck equation of Section 2.3.4 as a test of our Monte Carlo method. Starting at an initial state, we let the system slide at the velocity $\bar{v} = \bar{\lambda}/R$ (the case for which we can derive the Fokker-Planck equation) till it reaches steady state. Knowing the normal forces on all the sliders, we can compute the probability density. This density is also known from the solution of the Fokker-Planck equation at steady state (Equations (2.25) and (2.26)) and the two can be compared.

Figure 2.4 shows the probability density of forces in the initial and steady states using the Monte Carlo and Fokker-Planck methods. In this simulation, $R = 2, \bar{\lambda} = 1$ and thus $\bar{v} = 0.5$. An ensemble of 10^5 sliders is used. From the figure, there is a good match in the probability densities using the two methods. As a further verification, we have also computed the transient evolution with the two methods, using the Monte Carlo simulation to prescribe the boundary condition at $\bar{F} = 0$ for the Fokker-Planck equation. The two transients also show a good match with each other.

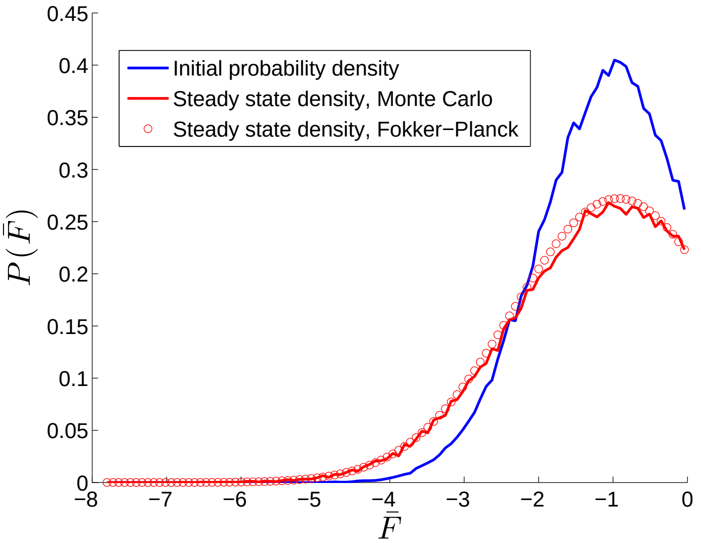

Figure 2.4: Probability density of normal forces at an initial state, and at steady state using two different methods, a Monte Carlo method and the Fokker-Planck solution. Note that some sliders are not in contact and thus the area under the curve, which is equal to the fraction of sliders in contact, is less than 1. In other words, there is a Dirac mass at $\bar{F} = 0$.

2.3.7 Velocity jump test

Drawing confidence from the above result, we perform velocity jump simulations using the Monte Carlo approach. For typical surfaces, σ is of the order of a micron and sliding velocities in the jump tests are usually between 0.01μm/s and 100μm/s. η/k_2

is of the order of a few seconds for the two materials mentioned in section 2.1.1. Thus, $\bar{v}$ ranges from 10^{-2} to 10^{2}. Starting from an initial state, we let an ensemble of 10^5 elements slide at $\bar{v} = 0.1$ till it reaches steady state. The velocity is then instantaneously changed to $\bar{v} = 1$ and the system is allowed to evolve to steady state. Velocity jumps to $\bar{v} = 0.1$ and $\bar{v} = 1$ are then repeated.

Figure 2.5a shows the evolution of the friction coefficient for two sets of parameter values (all parameters are the same except R). In both cases, we find that the friction coefficient changes instantaneously when the velocity jumps, and the change has the same sense as that of the velocity jump; i.e., the friction coefficient jumps up (down) when the velocity jumps up (down). Following the standard rate and state terminology, we call this jump the *direct effect*. This jump is followed by an evolution towards a steady state. We call this the *transient*. In both cases, this transient changes the friction coefficient in the direction opposite to the direct effect, i.e., the friction coefficient decreases from the high value following a jump up and increases from a low value following a jump down. In one case ($R = 1.1$, or the higher curve), the transient is smaller than the direct effect so that the steady state value is still higher (lower) for an increase (decrease) in velocity. This represents *velocity strengthening* behavior. In the other case ($R = 11$, or the higher curve), the transient is larger than the direct effect so that the steady state value is lower (higher) for an increase (decrease) in velocity. This represents *velocity weakening* behavior. If the power n in the local friction law is greater than 1, as shown in Figure 2.5b, then the friction coefficient change during the transient is in the same direction as the direct effect.

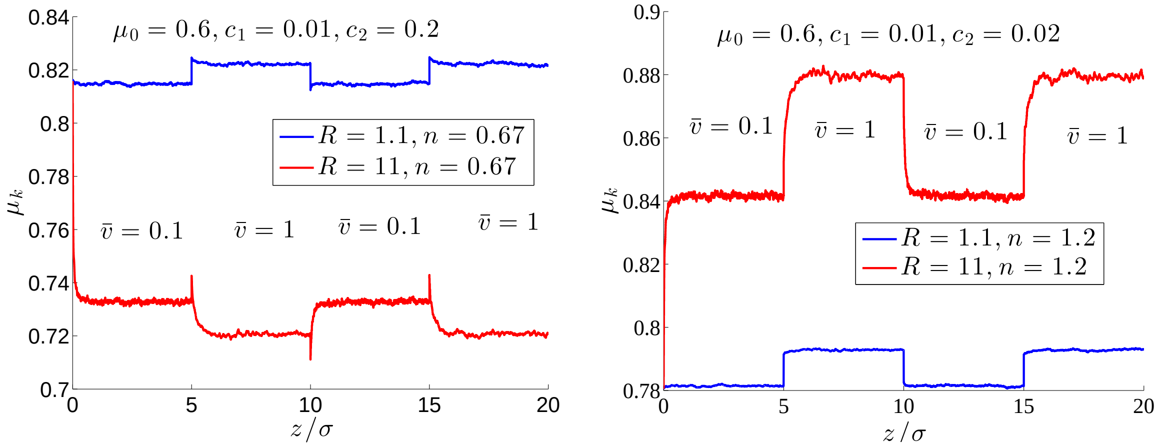

(a) (b)

Figure 2.5: Evolution of friction coefficient in velocity jump tests. (a) For $n < 1$, the direct effect and the transient compete against each other. Depending on the parameters, either the instantaneous or the transient effect dominates, leading respectively to velocity strengthening or velocity weakening. (b) For $n > 1$, the friction coefficient changes in the same direction during the direct effect and the transient.

Figure 2.6 shows the evolution of the dilatation for the same two sets of parameter values. We observe that the dilatation changes continuously with no jumps, and evolves towards a steady state following an imposed velocity jump. Further, the evolution occurs in the same sense, toward higher dilatation for higher velocity and vice versa, for both sets of parameters. The excursions are larger for larger R (the change in dilatation is hardly visible for the case $R = 1.1$).

In our model, the force on an asperity changes continuously with time, and therefore the force distribution also changes continuously with time. This is reflected in Figure 2.6. Therefore, the direct effect in Figure 2.5a is a direct consequence of our local friction law. In fact, the instantaneous increase in μ_k is given by $c_1 \log(v_{new}/v_{old})$. The subsequent evolution is a result of the collective behavior due to the evolution of the force distribution in addition to the local friction law. Since the dilatation increases with increasing velocity, the applied global normal force is carried by fewer asperities with larger average forces on each (we elaborate on this later). Consequently, if the exponent n in the local friction law satisfies $n < 1$ as we expect from the physics, velocity jump will lead to a decrease in friction coefficient during the evolution phase, and velocity jump down will lead to an increase in friction coefficient during evolution phase. In short, the direct effect and evolution will always compete with each other.

The above results capture many features of experimental observations. Both the direct effect and the transient are observed in experiments [33, 41, 9]. Further, the direct effect always follows the velocity jump. Furthermore, the direct effect and evolution always change the friction coefficient in opposite directions. This is consistent with the requirement that $n \in [2/3, 1]$. Finally, both velocity- strengthening and velocity-weakening behaviors have been observed.

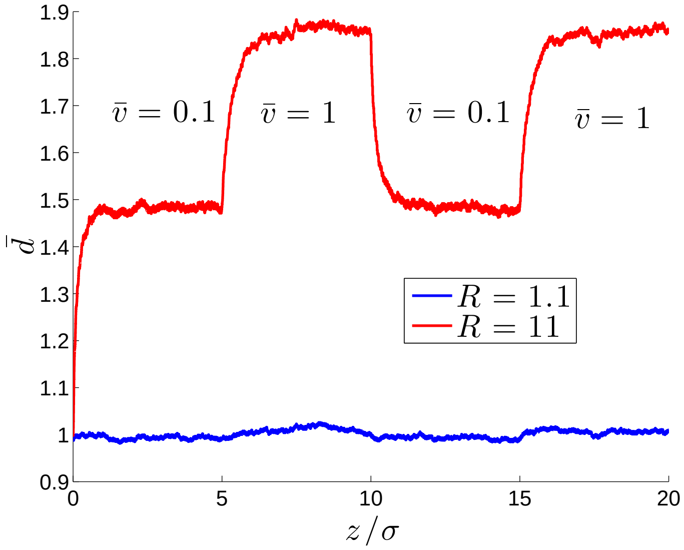

Figure 2.6: Evolution of dilatation in the velocity jump test. The average normal force on an asperity in contact is higher at higher sliding speeds. Thus, for the same global normal force, fewer sliders are in contact at higher speeds and the dilatation is larger. For R close to 1, the changes in dilatation are hardly apparent.

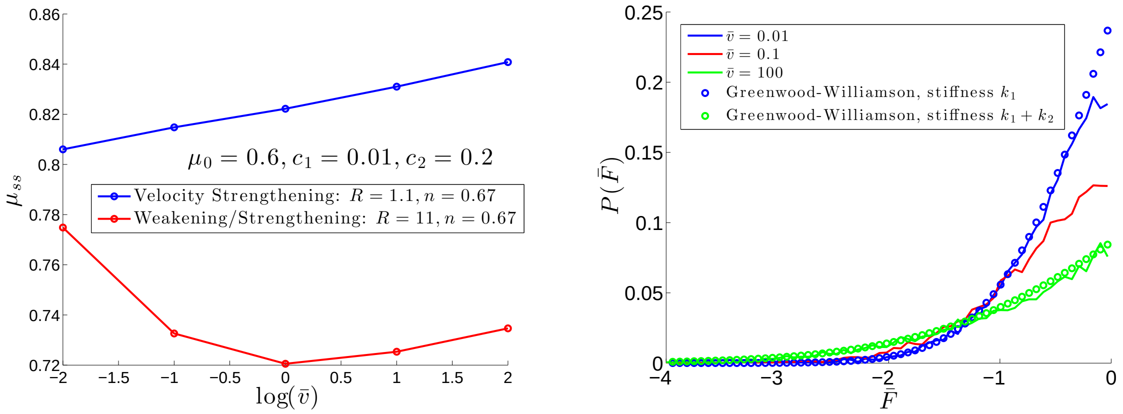

(a) (b)

Figure 2.7: (a) Velocity dependence of the steady-state friction coefficient. Depending on the parameters and the sliding speed, we can have velocity strengthening or velocity weakening. Transitions between strengthening and weakening behaviors have been observed in experiments [67]. (b) Probability density of the normal forces at steady state at different sliding speeds (solid lines). At higher speeds, the average normal force on an asperity in contact is higher. Thus, the area under the curve, which represents the fraction of sliders in contact, is smaller at higher speeds. The first moment of the force distribution, which is the global normal force, is the same for all the curves. Also shown is the probability density of forces in a linearized Greenwood-Williamson model with stiffnesses k_1 and $k_1 + k_2$. These are the force distributions in the limit of 0 and infinite sliding speeds.

2.3.8 Velocity strengthening vs. velocity weakening

Figure 2.7a shows the dependence of the steady-state friction coefficient on the sliding speed. One case (the blue curve) shows velocity strengthening at all sliding speeds, whereas the other case (the red curve) shows velocity weakening at low sliding speeds and strengthening at higher speeds. Since the SLS has only one relaxation timescale, the distribution of forces on asperities is sensitive to the sliding velocity only in a limited range of velocities (the lower velocities for the red curve). Outside this velocity range (the higher velocities for the red curve), the local friction properties dominate and we get velocity-strengthening behavior. The transition between velocity strengthening and velocity weakening has been observed in experiments [67].

2.3.9 Distribution of forces on asperities

Figure 2.7b shows the probability density of the normal forces at steady state at different sliding speeds. At higher sliding speeds, for the same global normal force, fewer sliders need to be in contact since the normal force on each of the ones in contact is higher on average. This can be seen in the figure where the area under the probability density curve, which represents the fraction of sliders in contact, is smaller at higher speeds. Also shown is the probability density of the normal forces in a linearized version of the Greenwood-Williamson model (where the nonlinear Hertzian contact is replaced by a linear one). The two curves correspond to two different stiffnesses, k_1 and $k_1 + k_2$. At low sliding speeds, the SLS elements have more time to evolve towards their steady state and thus effectively only the spring with stiffness k_1 is active during contact. At high speeds, the dashpot has little time to react, and the effective stiffness is nearly $k_1 + k_2$. This can be seen in Figure 2.7b, where the probability densities at low and high sliding speeds are similar to the densities of the GW model with stiffnesses k_1 and $k_1 + k_2$, respectively. The probability densities at different speeds can be mapped to the probability density of the Greenwood-Williamson model with the effective stiffness dependent on the sliding speed.

2.3.10 Characteristic slip distance

D_c is the characteristic length scale over which the system evolves to its steady state in velocity jump tests. We calculate this by fitting an exponential to the evolution of μ_k. Figure 2.8a shows the dependence of D_c on the sliding speed $\bar{v}$ for two different values of R and for $n = 0.67$ and $\bar{\lambda} = 1$. D_c also depends on the correlation length of the surface, $\bar{\lambda}$. Recall that the parameter $\bar{\lambda}$ appears in the equations only as $\bar{v}/\bar{\lambda}$. If we have two surfaces with correlation lengths $\bar{\lambda}_1, \bar{\lambda}_2$, and the SLS ensemble slides on these surfaces at velocities $\bar{v}_1$ and $\bar{v}_2$ such that $\bar{v}_1/\bar{\lambda}_1 = \bar{v}_2/\bar{\lambda}_2$, then the decay lengths are related as:

$$D_c(\bar{v}_1, \bar{\lambda}_1) = \frac{\bar{\lambda}_1}{\bar{\lambda}_2} D_c(\bar{v}_2, \bar{\lambda}_2).$$

D_c is fairly independent of $\bar{v}$ in some laboratory experiments [33], and our simplified model does not capture this independence.

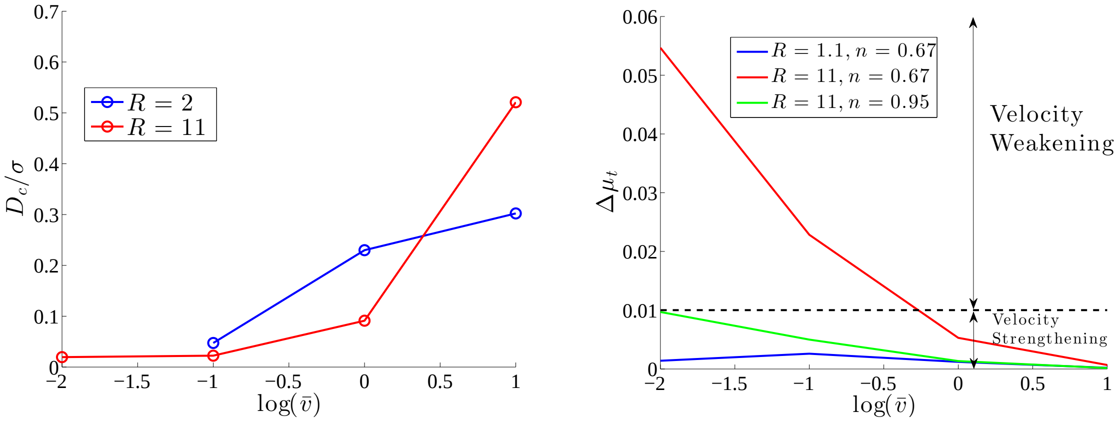

(a) (b)

Figure 2.8: (a)The characteristic length over which the system decays to steady state depends on the stiffness ratio R and the sliding speed $\bar{v}$. In many experiments, this distance is found to be a constant that depends only on the roughness of the surfaces. (b)The change in the friction coefficient during the transient phase following the direct effect for three different combinations of R and n. If the change during the transient is greater than the direct effect, then we have velocity-weakening (above the dashed line); otherwise, we have velocity- strengthening.

2.3.11 Parametric study

After nondimensionalization, we have five parameters: $R, \bar{\lambda}, n, c_1$, and c_2. Let us study the effect of each of them.

$R = 1 + k_2/k_1$ is the ratio between the instantaneous and steady-state stiffnesses of the SLS. When R is close to 1, the instantaneous and steady-state responses of the SLS are close, the differences between the distribution of forces on asperities at different sliding speeds are small, and thus, the transient change in μ_k following a jump in sliding speed is small. By a similar consideration, for large R ($k_2 \gg k_1$), the transient change in μ_k is large. Hence, for the same instantaneous effect, as the value of R increases, the behavior will change from velocity-strengthening to velocity-weakening, as illustrated in Figure 2.5a.

In the governing equations, (2.20), (2.21), and (2.22), the parameter $\bar{\lambda}$ appears only as $\bar{v}/\bar{\lambda}$. Thus, we can think of $\bar{\lambda}$ as setting a scale for the sliding speed. Consider two surfaces with correlation lengths $\bar{\lambda}_1$ and $\bar{\lambda}_2$ on which an SLS ensemble slides at two speeds $\bar{v}_1$ and $\bar{v}_2$. If $\bar{v}_1/\bar{\lambda}_1 = \bar{v}_2/\bar{\lambda}_2$, and if we start from the same initial state, the evolution of the two systems will be exactly the same. Since we have a velocity dependence in the local friction law, the coefficients of friction of the two systems will differ by $c_1 \log(\bar{v}_1/\bar{v}_2)$.

The power n in the local friction law represents the elasticity/plasticity of contacts. When $n = 1$, all contacts in the ensemble are plastic and the distribution of normal forces among the asperities has no effect on the friction coefficient. This is equivalent to the Bowden and Tabor model, modulo the velocity-dependent term in the local friction law. When $n = 2/3$, the effect of distribution of forces among asperities plays an important role in determining μ_k. Parameters c_1 and c_2 describe the microscopic frictional response of a single contact.

We would like to study how each of the above parameters affects the friction coefficient. To this end, we do velocity jump experiments at different speeds for different values of the parameters R and n, and calculate the change in μ_k during the transient phase ($\Delta\mu_t$) following the instantaneous jump. Figure 2.8b shows the value of $\Delta\mu_t$ at different velocities for three different combinations of parameters R and n. A value of $c_2 = 0.2$ has been used ($\Delta\mu_t$ changes linearly with c_2). Also shown as a dashed line is c_1, which has been assumed to be 0.01. We have velocity strengthening when $\Delta\mu_t < c_1$ (below the dashed line) and velocity weakening when $\Delta\mu_t > c_1$ (above the dashed line). In many experiments, $\Delta\mu_t$ is observed to be independent of the sliding speed. In our model, $\Delta\mu_t$ is not a constant for given material properties but varies with the sliding velocity.

2.3.12 Comparison with rate and state formulations

Our results on the evolution of friction coefficient in jump tests can be well fitted by the rate and state equations (1.3-1.5), as illustrated in Figure 2.9a. In the example shown, the best fit parameters for the rate and state equations are $\mu_0 = 0.7207, a = 0.0043 (= c_1/\ln 10), b = 0.0096$. v^* was chosen to be 1 and D_c/σ is 0.13 for the aging law and 0.042 for the slip law.

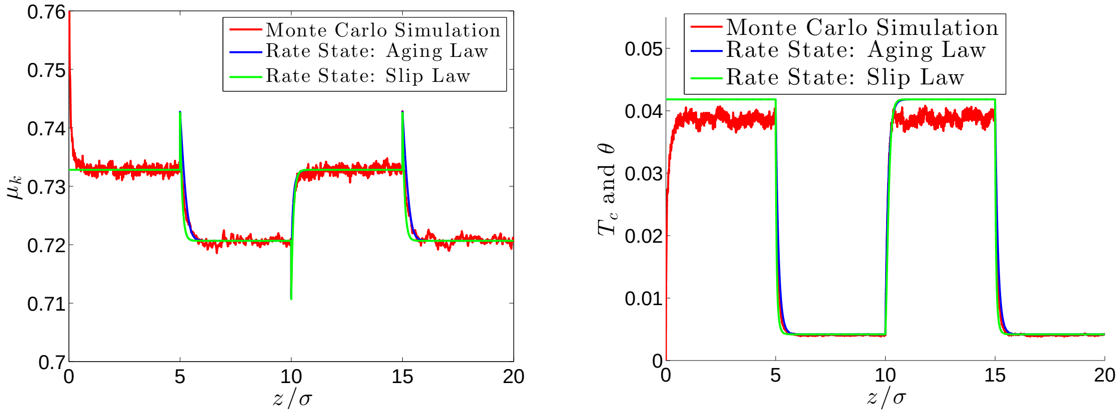

(a)

(b)

Figure 2.9: (a)Evolution of μ_k in a velocity jump test (with $R = 11$, $n = 0.67$), along with fits for two versions of the rate and state laws. (b)The average time of contact calculated using the Monte Carlo simulation (red), and the evolution of the state variable θ calculated from the fits in (a). The average time of contact is indeed close to the state variable evolution, supporting the interpretation of the state variable in the rate and state laws as the average contact time.

2.3.13 State variable

In the rate and state laws, the state variable is sometimes interpreted as the average contact time of the asperities [42, 49]. This time of contact can be calculated explicitly in our simulations. Figure 2.9b shows the evolution of the average time of contact (T_c) in a velocity jump test. Also shown in the figure is the evolution of the state variable θ for the two rate and state laws, calculated using the friction evolution fit of Figure 2.9a (θ does not match T_c in absolute value, the figure shows θ scaled to match T_c for the last data point). The steady-state T_c is approximately inversely proportional to the sliding speed, as proposed for the state variable in the rate and state formulations. Thus, our model is consistent with the idea that state variable in the rate and state laws is related to the average contact time.

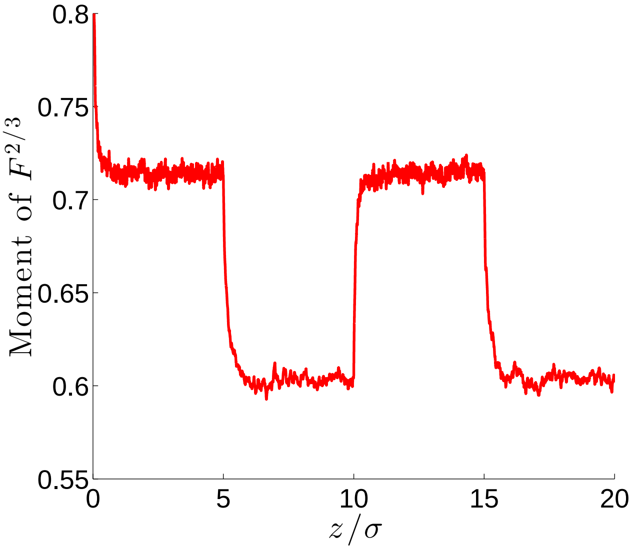

Figure 2.10: Evolution of the moment of $\bar{F}^n$ during the velocity jump test. This moment serves as the state variable in our model.

2.3.14 Moment as a state variable

In our model, the transient behavior in the velocity jump tests is proportional to the moment of $\bar{F}^n$, i.e., to

$$\psi(\bar{t}) = \int_{\bar{F}} \bar{F}^n P(\bar{t}, \bar{F}) \mathrm{d}\bar{F}. \tag{2.27}$$

The evolution of this moment is shown in Figure 2.10 for $n = 2/3$. This moment acts as the state variable in our model, and we can formulate the following rate and state description of our model:

$$\mu_k(\bar{t}) = \mu_0 + c_1 \log(\bar{v}) + c_2 \psi(\bar{t}), \tag{2.28}$$

$$\psi'(\bar{t}) = g(\bar{v})(\psi(\bar{t}) - \psi_{ss}(\bar{v})), \tag{2.29}$$

where $g(\bar{v})$ and $\psi_{ss}(\bar{v})$ can be determined by Monte Carlo simulations for given model parameters $R, n, \bar{\lambda}$. In fact, $g = \bar{v}/\bar{D}_c$, where $\bar{D}_c$ is shown in Figure 2.8a for $n = 0.67$ for two different values of R.

2.4 Nonlinear contact model

Until now, we have modeled asperities as linear viscoelastic elements. To test how sensitive the results of our model are to this assumption, we repeat the velocity jump simulations with a modified model for an asperity. We make spring 1 in the SLS nonlinear. The constitutive equations are:

$$F = k_1 sgn(x - x^0)|x - x^0|^{3/2} + \eta \dot{x}_\eta,$$

$$\eta \dot{x}_\eta = k_2(x_2 - x_2^0).$$

The power 3/2 has been chosen to mimic Hertzian contact behavior. Using the Monte Carlo method, we repeat the velocity jump experiment. Figure 2.11 shows that the evolution of the friction coefficient is similar to the linear SLS case. While not conclusive, this example suggests that the qualitative features of the results are not crucially dependent on the particular description of a single asperity.

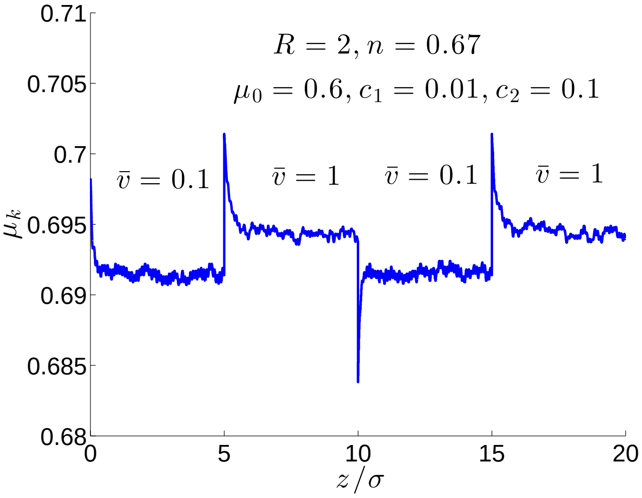

Figure 2.11: Velocity jump experiment with a nonlinear asperity model. The evolution of friction coefficient is qualitatively similar to the evolution in Figure 2.5a. Though not conclusive, this suggests that the qualitative features of the results are robust with respect to the single asperity model.

2.5 Multiple timescales

We conjectured that the saturation of the static friction coefficient in 3-4 decades (Figure 2.2) and the limited velocity range of velocity weakening (Figure 2.7a) is primarily due to the single timescale in the SLS. To verify this, we perform the static contact and velocity jump simulations with an ensemble of SLS having multiple timescales. Figure 2.12a shows the evolution of the static friction coefficient in two cases. In the first case (blue), all sliders in the ensemble have the same relaxation time, $\eta = 1$. In the other case (red), half the sliders have $\eta = 1$ and the other half have $\eta = 10$. The logarithmic growth regime is wider for the case with two timescales. Figure 2.12b shows the steady state friction coefficient as a function of the sliding speed. We see that the case with two timescales has a broader velocity-weakening regime. This confirms our conjecture that the existence of multiple timescales leads to longer evolution of the static friction coefficient and wider velocity-weakening regimes.

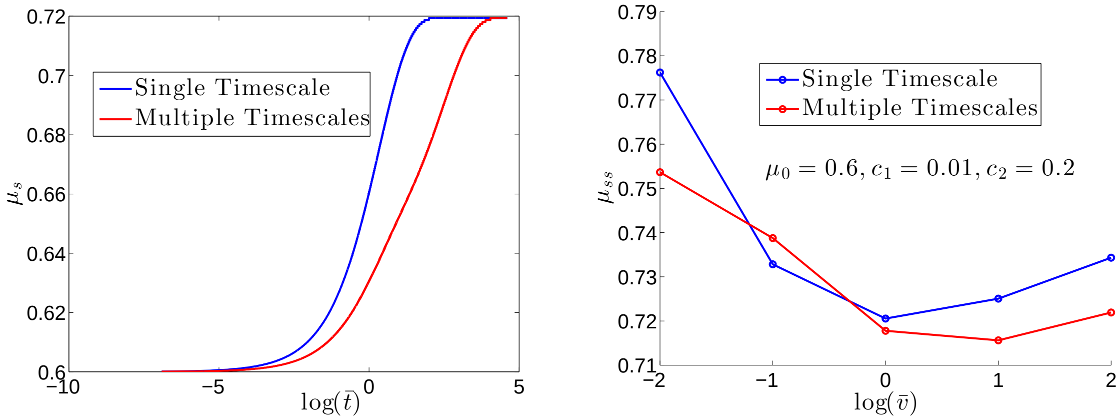

(a) (b)

Figure 2.12: (a) Evolution of static friction coefficient with hold time for an ensemble of SLS with two timescales. (b) The steady-state friction coefficient as a function of the sliding speed for an ensemble of SLS with two timescales.

2.6 Concluding remarks

In this chapter, we proposed a model for friction between macroscopic surfaces considering asperities at the microscale to be viscoelastic and modeling rough surfaces as a stochastic process. Our main contribution is a framework to link properties of single asperities and surface features to the macroscopic static and sliding frictional behavior. We showed that, because of the collective response of contacts, the behavior at the macroscale can be very different from that at the microscale.

Even in our relatively simple model, rate and state effects appear naturally as a consequence of the collective asperity response. The model reproduces the strengthening of the static friction with hold time. This strengthening is approximately logarithmic for 3-4 decades in time. For sliding friction, the model reproduces many experimental observations. To capture the direct effect of these experiments, we need to endow the microscopic asperity-level friction law with a velocity-strengthening dependence. This does not, however, imply that the macroscopic response is velocity-strengthening. The velocity strengthening of individual contacts and the collective behavior together determine whether the macroscopic response is velocity-strengthening or weakening.

The power n in the local friction law plays a crucial role in the evolution of the friction coefficient. If $n > 1$, the static friction coefficient decreases with hold time and the transient evolution of sliding friction in velocity jump experiments happens in the same sense as the instantaneous change. Since we expect the power n to be less than or equal to 1, this explains why the above two features are not observed in experiments.

At the same time, the model appears to be too simple to reproduce all experimental observations. First, the strengthening of static friction with hold time saturates in 3-4 decades in our model. This is consistent with experiments on some materials but the strengthening persists for longer times in others. A complete understanding of this issue appears to be beyond the scope of this model. Second, our model results in velocity dependence of the characteristic evolution length scale D_c and parameter b that quantifies the transient change in friction in the rate and state equations, whereas these quantities are largely velocity-independent in experimental studies.

There are a number of ways to improve the model. In the present model, individual asperities are independent, the only interaction between them being through a mean field (dilatation). Long-range elastic interactions through the bulk may, however, play an important role. We have also assumed one of the surfaces to be rigid. While this is reasonable when one of the surfaces is much more deformable than the other, when the two surfaces are similar (with respect to deformability), it will be important to incorporate the non-rigidity, especially during sliding. We have neglected the spatial distribution of asperities and contacts; this will, however, be important for reproducing realistic frictional behavior, especially when the long-range interactions are incorporated. Depending on the material of the sliding surfaces, the model for a single asperity can be modified to incorporate effects such as plasticity, adhesion, etc. We explore some of these issues in the next chapters.

Chapter 3

Static and sliding contact of rough surfaces: effect of surface roughness, material properties, and long-range elastic interactions

Here, we study the static and sliding contact of three-dimensional rough surfaces with viscoelastic and viscoplastic material models and long-range elastic interactions between contacts. We present, as far as we know, the first sliding simulations of three-dimensional rough surfaces with long-range interactions. Simulations show that the qualitative features of static and sliding friction are determined by the material and surface properties and the long-range elastic interactions only change the results quantitatively.

3.1 Introduction

Most surfaces have roughness features at many length scales. To bridge the micro and macro scales, the smallest relevant length scales must be resolved while at the same time, the system must be large enough to be representative of a macroscopic body. A numerical method like the Finite Element Method, though useful to study the stress distribution at contacts, plasticity, and such, results in a large number of degrees of freedom [68, 69], and this can be especially intractable during sliding of surfaces. To overcome this, a boundary-element like method has been proposed in the literature, and many aspects of rough surface contact have been studied using this method [70, 71, 72, 73, 74, 75, 76]. However, as far as we know, time dependent behavior and sliding of rough surfaces has not been studied, and this is the main focus here.

As mentioned earlier, high stresses at the contacts result in time-dependent behavior of the materials. As a starting point, the model developed here considers viscoelastic material behavior.

Elastic fields are long-range, the displacement field due to a point load on the surface of an elastic half-space decays only inversely with the distance from the point of application. This means that when two rough surfaces are pushed against each other, the interactions between contacts can be important.

Here, we develop a model that considers all of the above mentioned effects. An important question to answer is: what role does each of the factors: material properties, surface roughness and elastic interactions, play in determining macroscopic friction?

3.2 Model

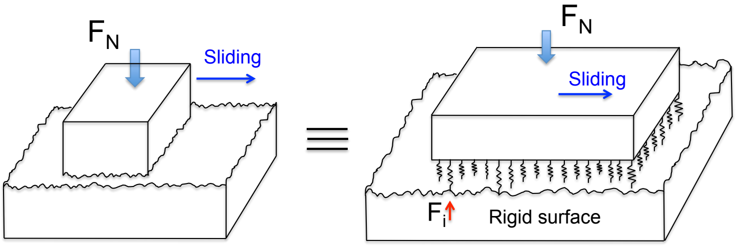

Figure 3.1: Contact of two rough surfaces; one of the rough surfaces is approximated by a set of discrete elements, the other surface is assumed to be rigid. The only degree of freedom of the elements is normal to the interface.

We consider the contact of two rough surfaces. We assume that one of the surfaces is rigid and represent the other surface by a set of discrete elements (Figure 3.1). The lengths of the elements are used to simulate the geometry of surfaces. The internal degrees of freedom of the discrete elements are the lengths normal to the interface.

For the elements, we assume constitutive equations of the form:

$$u_i(t) = \int_0^t \left(\sum_j C(t-\tau, r_{ij}) F_j(\tau) \right) \mathrm{d}\tau, \tag{3.1}$$

where $u_i(t)$ is the deformation of the element 'i' at time t, $F_j(\tau)$ is the force on element 'j' at time τ, $C(t-\tau, r_{ij})$ is the viscoelastic compliance kernel that captures the effect of the force at location 'j' at time τ on an element located at 'i' at time t, and r_{ij} is the distance between the two elements. Unless mentioned otherwise, the viscoelastic material behavior has a single relaxation timescale.

We consider two kinds of interactions between contacts. In the first, called the case with *no elastic interactions*, the deformation of an element u_i is unaffected by forces elsewhere:

$$\begin{aligned} u_i(t) &= \int_0^t C^0 \left[\delta(t-\tau) + Ae^{-\lambda(t-\tau)}\right] F_i(\tau)\mathrm{d}\tau \\ &= C^0 \left[F_i(t) + \int_0^t Ae^{-\lambda(t-\tau)} F_i(\tau)\right] \mathrm{d}\tau, \end{aligned} \tag{3.2}$$

where $\delta(t-\tau)$ is the Dirac delta function that captures the instantaneous elastic response, A is the amplitude of the viscoelastic effect, λ is the viscoelastic decay rate, and C^0 is the compliance of the elements. The second is the case with *Boussinesq interactions.* The Boussinesq solution gives the displacement (normal to the interface) at a point on the surface resulting from a distant point load on a homogenous, isotropic, linear-elastic half-space:

$$u(r) = \frac{1-\nu}{2\pi G}\frac{F}{r},$$

where G is the shear modulus of the half-space, ν is its Poisson ratio, and r is the distance to the point of force application. Following this and using superposition, we postulate:

$$u_i(t) = \frac{1-\nu}{2\pi G}\frac{1}{r_{ij}}F_j(t), \quad r_{ij} > 0.$$

For a linear viscoelastic half-space, using the correspondence principle, this becomes:

$$\begin{aligned} u_i(t) &= \int_0^t \frac{1-\nu}{2\pi G}\frac{1}{r_{ij}}\left(\delta(t-\tau)+Ae^{-\lambda(t-\tau)}\right)F_j(\tau)\mathrm{d}\tau \\ &= \frac{1-\nu}{2\pi G}\frac{1}{r_{ij}}\left[F_j(t)+\int_0^t Ae^{-\lambda(t-\tau)}F_j(\tau)\mathrm{d}\tau\right], \quad r_{ij}>0. \end{aligned} \tag{3.3}$$

The Boussinesq solution is singular at the point of application of the load, so the force F_i is interpreted not as a point load but as a distributed constant pressure over a rectangular area. The displacements caused by such a pressure distribution was derived by Love [77]. This solution, which has a number of logarithmic terms in it, is close to the Boussinesq solution even for neighboring elements, but is not singular at the point of loading. Thus, in computing the displacements at element 'j' due to a force at 'i', the Boussinesq solution is used for all $i \neq j$ and the Love solution for $i = j$. Together, equation (3.1) is obtained.

Each element, at a given instant, can either be in contact or out of contact with the rigid surface. If in contact, the following kinematic constraint is satisfied:

$$x_i(t) + y_i(t) = d(t),$$

where $x_i(t)$ is the length of the element at time t and equal to $x_i^0 + u_i(t)$, x_i^0 is the undeformed length, $u_i(t)$ is its deformation, $y_i(t)$ is the height of the rigid surface corresponding to the position of element 'i', and d is the dilatation, which is the separation between the reference levels from which the heights of the elements and the heights of the rigid surface are measured. When an element is out of contact with the surface, its force is $F_i(t) = 0$. Also, $F_i \leq 0$ since no tensile forces are allowed.

Two simplifying assumptions have been made in the formulation of this model. First, the Green's function (the Boussinesq solution) corresponds to the solution for a point force on a flat linear-elastic half-space. The presence of surface roughness and the finite size of the system will change the elastic solution. We also neglect the effect of the shear forces at the contacts. The shear forces would have an additional contribution to the normal deformations u_i of the elements. These issues remain a topic of current work.

3.2.1 Nondimensionalization

Using L^*, T^*, F^* to nondimensionalize length, time, and force, we get:

$$\bar{u} = \frac{u}{L^*}, \quad \bar{r}_{ij} = \frac{r_{ij}}{L^*}, \quad \bar{t} = \frac{t}{T^*}, \quad \bar{\tau} = \frac{\tau}{T^*}, \quad \bar{F} = \frac{F}{F^*}.$$

Equation (3.2) after nondimensionalization becomes:

$$\bar{u}_i(\bar{t}) = \bar{C}^0 \left[\bar{F}_i(\bar{t}) + \int_0^{\bar{t}} \bar{A} e^{-\bar{\lambda}(\bar{t}-\bar{\tau})} \bar{F}_i(\bar{\tau}) \right] \mathrm{d}\bar{\tau}, \tag{3.4}$$

where $\bar{A} = AT^*, \bar{\lambda} = \lambda T^*$, and $\bar{C}^0 = C^0 F^*/L^*$. For all simulations, $\bar{C}^0 = 16$ is used to make the total contact area about the same as the Boussinesq interaction case. Similarly, equation (3.3) becomes:

$$\bar{u}_i(\bar{t}) = \frac{(1-\nu)F^*}{2\pi G L^{*2}} \frac{1}{\bar{r}_{ij}} \left[\bar{F}_j(\bar{t}) + \int_0^{\bar{t}} \bar{A} e^{\bar{\lambda}(\bar{t}-\bar{\tau})} \bar{F}_j(\bar{\tau}) \mathrm{d}\bar{\tau} \right].$$

With $F^* = 2\pi G L^{*2}/(1-\nu)$, the above equation simplifies to:

$$\bar{u}_i(\bar{t}) = \frac{1}{\bar{r}_{ij}} \left[\bar{F}_j(\bar{t}) + \int_0^{\bar{t}} \bar{A} e^{-\bar{\lambda}(\bar{t}-\bar{\tau})} \bar{F}_j(\bar{\tau}) \mathrm{d}\bar{\tau} \right]. \tag{3.5}$$

The rms roughness for many surfaces is of the order of a micron [60], so we set $L^* = 1$ μm. We set the timescale $T^* = 1$ second. For rocks, G is around 30 GPa and ν is around 0.2. Using these values, $F^* = 0.235$ N ≈ 0.25 N. After nondimensionalization, there are two nondimensional constants: the decay rate $\bar{\lambda}$ and the amplitude $\bar{A}$.

To understand the effect of these parameters, let us consider a force $\bar{F}_j(\bar{t}) = \bar{F}_j^0 H(\bar{t})$, where $H(\bar{t})$ is the Heaviside function. For $\bar{t} > 0$,

$$\bar{u}_i(\bar{t}) = \frac{1}{\bar{r}_{ij}} \left[1 + \frac{\bar{A}}{\bar{\lambda}} \left(1 - e^{-\bar{\lambda}\bar{t}} \right) \right] \bar{F}_j^0.$$

If $\bar{t} \ll 1/\bar{\lambda}$,

$$\bar{u}_i(\bar{t}) \approx \frac{1}{\bar{r}_{ij}} \bar{F}_j^0,$$

and for $\bar{t} \gg 1/\bar{\lambda}$,

$$\bar{u}_i(\bar{t}) \approx \frac{1}{\bar{r}_{ij}} (1 + \bar{A}/\bar{\lambda}) \bar{F}_j^0.$$

Thus, the instantaneous compliance of the system is $1/\bar{r}_{ij}$, the steady state compliance is $(1 + \bar{A}/\bar{\lambda})/\bar{r}_{ij}$, and the deformation reaches steady state at the decay rate $\bar{\lambda}$.

For a finite number of viscoelastic relaxation timescales, equations (3.4) and (3.5) become:

$$\bar{u}_i(\bar{t}) = \bar{C}^0 \delta_{ij} \left[\bar{F}_j(\bar{t}) + \int_0^{\bar{t}} \sum_{k=1}^{N_T} \bar{A}_k e^{-\bar{\lambda}_k(\bar{t}-\bar{\tau})} \bar{F}_j(\bar{\tau}) \mathrm{d}\bar{\tau} \right] \text{ (no elastic interaction)} \tag{3.6}$$

and

$$\bar{u}_i(\bar{t}) = \frac{1}{\bar{r}_{ij}} \left[\bar{F}_j(\bar{t}) + \int_0^{\bar{t}} \sum_{k=1}^{N_T} \bar{A}_k e^{-\bar{\lambda}_k(\bar{t}-\bar{\tau})} \bar{F}_j(\bar{\tau}) \mathrm{d}\bar{\tau} \right] \text{ (Boussinesq interaction),} \tag{3.7}$$

where N_T is the number of relaxation timescales, $\bar{A}$ and $\bar{\lambda}$ are the viscoelastic decay amplitudes and decay rates, respectively. In the Boussinesq interaction case, the material properties appear naturally in the constitutive equation, since it is derived from an elastic solution. For the case with no elastic interactions, $\bar{C}^0$ is an effective compliance parameter.

3.2.2 Algorithm

Differentiating equations 3.6 or 3.7 results in a set of coupled ordinary differential equations that are the governing equations. Let us consider equation 3.7. Differentiating with respect to nondimensionalized time, we get:

$$\dot{\bar{u}}_i = \frac{1}{\bar{r}_{ij}} \left[\dot{\bar{F}}_j + \int_0^{\bar{t}} \sum_{k=1}^{N_T} (-\bar{\lambda}_k \bar{A}_k) e^{-\bar{\lambda}_k(\bar{t}-\bar{\tau})} \bar{F}_j(\bar{\tau}) \mathrm{d}\bar{\tau} + \left(\sum_{k=1}^{N_T} \bar{A}_k \right) \bar{F}_j(\bar{t}) \right]. \tag{3.8}$$

As mentioned earlier, since $1/\bar{r}_{ij}$ is singular for $i = j$, it is replace by C_{ij} which is obtained by combining Boussinesq and Love solutions.

$$\dot{\bar{u}}_i = C_{ij}\left[\dot{\bar{F}}_j + \int_0^{\bar{t}} \sum_{k=1}^{N_T}(-\bar{\lambda}_k\bar{A}_k)e^{-\bar{\lambda}_k(\bar{t}-\bar{\tau})}\bar{F}_j(\bar{\tau})\mathrm{d}\bar{\tau} + \left(\sum_{k=1}^{N_T}\bar{A}_k\right)\bar{F}_j(\bar{t})\right]. \tag{3.9}$$

We use a first-order Euler method in evolving the equations. The contact conditions of the elements (in or out of contact) can change during the evolution. This is updated in an explicit way.

Given the current state (dilatation, the deformations and forces of all the elements and other variables that keep track of the history in the viscoelastic case), the elements in and out of contact are assumed to remain that way during a time step Δt. The steps in the evolution of a single time step are:

1. Given the dilatation rate $\dot{\bar{d}}$, for the elements in contact, determine the deformation rate from the kinematic constraint:

   $$\dot{\bar{u}}_i = \dot{\bar{d}} - \dot{\bar{y}}_i.$$

   The rate of change of the rigid surface height, $\dot{\bar{y}}_i$, is zero for static contact but nonzero during sliding.

2. For the elements not in contact, the force remains zero:

   $$\dot{\bar{F}}_i = 0.$$

3. Determine the deformation rate of elements not in contact and the rate of force for the elements in contact using the governing equations.

4. Update the forces, deformations and other internal variables that keep track of the history.

5. Use the kinematic constraint and the non-negativity of force as checks for transitions into and out of contact, respectively.

When the total normal force is to be held constant, the dilatation rate $\dot{d}$ is determined to satisfy the constraint.

3.2.3 Computational Memory and Complexity considerations

In the Boussinesq interaction case, because the deformation due to a point force decays only as $1/r$, the compliance matrix C_{ij} is dense and for a large system, storing the matrix entries can lead to large memory requirements. We circumvent this by computing the matrix vector product $C_{ij}F_j$ in a matrix free way and using an iterative solver (GMRES) [78] when a linear system is to be solved. The other issue is the computation of the matrix vector product. Again, because of the long-range $1/r$ decay, a brute force computation of the interactions involves $O(N^2)$ operations where N is the number of elements, and this can be prohibitively expensive for large systems. Two things come to our rescue here. First, for rough surfaces, the actual area of contact is only a small fraction of the nominal area, so at any instant of time, the forces are nonzero for only a small fraction of the elements and only these need to be considered in computing the displacements. Second, the $1/r$ interactions can be computed to within prescribed error tolerance in $O(N\log(N))$ operations using the Fast Multipole Method (FMM) [79, 80]. In all results presented here, we use an FMM method of order 5, since this seems sufficient on comparison with a brute force calculation.

3.2.4 Rough surface generation

Rough surfaces can be characterized as a stochastic process [81, 56, 57]. This characterization is used extensively in exploring various aspects of contact between surfaces [26, 58, 59]. The process is specified by two functions: a probability distribution of heights, which describes features normal to the interface, and an autocorrelation function, which is related to how the vertical features vary along the interface. For many surfaces, the probability distribution of heights is Gaussian:

$$P(z) = \frac{1}{\sigma\sqrt{2\pi}} e^{-z^2/2\sigma^2},$$

where z is the height of a surface from the mean, $P(z)$ is the probability density, and σ is the root mean square roughness [60]. The autocorrelation is found to decay exponentially or as a Gaussian [60, 82]. Here, we consider surfaces with a Gaussian autocorrelation:

$$R(\delta_x, \delta_y) =< z(x, y)z(x + \delta_x, y + \delta_y) >= \sigma^2 e^{-(\delta_x^2/\beta_x^2+\delta_y^2/\beta_y^2)},$$

where R is the autocorrelation function, β_x, β_y are the correlation lengths along x and y directions, and $<>$ denotes expectation with respect to the probability distribution. For such surfaces, the power spectral density S (which is the Fourier transform of the autocorrelation) as a function of the spatial frequencies ω_x, ω_y is given by:

$$S(\omega_x, \omega_y) = \frac{1}{2}\sigma^2 \beta_x \beta_y e^{-(\beta_x^2\omega_x^2+\beta_y^2\omega_y^2)/4}.$$

Rough surfaces with these statistical properties can be generated by generating a set of independent Gaussian random numbers and using a linear filter [83]. The weights of the linear filter are determined from the autocorrelation. Figure 3.2 shows one realization of such a surface, the probability distribution of heights, and the autocorrelation of generated surfaces. Also shown are the prescribed statistical properties. The generated surfaces show a good match with respect to the prescribed properties.

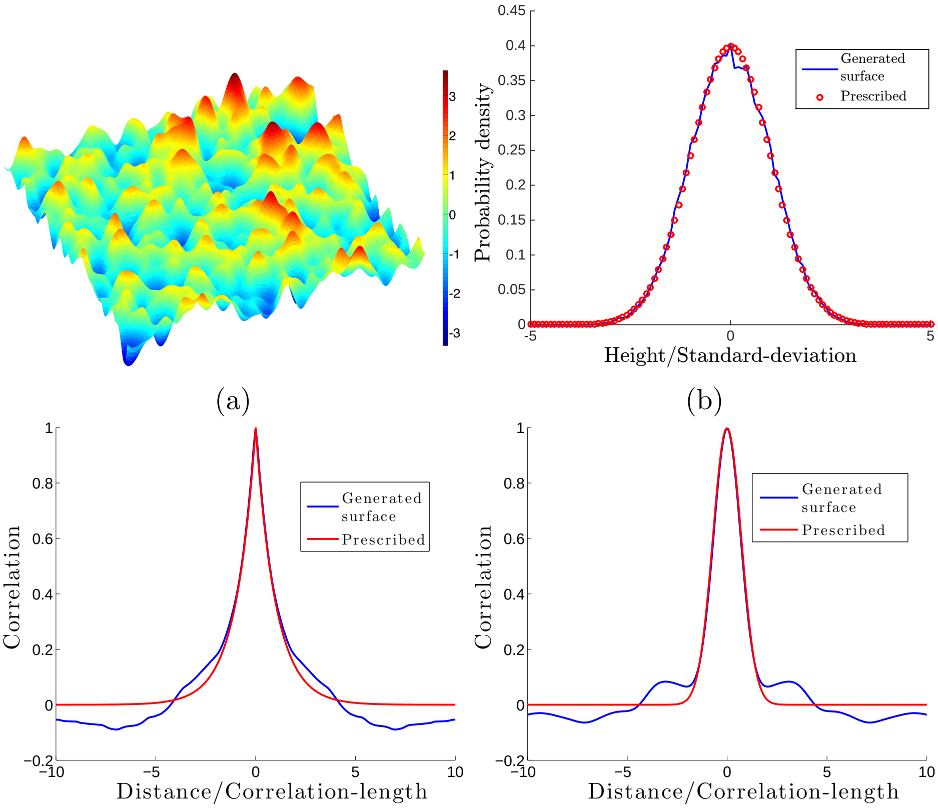

(a) (b)

(c) (d)

Figure 3.2: (a) Rough surface with a Gaussian distribution of heights and a Gaussian autocorrelation. Statistical properties of the generated surfaces: (b) probability density (Gaussian) of heights, (c) exponential spatial correlation, and (d) Gaussian spatial correlation.

Unless mentioned otherwise, the surfaces generated here have a Gaussian distribution of heights with zero mean, a root mean square roughness $\sigma = 1$ μm, and a Gaussian autocorrelation with correlation lengths $\beta_x = 10$ μm and $\beta_y = 10$ μm.

3.3 Validation using Hertzian contact

To validate our formulation, we simulate the Hertzian contact of a homogenous linear-elastic sphere of radius 10 with a rigid flat surface. The geometry of the sphere is simulated using the undeformed lengths of the elements. The two surfaces are initially apart, and the force and deformations of all the elements are initialized to zero. The surfaces are then brought into contact by decreasing the dilatation. The evolution of the deformations and forces of the elements is computed.

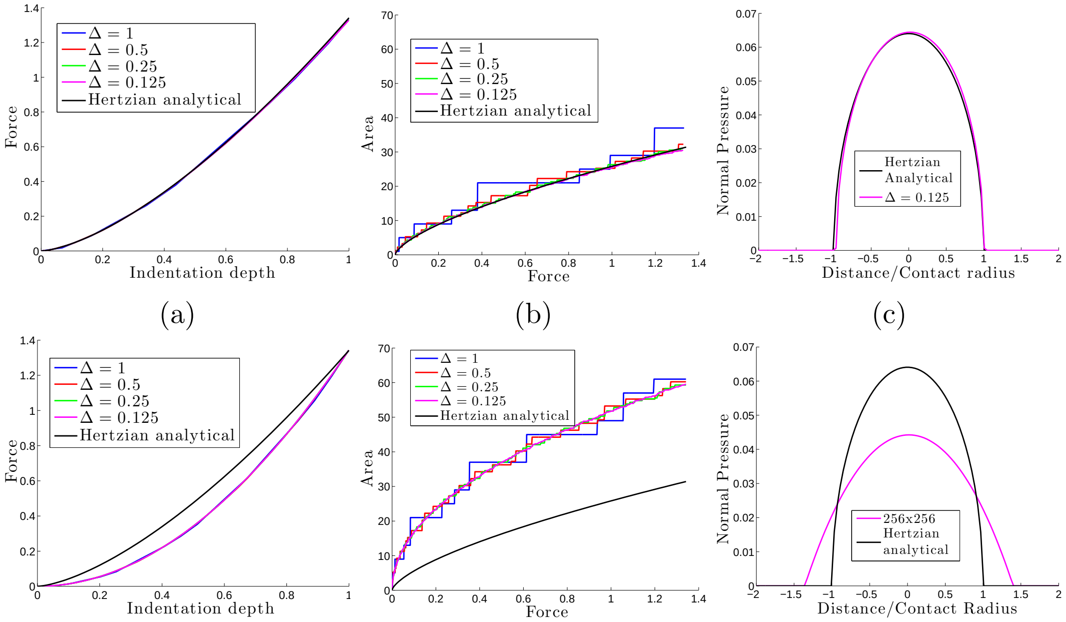

(a) (b) (c)

(d) (e) (f)

Figure 3.3: Comparison of analytical and numerical solutions for contact of a linear-elastic sphere against a rigid flat: (top row) with Boussinesq interaction; (bottom row) with no elastic interaction. Lines of different colors correspond to different discretization sizes Δ, the distance between the discrete elements.

In the Boussinesq interaction case, there is an excellent match between the numerical and analytical solutions (Figure 3.3). The elastic constants used in the analytical and numerical solutions are the same and no other parameters are used in obtaining the numerical results. For the case with no elastic interaction, $\bar{C}^0$ is chosen to make the force at the final indentation match the analytical solution. The scaling of the force and area deviates from the Hertzian solution.

3.4 Static contact

Here, we study the static contact of rough surfaces. We consider the contact between a flat linear viscoelastic surface ($\bar{\lambda} = 1, \bar{A} = 0.2$) and a rough rigid surface, both 512×512 in size. The rough surface is generated as described in Section 3.2.4. The surfaces, initially apart, are loaded instantaneously to a total force that corresponds to a nominal pressure of 100 MPa. The system is then evolved, keeping the global normal force constant. The evolution of the forces, deformations, and the contact area is computed.

3.4.1 Evolution of contact and force distribution

After the initial compression, the forces at the contacts start relaxing because of the viscoelastic behavior. To keep the global force constant, more contacts are formed and the contact area increases. Just as in experiments [41], existing contacts grow with time, some contacts coalesce and some new ones are formed (Figure 3.4).

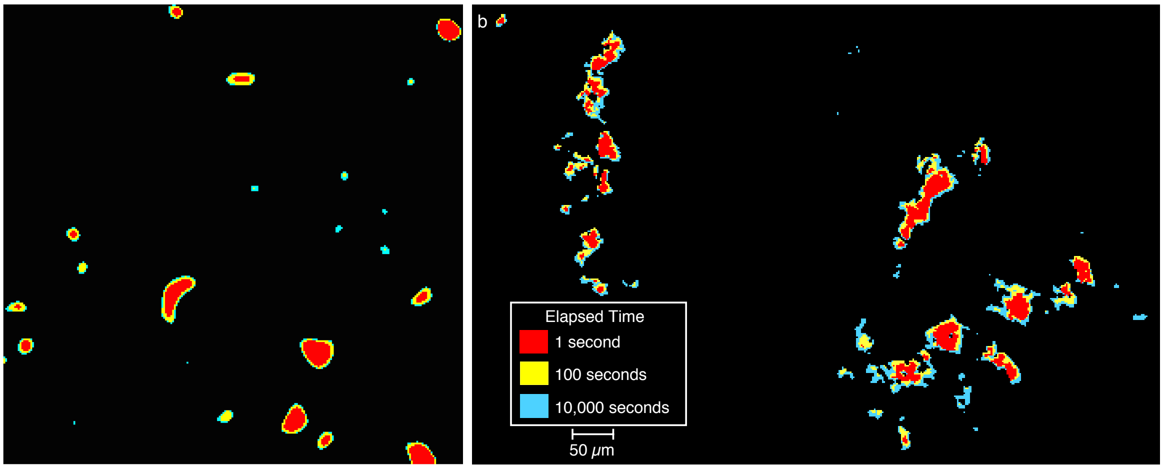

(a) (b)

Figure 3.4: Evolution of contacts in (a) our simulations, and (b) experiments [41], during a static contact test. In (a), contacts at $\bar{t} = 0$ are in red, $\bar{t} = 10$ are in yellow, and $\bar{t} = 100$ are in cyan. Existing contacts grow, some coalesce, and some new contacts are formed. (b) is reproduced with permission from [41].

As the contact forces relax and contact area increases, the force distribution spreads, and the force per unit contact area decreases. (Figure 3.5a). The first moment of the force distribution, which is the total normal force, is the same for initial and final states. The zeroth moment (area under the curve), which is the total contact area, is larger at the final state.

Even though the total contact area increases, the average contact radius, calculated as $\sqrt{\text{Contact area}/(\pi \times \text{Number of contacts})}$, remains nearly constant (Figure

3.5b). The average contact radius is close to 5 and the maximum variation is about 0.5. This is because, with time, as the contact area increases, the number of contacts also increases, keeping the average contact radius approximately constant. A similar observation was made by Greenwood and Williamson in their statistical model of elastic contacts [26].

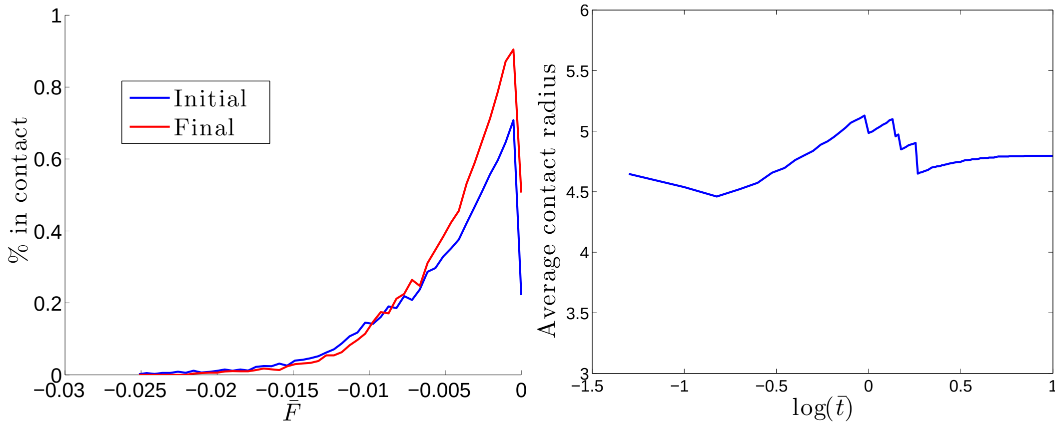

(a) (b)

Figure 3.5: (a) Distribution of contact forces at the initial and steady states. Initially, the area of contact is lower but the average force on a contact is higher. With time, as the forces relax, the number of contacts increases but the average force per contact decreases. (b) Evolution of the average contact size with time. Even though the total contact area increases, the average contact size does not change significantly.

3.4.2 Dilatation, area, and friction evolution

As the contact forces relax, dilatation decreases (the surfaces move closer to each other) and the contact area increases (Figure 3.6). With either of the interactions (Boussinesq or no elastic), the duration and magnitude of area growth are approximately the same .

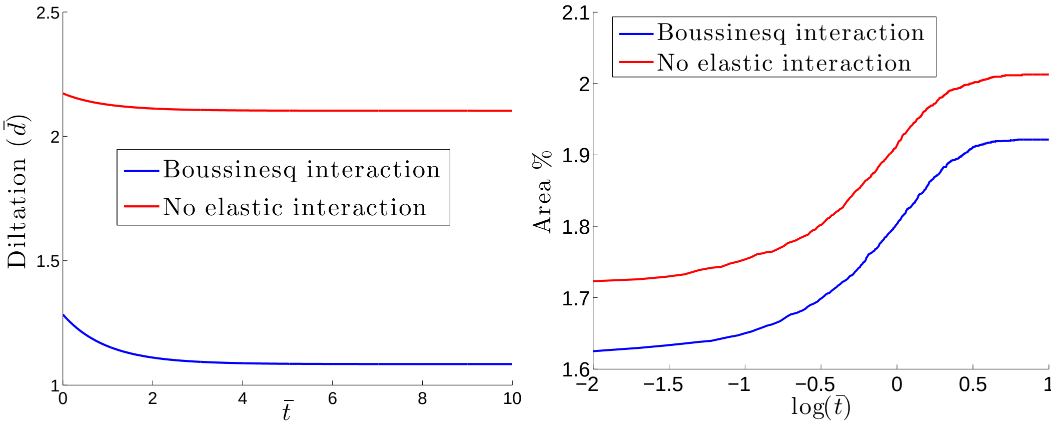

(a) (b)

Figure 3.6: Evolution of (a) dilatation and (b) contact area with the time of contact. Because of viscoelastic relaxation, the surfaces move closer and the area of contact increases with time.

If the shear strength of each contact is τ_s, then the static friction coefficient μ_s is,

$$\mu_s(t) = \frac{F_S(t)}{F_N} = \frac{\tau_s A_r(t)}{\sigma_N A_N},$$

where F_S is the global shear force, F_N is the global normal force, A_r is the actual area of contact, A_N is the nominal area of contact, and σ_N is the nominal compressive stress. The shear stress at the contact can be a significant fraction of the shear modulus [54, 84], and we use $\tau_s = 2.5$GPa. In the simulations, the friction coefficient increases with time, logarithmically for a period of time, and saturates to a steady value at long times (Figure 3.7a).

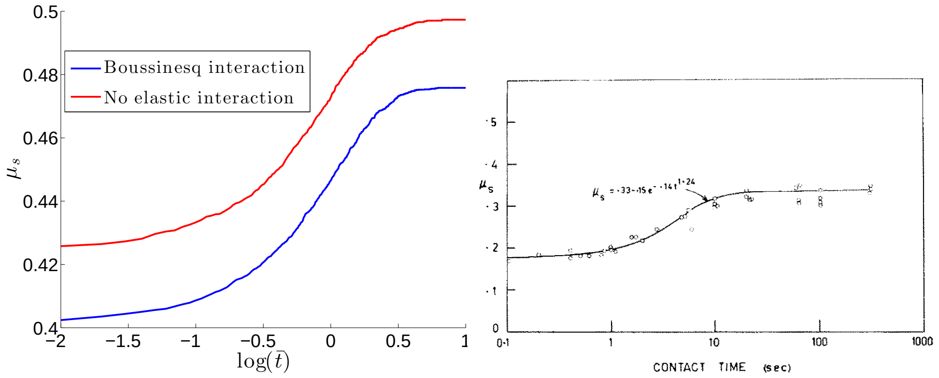

(a) (b)

Figure 3.7: Evolution of static friction coefficient with time in our simulations (a) with Boussinesq and no elastic interactions and (b) experiments of Richardson et al. (reproduced with permission from [39]). For some duration, the growth is logarithmic in time and saturates to a steady state at long times. The timescale and the magnitude of evolution are unchanged by the presence of long-range Boussinesq interactions.

The predicted increase of the static friction coefficient with time has been widely observed in experiments [32, 40, 39]. In our simulations, the variation in μ_s lasts about 2 decades in time. In some materials like mild steel, a similar duration of static friction growth, with saturation at small and long times, is observed [39], as shown in Figure 3.7b. Thus, our results are consistent with these experimental observations.

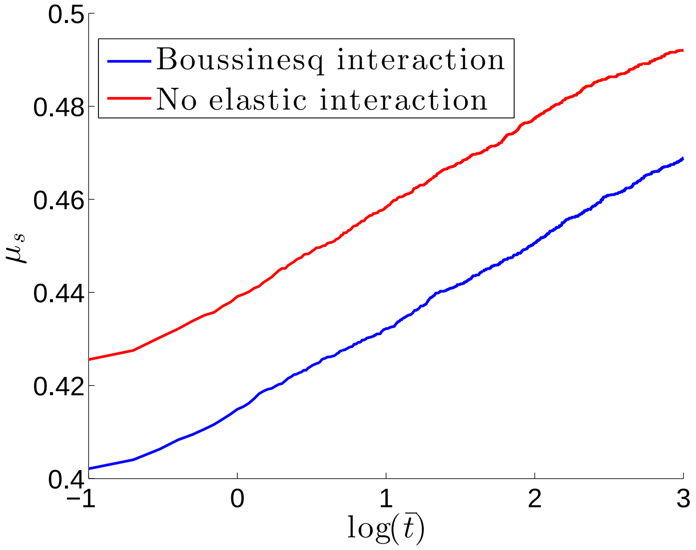

Figure 3.8: Evolution of friction coefficient during static contact for a material with four viscoelastic timescales. The region of logarithmic growth lasts over 4 decades, as seen in experiments on rocks.

In experiments on rocks, the logarithmic growth persists throughout the duration of the experiments, which have lasted up to six decades in time [40, 33]. Since μ_s cannot increase indefinitely, it eventually has to reach a steady state. This delayed saturation is not captured by our model. We conjecture that the difference between our model response and the rock experiments is for the following reason. The constitutive relation we assume has only one relaxation time, while a real viscoelastic material has many relaxation timescales. Longer timescales of relaxation lead to longer times of growth in contact area and hence friction. To test this, we repeat the static contact test for a material with four viscoelastic relaxation timescales ($N_T = 4, \bar{\lambda}_k = 1, 0.1, 0.01, 0.001, \bar{A}_k = 0.05, 0.005, 0.0005, 0.00005$). The linear growth regime of friction now extends over 4 decades in time, as seen in the experiments on rocks (Figure 3.8).

In Chapter 2, we conjectured that the presence of elastic interactions between contacts will increase the timescale of friction evolution. Our simulations show that the elastic interactions do not change the qualitative features of the macroscopic friction evolution. In Figure 3.7a, the friction growth, with and without elastic interactions, saturates at about $\bar{t} = 10$. The magnitude of the change in friction is also about the same for the two cases.

3.4.3 Dependence on normal pressure and system size

Friction coefficient is known to be independent of the normal force for macroscopic rough surfaces (Amontons law). In the Bowden and Tabor model, this is explained by the plasticity of contacts [30] whereas in the Greenwood Williamson (GW) model, this is a result of the statistics of the rough surface [26]. The GW model ignores interactions between contacts which might be important. Our model exhibits the same behavior. Both with and without elastic interactions, the friction coefficient is nearly independent of the applied normal pressure (Figure 3.9).

Since the elastic interactions are long-range, the friction coefficient can be dependent on the system size. Surprisingly, even for small system sizes (our nondimensionalizing length is 1 μm, and thus the systems sizes considered are 128 μm, 256 μm, and 512 μm), the friction coefficient is nearly independent of the system size.

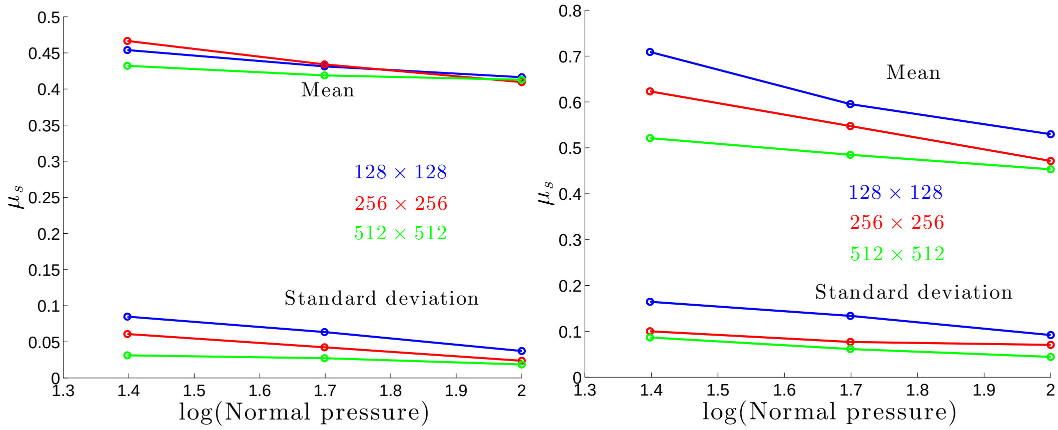

(a) (b)

Figure 3.9: Dependence of friction coefficient on normal pressure for three system sizes with (a) Boussinesq and (b) No elastic interactions. The mean and the standard deviation for 15 realizations for each case is shown. Considering the mean and the standard deviation, the friction coefficient is independent of both the system size and the applied nominal pressure.

3.4.4 Dependence on surface roughness

In our model, the static friction coefficient decreases monotonically with increasing roughness (Figure 3.10a). A similar dependence on roughness is seen in experiments for a certain range of roughness (see page 62-63 of [32]). At higher values of roughness, the friction coefficient in experiments first becomes nearly independent, and then increases with increasing roughness [32]). This is usually attributed to plasticity and ploughing (having to lift one asperity over an other), neither of which is considered in our model. The predictions here are entirely due to the change in contact area with roughness.

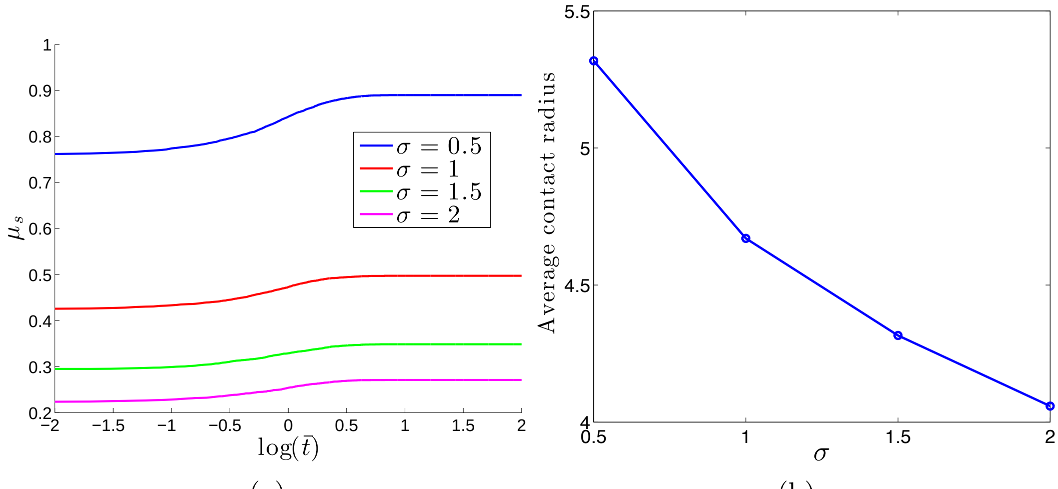

(a) (b)

Figure 3.10: (a) Dependence of friction coefficient on the rms roughness of the contact surfaces. μ_s decreases with increasing roughness, consistent with some experiments for a range of roughness. (b) The average contact size decreases with increasing rms roughness.

Simulations also show that the average contact size decreases with increasing roughness (Figure 3.10b). This means that the average contact stress increases with increasing roughness. In Figure 3.10, the total contact area (friction coefficient is proportional to total contact area) depends more strongly on σ than the average contact radius. In going from $\sigma = 0.5$ to $\sigma = 2$, the friction coefficient at steady state decreases approximately by a factor of 3.3, whereas the average contact radius decreases by about 1.3. This means that the number of contacts decreases by a factor of about 2.

Since there are no plasticity effects in the model, the contact stresses can increase unboundedly. We conjecture that including plasticity will lead to a weaker dependence on rms roughness since the stresses are then bounded by the yield stress.

3.4.5 Dependence on viscoelastic properties

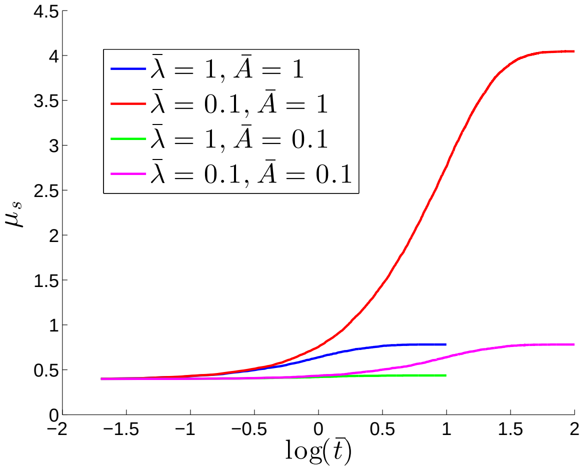

Figure 3.11: Evolution of friction coefficient for four different combinations of viscoelastic parameters. The timescale of evolution is determined by $\bar{\lambda}$, and the difference between initial and final states is determined by the ratio $\bar{A}/\bar{\lambda}$.

To study the dependence of friction evolution of the viscoelastic properties, we perform static contact simulations for four different combinations of the parameters $\bar{\lambda}$ and $\bar{A}$. Figure 3.11 shows the evolution of friction coefficient for the four cases. The pink and red curves (both have $\bar{\lambda} = 0.1$) reach steady state at about the same time, but the magnitude of the change in area is different. Similarly for the blue and green curves (both have $\bar{\lambda} = 1$). This tells us that the timescale of evolution of area and friction is determined by $\bar{\lambda}$. Comparing the blue and pink curves, the steady state stiffness is determined by the ratio $\bar{A}/\bar{\lambda}$. Thus, $\bar{\lambda}$ determines how long it takes to reach steady state, and $\bar{A}/\bar{\lambda}$ determines the magnitude of the difference between the initial and final states, as expected from Section 3.2.1. The initial value of friction is determined by the instantaneous stiffness of the system (stiffness corresponding to fast loading rates) and is hence independent of the viscoelastic properties.

3.5 Sliding contact

Let us move on to the sliding contact of rough surfaces. For sliding, the rigid surface must be larger than the deformable one. The results presented here are for a

512×512 deformable rough surface sliding on a larger 512×1024 rigid rough surface with the distance between the elements, Δ, is 1. During sliding, the heights of the rigid surface in between its discretized heights are computed using a cubic spline interpolation along the sliding direction. As the surfaces slide, the governing equations and the surface topography determine the evolution of forces and deformations of the elements.

3.5.1 Evolution of contacts

As an element slides, its deformation and force evolve depending on the surface profile it encounters (Figure 3.12). The element is initially out of contact and force is zero. As it slides, it repeatedly comes into and goes out of contact with the surface. The corresponding force evolution is also shown. The oscillations in the element height in the region marked as 1 are from the oscillations in the dilatation (to keep the normal force constant). In the region marked 2, the element is out of contact but its height is still changing. This is because of the long-range elastic interactions, the deformation caused by perhaps a neighboring element in contact.

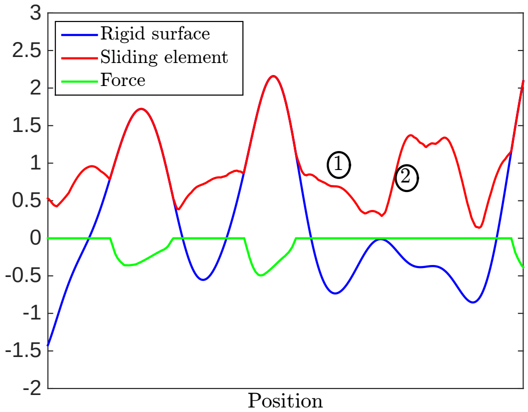

Figure 3.12: Evolution of a single element as it slides along a rough surface. The element is initially out of contact and the force is zero. As it slides, it repeatedly comes into and goes out of contact with the rigid surface, and correspondingly the force on it also evolves.

Figure 3.13b shows the evolution of forces on a subset of the elements of the surface during sliding. The subset of elements considered is marked by a red box in Figure 3.13a. Different aspects of the evolution of the contacts during sliding are apparent in the figure: some new contacts are formed, some existing ones grow, and some dwindle and go out of contact.

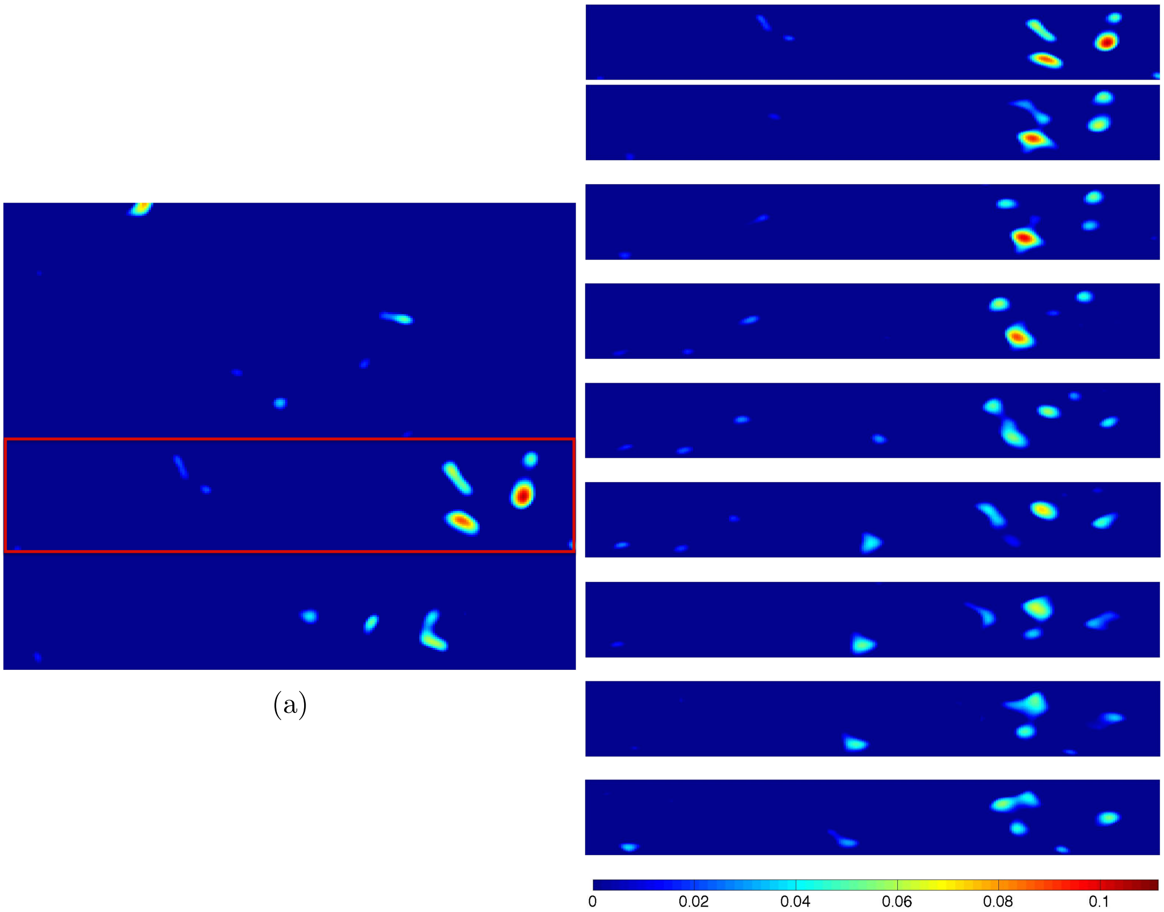

(a)

(b)

Figure 3.13: Evolution of forces on a subset of the elements of the surface during sliding. The subset of elements considered is marked by a red box in (a) and its evolution is shown in (b).

From the evolution of the elements, to calculate the friction coefficient, the following friction law is used:

$$\mu(\bar{t}) = \frac{\left[a \ln(\bar{v}) + \tau_s\right] A_r(\bar{t})}{F_N}. \tag{3.10}$$

As before, the shear strength of each contact is τ_s. The force necessary to overcome this is $\tau_s A_r(\bar{t})$. Thus, the contribution of this to the friction coefficient is $\tau_s A_r(\bar{t})/F_N$. If the surfaces are sliding at speed $\bar{v}$, the contacts are sheared at a strain rate that is proportional to the sliding speed and the shearing force can depend on the strain rate. This is accounted for by the logarithmic term $a \ln(\bar{v}) A_r(\bar{t})/F_N$ [84].

3.5.2 Velocity jump test

As in experiments, we perform velocity jump simulations. Two rough surfaces are brought into contact to a total force equivalent to a nominal pressure of 100 MPa. The surfaces then slide at this constant normal force at speed $\bar{v} = 10$. The sliding velocity is then instantaneously changed to $\bar{v} = 1$. Jumps to $\bar{v} = 10$ and $\bar{v} = 1$ are repeated. Since the nondimensionalizing length and time scales are 1μm and 1 second, respectively, $\bar{v} = 10$ corresponds to a sliding speed of 10μm/s, and sliding speed in most velocity jump experiments is around this value [41].

Figures 3.14a shows the evolution of contact area during the jump test for two different sets of parameters, $\bar{\lambda} = 1, \bar{A} = 1$ (blue), and $\bar{\lambda} = 1, \bar{A} = 10$ (red). In both cases, the area of contact is smaller at higher speeds. Because of viscoelasticity, the forces at the contacts depend on the sliding speed (which can be thought of as a strain rate for the viscoelastic elements). At higher sliding speeds, the average force on a contact is higher and thus, to sustain the same global normal force, the actual area of contact necessary is smaller than that at a lower sliding speed. Therefore, on jumping from a low speed to a higher speed, the contact area gradually decreases and reaches a steady state corresponding to the new sliding speed.

The friction coefficient changes instantaneously (Figure 3.14b) when the velocity jumps because of the logarithmic term in equation (3.10), and the change has the same sense as that of the velocity jump, i.e., the friction coefficient jumps up (down) when the velocity jumps up (down). Following the standard rate and state terminology, we call this jump the *direct effect*. This jump is followed by an evolution towards a steady state (because of the evolution of contact area). We call this the *transient*. In both cases, this transient changes the friction coefficient in the direction opposite to the direct effect, i.e., the friction coefficient decreases from the high value following a jump up and increases from a low value following a jump down.

In one case (blue), the transient is smaller than the direct effect so that the steady state friction is higher (lower) for higher (lower) velocity. This represents *velocity strengthening* behavior. In the other case (the red curve), the transient is larger than the direct effect so that the steady state value is lower (higher) for higher (lower) velocity. This represents *velocity weakening* behavior. The evolution of area and friction coefficient in our simulations and experiments are qualitatively similar (Compare figures 3.14a, 3.14b and 3.14c).

The qualitative aspects of the response remain unchanged when the elastic interactions are turned off (Compare figures 3.14a and 3.14b, and 3.14d and 3.14e) During sliding, the evolution of area and friction, velocity-strengthening, and velocity-weakening are determined largely by the viscoelastic properties and are only quantitatively changed by the long-range elastic interactions.

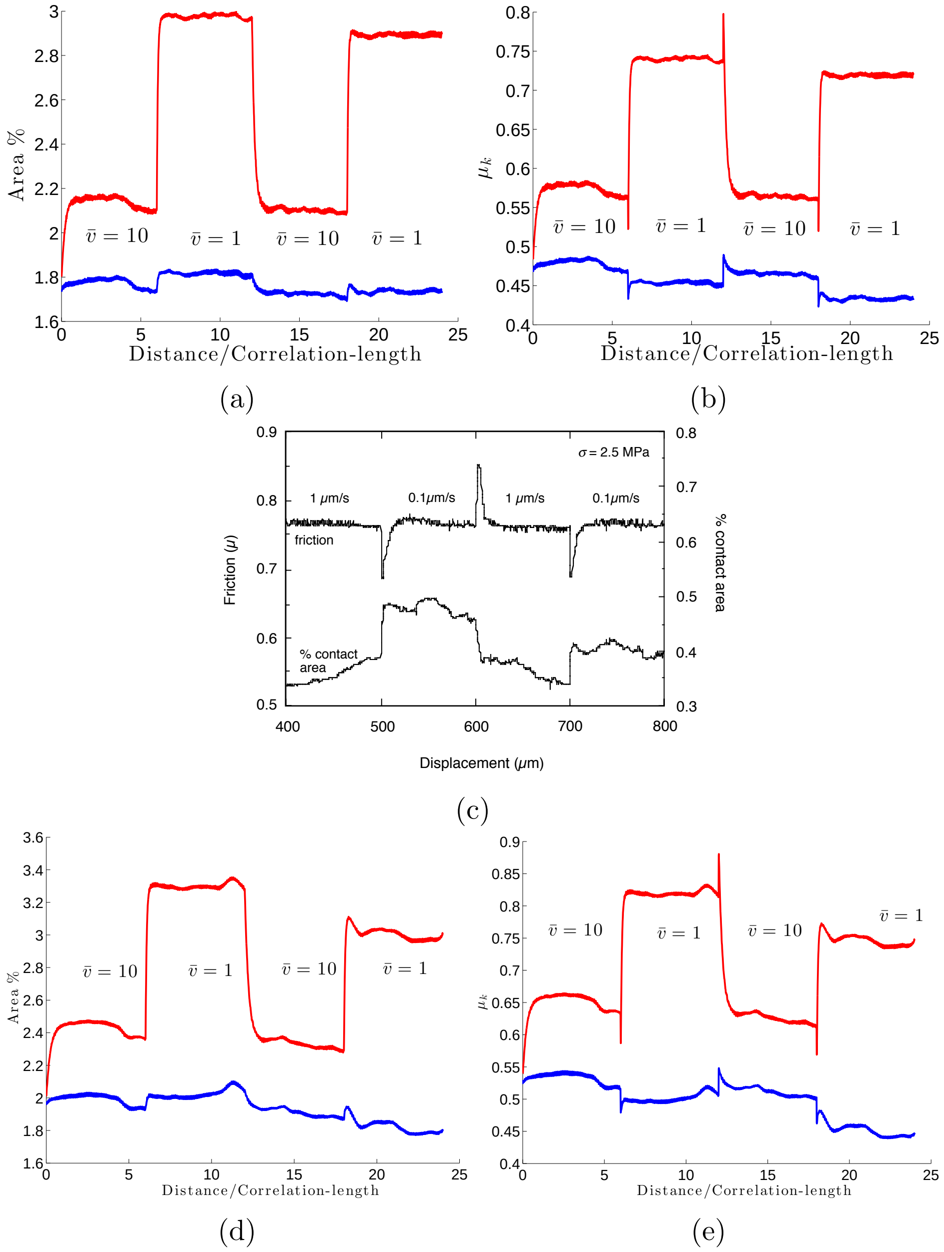

(a) (b) (c) (d) (e)

Figure 3.14: Evolution of contact area and friction coefficient (μ_k) during velocity jump tests with $\bar{\lambda} = 1, \bar{A} = 1$ (blue) and $\bar{\lambda} = 1, \bar{A} = 10$ (red). (a) Because of viscoelasticity, the average force on a contact is higher at higher speeds, and thus for the same global normal force, contact area is smaller at higher speeds. (b) With a jump in sliding speed, μ_k changes instantaneously, and this is followed by an evolution to a steady state. Depending on the material parameters, the steady state value can increase or decrease with increasing sliding speed. The two cases correspond to velocity-strengthening (blue) and velocity-weakening (red), respectively. (c) Evolution of contact area and friction during a velocity jump test (reproduced with permission from Dieterich [41]). (d) and (e) Evolution of contact area and friction coefficient for the case with no elastic interaction. The qualitative behavior is the same as (a) and (b).

3.5.3 Dependence on velocity and viscoelasticity

The two timescales involved during sliding contact are the viscoelastic relaxation timescale, determined by $\bar{\lambda}$, and the timescale corresponding to the ratio of the correlation length to the sliding speed, $\beta/\bar{v}$. In static contact, the duration of friction evolution was determined by $\bar{\lambda}$ and the magnitude of the growth by $\bar{A}/\bar{\lambda}$ (Section 3.4.5). During sliding, instantaneous and steady state behavior of static contact are like sliding at very high and very low speeds. Thus, $\bar{\lambda}$ determines where the system is sensitive with respect to sliding speed and $\bar{A}/\bar{\lambda}$ determines the magnitude of the sensitivity.

To study the velocity dependence, two rough surfaces are compressed to a nominal pressure of 100 MPa and starting at the same initial state, slid at different speeds till they reach steady state. With increasing sliding speed, dilatation always increases and the contact area always decreases (Figure 3.15). The friction coefficient can either increase or decrease, depending on whether the direct effect or the transient change dominates.

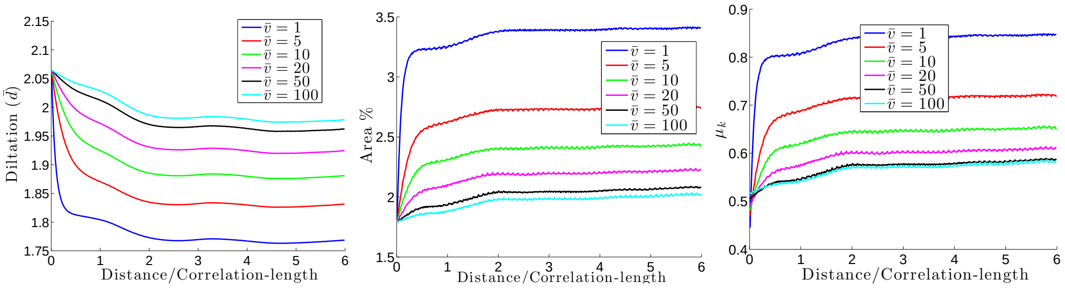

(a) (b) (c)

Figure 3.15: Evolution of (a) dilatation, (b) contact area, and (c) friction coefficient starting from the same initial state and sliding at different speeds. At higher sliding speeds, the average force on a contact is higher and thus, to sustain the same global normal force, the dilatation is higher and the total area of contact is smaller. The friction coefficient can either increase or decrease with the sliding speed (Section 3.5.2).

The distribution of forces at the contacts depends on the sliding speed (Figure 3.16). The percentage area in contact, which is the area under the curve, is smaller at higher speeds. The same global normal force is sustained at lower speeds by a larger area of contact but the average force is smaller. At higher speeds, the contact area is smaller but the average force is larger.

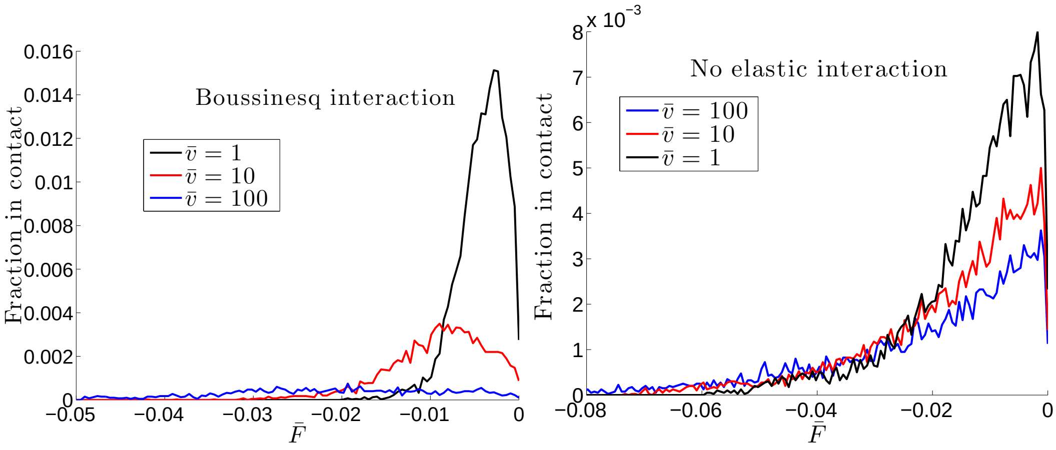

(a) (b)

Figure 3.16: Force distribution at contacts at steady state at different sliding speeds. The area under the curve is less than 1, since only a small percentage of the nominal area is in contact.

In static contact, the average contact radius remained nearly constant during the evolution. In sliding contact, the average contact size decreases with increasing sliding speed (Figure 3.17).

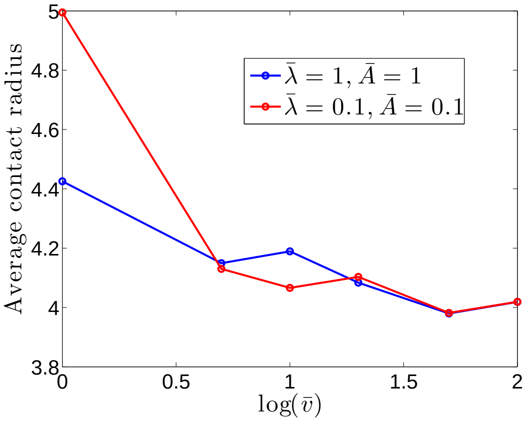

Figure 3.17: Variation of the average contact size at steady state and different sliding speeds.

The velocity-strengthening and velocity-weakening behavior is determined by the magnitude of the sensitivity of the system to velocity changes as compared to the direct effect. This sensitivity depends on the viscoelastic properties. To study the dependence on the viscoelasticity, sliding simulations with four combinations of the viscoelastic parameters $\bar{\lambda}, \bar{A}$ are performed. The steady state contact area always decreases with increasing speed but the magnitude of this variation depends on $\bar{A}/\bar{\lambda}$ (Figure 3.18a). For the case $\bar{\lambda} = 0.1, \bar{A} = 1$, $\bar{A}/\bar{\lambda} = 10$, and the area changes are larger than the other cases.

The steady state friction coefficient can either increase or decrease with increasing speed depending on $\bar{\lambda}, \bar{A}$ and the magnitude of the direct effect (a in Equation 3.10). For example, in Figure 3.18b , for $\bar{\lambda} = 0.1, \bar{A} = 1$, the system is velocity-weakening at most sliding speeds while for $\bar{\lambda} = 1, \bar{A} = 0.1$, the system is velocity-strengthening at all the sliding speeds.

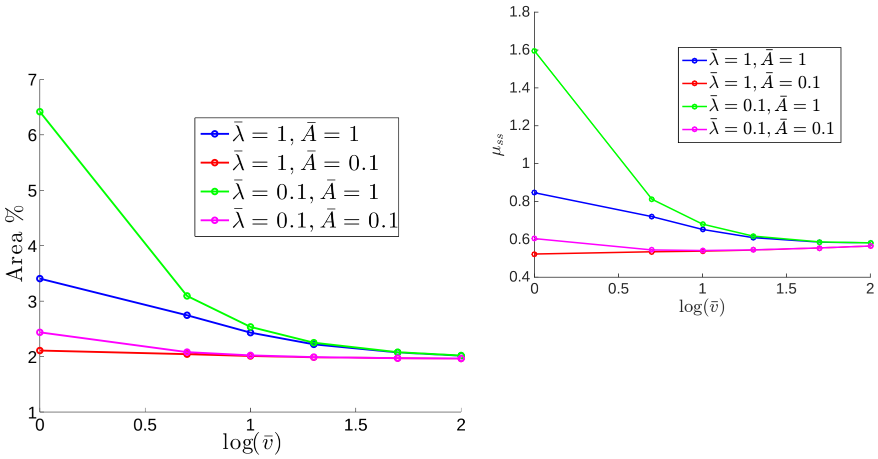

(a) (b)

Figure 3.18: Steady state (a) contact area and (b) friction coefficient at different sliding speeds for four combinations of the viscoelastic parameters. The contact area always decreases with increasing speed but the friction coefficient might increase or decrease depending on whether the direct effect or the transient effect dominates.

3.5.4 Magnitude of the direct effect

According to the local friction law (equation 3.10), the magnitude of the direct effect at any sliding speed is proportional to the area of contact at steady state at that speed, $A_r(\bar{v})$. Since $A_r(\bar{v})$ decreases monotonically with increasing $\bar{v}$, the magnitude of the direct effect also decreases monotonically. In experiments though, it is observed that the direct effect is proportional to the logarithm of the ratio of the final and initial sliding speeds. This is possible, at least in our formulation, only if the velocity dependent term in equation (3.10) increases faster than $\log(\bar{v})$.

3.5.5 Normal stress jump and pulse tests

Experiments show that when sliding surfaces are subjected to jumps in the normal pressure, they show a history-dependent behavior, similar to what is seen in velocity jump tests [38, 85]. To test this in our simulations, a pressure of 50 MPa is applied and the system is slid till it reaches steady state. Then, the pressure is “instantaneously” increased to 75MPa. The sliding is then continued. During the fast loading, the contact area also changes instantaneously and this is followed by an evolution to a steady state corresponding to the new load (Figures 3.19a). This behavior has been observed in experiments, as shown in Figure 3.19b [38] (in our model, the shear force is proportional to the contact area).

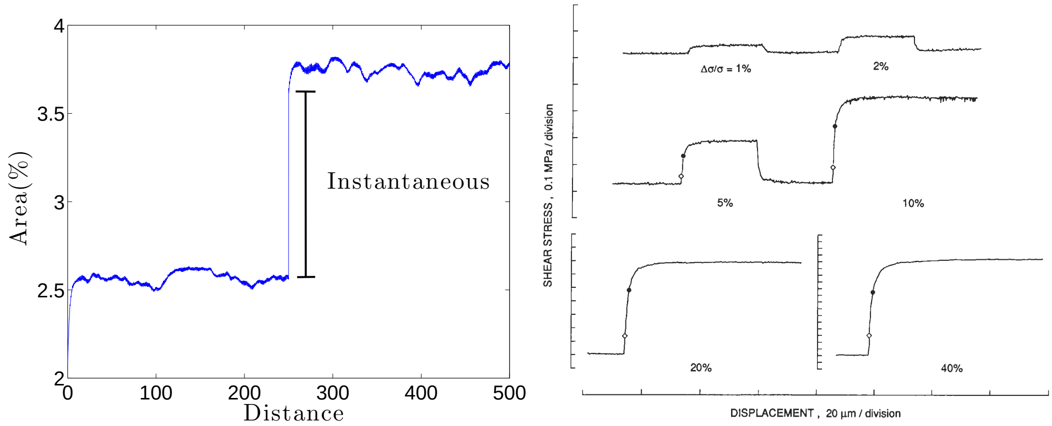

(a) (b)

Figure 3.19: Evolution of (a) contact area in our simulation and (b) shear stress in experiments during a normal stress jump test (reproduced with permission from [38]). The contact area changes instantaneously during the normal stress increase and this is followed by an evolution to a new steady state.

Similarly, we perform normal stress pulse simulations. The normal stress is increased and brought back to the initial value instantaneously. In experiments, it is seen that the shear stress does not go back to the initial value instantaneously but evolves over a longer time scale (Figure 3.20c) [38, 85]. In our simulations, if the loading and unloading during the normal stress variation is done at a very high rate compared to the viscoelastic relaxation time, the area goes back to its initial value along with the applied normal stress. This is to be expected since the loading unloading process is effectively elastic (see Figure 3.20a). If the loading unloading is done at a slower rate, the area does not go back to its initial value along with the normal force but evolves over a longer timescale, as in experiments (Figure 3.20b).

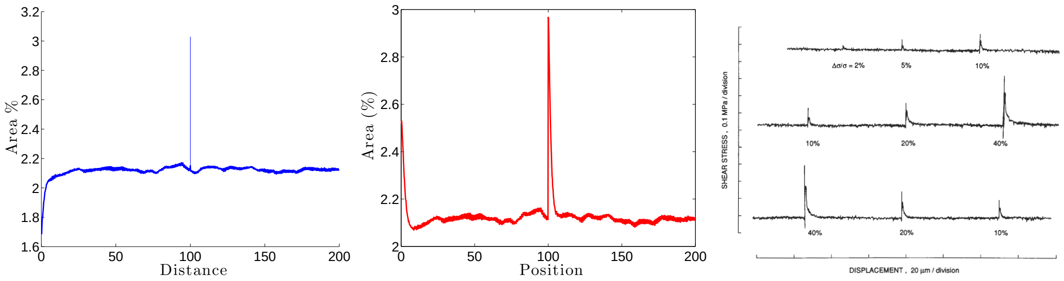

(a) (b) (c)

Figure 3.20: Evolution of contact area in our simulations when the normal stress pulse is applied at a (a) very high rate, and (b) a rate comparable to the viscoelastic timescale. (c) Evolution of shear stress in experiments during a normal stress pulse test (reproduced with permission from [38]).

3.5.6 Dependence of characteristic slip on roughness and viscoelasticity

In experiments, the characteristic slip D_c over which friction reaches steady state following a velocity jump has been observed to be nearly independent of the sliding speed, the normal force etc., but to depend on the surface roughness. In all experiments in the literature, in preparing the surfaces, there is no independent control of the surface parameters σ (rms roughness) and β (the correlation length). Thus, they cannot distinguish between the effects of the two separately. Intuitively, we expect D_c to depend more on the correlation length than the rms roughness of the surface. To test this, velocity jump simulations are performed for three combinations of σ, β (all results are averaged over 15 realizations of the rough surface).

D_c is calculated by fitting an exponential to the transient μ_k evolution following a velocity jump. In our simulations, D_c depends on the correlation length much more strongly than the rms roughness (Figure 3.21). The correlations in the surface features of the rough surface decay over the length scale β. Thus, the distance the system has to slide to reach steady state depends on β and D_c increases with increasing β. The rms roughness σ affects the area of contact, and the value of the friction coefficient but does not affect D_c.

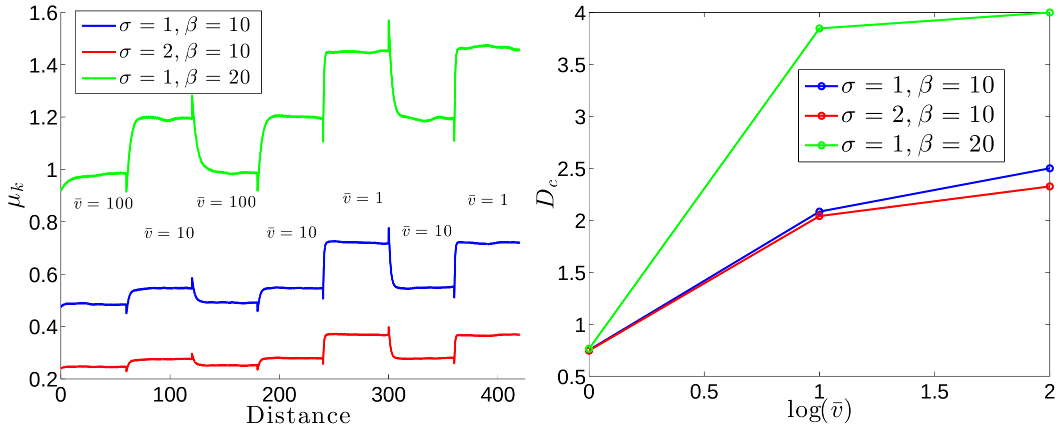

(a) (b)

Figure 3.21: (a) Evolution of friction coefficient in velocity jump simulations for surfaces of three different roughness. (b) Decay length at different speeds for the three cases. The decay length depends more strongly on the correlation length than the rms roughness.

To see if D_c if affected by the elastic interactions, the above calculations are repeated with no elastic interactions. Surprisingly, D_c is largely unchanged by the presence of elastic interactions (Figure 3.22).

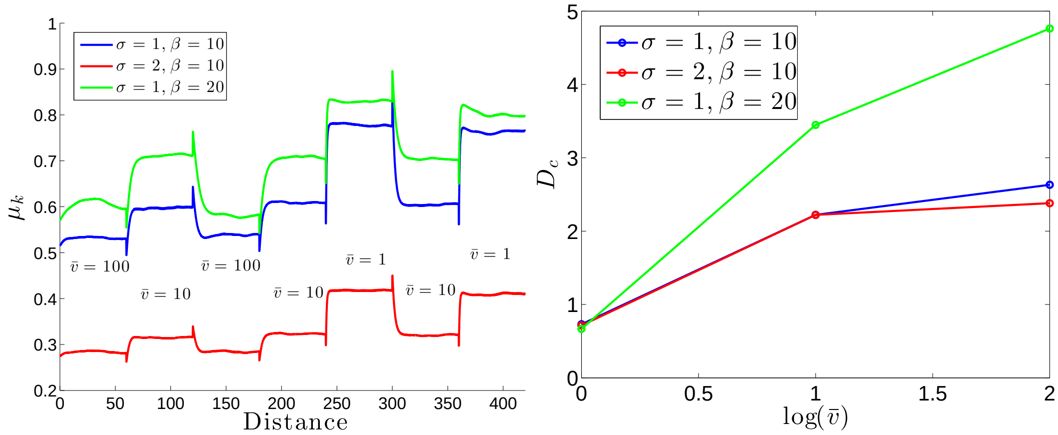

(a) (b)

Figure 3.22: Decay length at different speeds with no elastic interactions. Comparison with Figure 3.21 shows that elastic interactions do not affect D_c significantly.

In Figures 3.21 and 3.22, at very low speeds, D_c is independent of the surface properties. This is because, at very low speeds, the sliding process is almost elastic, since the viscoelastic elements have a lot of time to relax before sliding any considerable distance. With longer viscoelastic relaxation timescales (smaller $\bar{\lambda}$), D_c should be higher at the lower sliding speeds. To test this, velocity jump simulations on surfaces with three different viscoelastic properties are performed. We find that adding the longer timescales does increase D_c at the lower sliding speeds (Figure 3.23b). The experimentally observed constancy of D_c over a range of sliding speeds could thus be a result of the fact that a real material usually has a broad range of relaxation times.

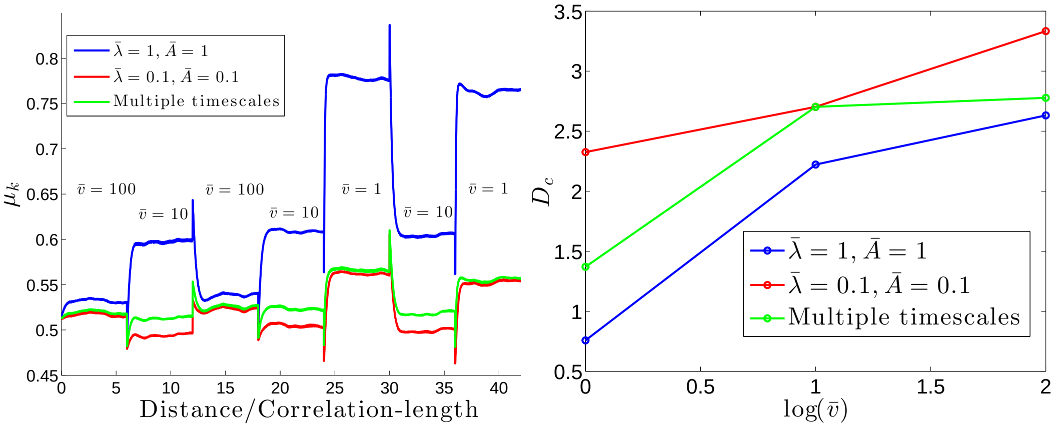

(a) (b)

Figure 3.23: (a) Evolution of friction coefficient in velocity jump simulations for surfaces of three different viscoelastic properties. The green curve corresponds to a system with four timescales, $\bar{\lambda}_k = 1, 0.1, 0.01, 0.001, \bar{A} = 0.25, 0.025, 0.0025, 0.00025$. Including longer relaxation timescales increases D_c at the lower sliding speeds.

3.5.7 Convergence with increasing spatial frequency

Because the rough surface is discretized, roughness features only up to a finite maximum spatial frequency can be incorporated. Since rough surfaces have features at many length scales, it is interesting to see if there is a convergence in the macroscopic properties as more and more frequencies are included. For this, we perform static contact and velocity jump simulations for surfaces with different cut-off frequencies in spatial features.

Simulations show that the area of contact decreases as more and more frequencies are included (Figure 3.24). This is because lower cut-off frequencies make the surfaces smoother (see Section 3.4.4 on roughness dependence). Furthermore, the marginal change in area with respect to the cut-off frequency decreases with increasing frequency. Thus, it can be expected that surface features beyond a certain frequency will have little effect on the macroscopic contact area.

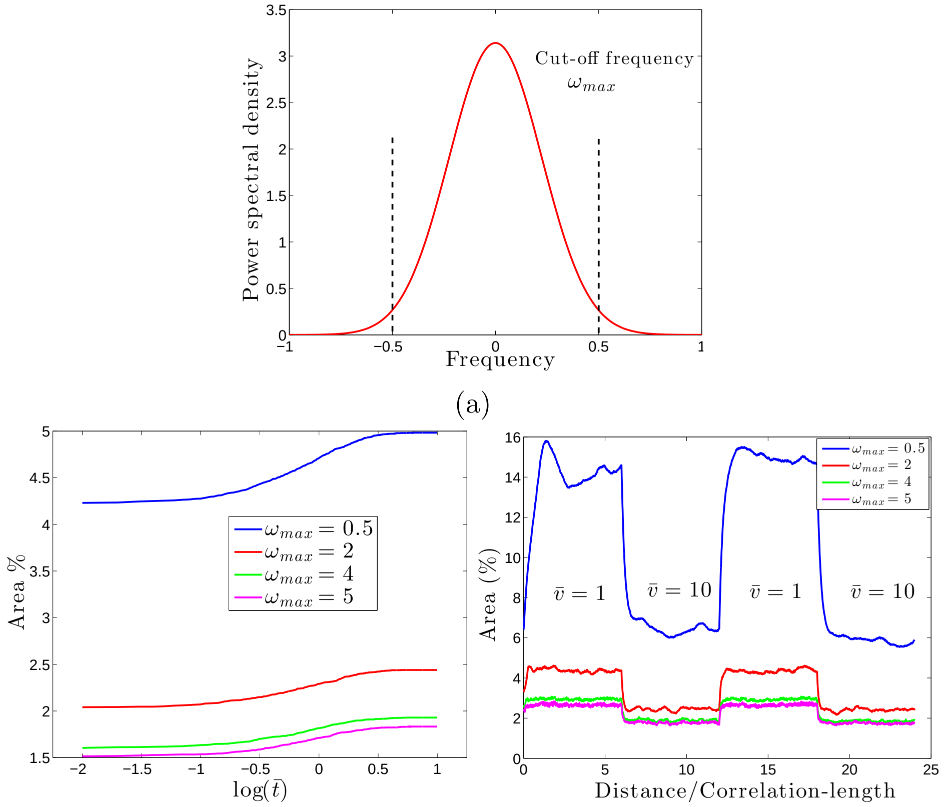

(a)

(b) (c)

Figure 3.24: (a) Power spectrum of Gaussian noise with Gaussian correlation. Area of contact area during (b) static contact and (c) velocity jump simulations for surfaces with different cut-off frequencies. The area of contact decreases as we include more and more frequencies, since lower cut-off frequencies make the surfaces smoother. The marginal change in area with respect to the cut-off frequency decreases with increasing frequency.

3.6 Conclusion

Here, we developed a framework to study the time and velocity dependent behavior of rough surfaces in static and sliding contact to understand how static and sliding friction are affected by material properties (particularly, viscoelastic properties), surfaces roughness, and long-range elastic interactions.

We found that although elastic interactions are important from a quantitative perspective, they do not change the qualitative aspects of frictional behavior, either in static or sliding contact.

In static contact, the duration of growth of friction coefficient is determined by the viscoelastic relaxation times. The absolute value of the friction coefficient and the magnitude of growth during static contact are determined by both the viscoelastic properties and the surface roughness.

The sliding behavior is determined by the interaction of two timescales, the viscoelastic relaxation times, and the ratio of the correlation length of the surface to the sliding speed. The distributions of forces at the contacts at different speeds are different, and this determines how the contact area and friction coefficient change with the sliding speed. Depending on the direct effect and the contact area dependence on sliding speed, the behavior can be velocity-strengthening or velocity-weakening. The characteristic slip distance D_c depends on the viscoelastic relaxation times, the sliding speed, and the correlation length of the surface, but not on the rms roughness.

Chapter 4

Static and sliding contact of viscoplastic rough surfaces

The model in the previous chapter assumes that the material behavior of the deformable surface is linear viscoelastic. While this is reasonable for some materials like polymers, in others, like rocks, ceramics, and metals, the time-dependent behavior is due to the high local stresses at the contacts. This creep behavior, and its causal mechanisms such as dislocation motion, has been extensively studied and characterized by viscoplastic models [86]. Thus, incorporating these viscoplastic models provides a further link between macroscopic behavior and the underlying mechanisms.

4.1 Elastic-viscoplastic model

We propose the following elastic-viscoplastic constitutive model. First, the total deformation is split into elastic and plastic parts:

$$\bar{u} = \bar{u}_e + \bar{u}_p, \quad \dot{\bar{u}} = \dot{\bar{u}}_e + \dot{\bar{u}}_p,$$

where $\bar{u}, \bar{u}_e$, and $\bar{u}_p$ are the total, elastic, and plastic deformations, respectively. The forces and the elastic deformations are related linearly:

$$\bar{u}_e = \bar{C}_{ij}\bar{F}_j,$$

where $\bar{C}_{ij}$ is the compliance and $\bar{F}_i$ is the force. A power law creep prescribes the evolution of plastic strain:

$$\dot{\bar{u}}_p = A_{cr}(|\bar{F}|/\bar{F}_y)^n \operatorname{sign}(\bar{F}), \tag{4.1}$$

where $\bar{F}_y, A_{cr}, n$, are the yield stress, the creep rate, and the creep exponent, respectively. A hardening rule is defined the evolution of the yield stress:

$$\dot{\bar{u}}_{acc} = |\dot{\bar{u}}_p|, \bar{F}_y = \bar{F}_y^0(1 + B\bar{u}_{acc})^m,$$

where $\bar{u}_{acc}, \bar{F}_y^0, B, m$ are the accumulated plastic strain, the initial yield stress, the hardening rate and the hardening exponent respectively.

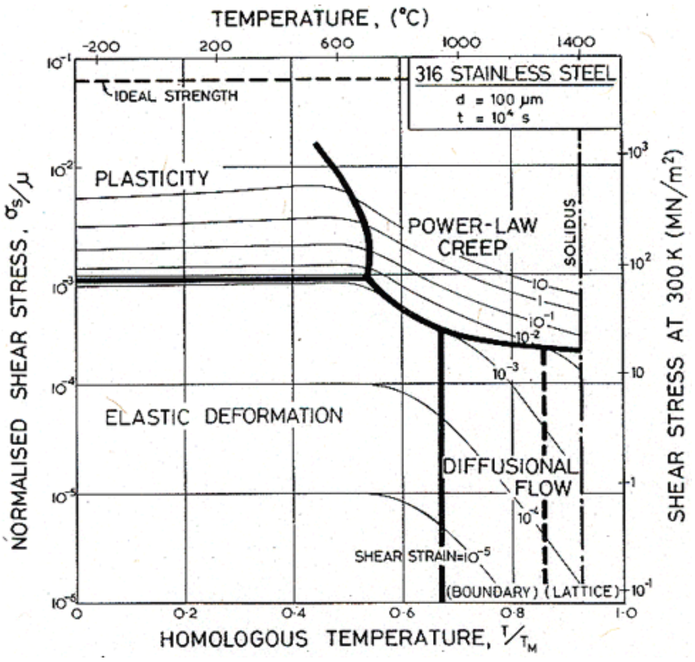

Figure 4.1: Deformation mechanism map for stainless steel (reproduced with permission from [86]). Such maps can be used to determine the relevant viscoplastic creep law.

Although specific forms of creep and hardening laws are used here, depending on the material, the stresses, and temperature, appropriate laws can be used by referring to deformation mechanism maps such as those of Frost and Ashby [86]. Figure 4.1

shows one such map for stainless steel [86].

4.2 Static Contact

We simulate the static contact test of rough surfaces. These are similar to the simulations described in Section 3.4 in Chapter 3 with the viscoelastic constitutive equation replaced by the above described viscoplastic model.

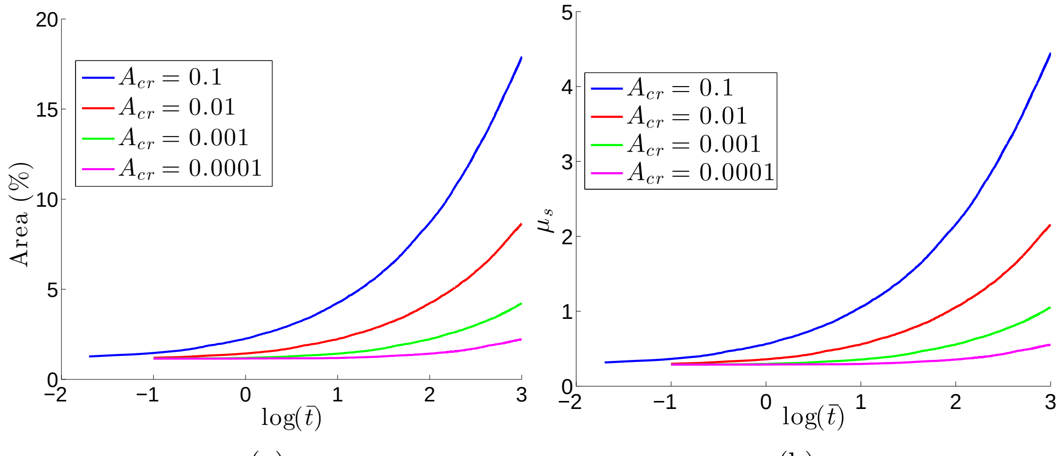

(a) (b)

Figure 4.2: Evolution of contact area and static friction coefficient with time for a viscoplastic material. μ_s grows logarithmically with time with no signs of saturation, as seen in many experiments.

As in the viscoelastic case, the area of contact, and thus μ_s, increases with the time of contact, and after an initial phase, grows logarithmically with time (Figure 4.2). In the viscoelastic case, the growth saturates after about 2 decades (Section 3.4 in Chapter 3). However, here the growth seems to continue indefinitely and shows no signs of saturation. This is expected from the viscoplastic model since the contacts continue to creep under any nonzero force (see equation 4.1).

Figure 4.2 also shows the dependence of the friction evolution on the creep rate A_{cr}. Larger creep rates lead to a faster and larger growth in μ_s. Similar parametric studies of the other viscoplastic parameters can be used to determine the range of physically relevant viscoplastic parameters. For example, it is known that the real area of contact in most cases is of the order of 1%. This implies that the relevant creep rates are around 0.001 (assuming the other parameters used are in the right regime).

4.3 Sliding contact

We also perform velocity jump simulations similar to those described in Section 3.5 of Chapter 3. The qualitative features of friction evolution are the same as the viscoelastic case. With a jump in the sliding speed, there is an instantaneous change in μ_k followed by a transient evolution to a steady state (Figure 4.3). The figure also shows how μ_k depends on the creep rate A_{cr}. Large creep rates lead to large transients and velocity-weakening, whereas smaller creep rates result in velocity-strengthening behavior.

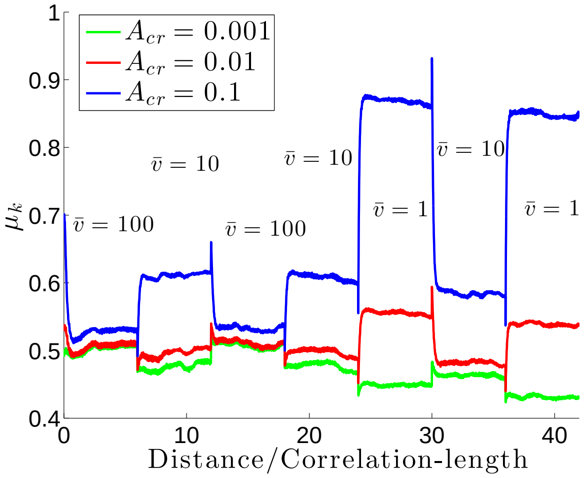

Figure 4.3: Evolution of μ_k during velocity jump tests. Large creep rates lead to velocity-weakening while smaller creep rates result in velocity-strengthening behavior.

One key difference between the viscoelastic and viscoplastic formulations is that in the viscoplastic case there is permanent deformation. So, the surfaces evolve as they are in static or sliding contact. Figure 4.4 shows two surfaces, an initially undeformed one and the same surface after sliding for a while. Two peaks in the surface are marked with circles, and, as is evident from the figure, the peaks get flattened as the surface slides. A profile of a section through the surface and the plastic deformation after the sliding are also shown. It would be interesting to study if the plastic deformation leaves a signature of the sliding direction.

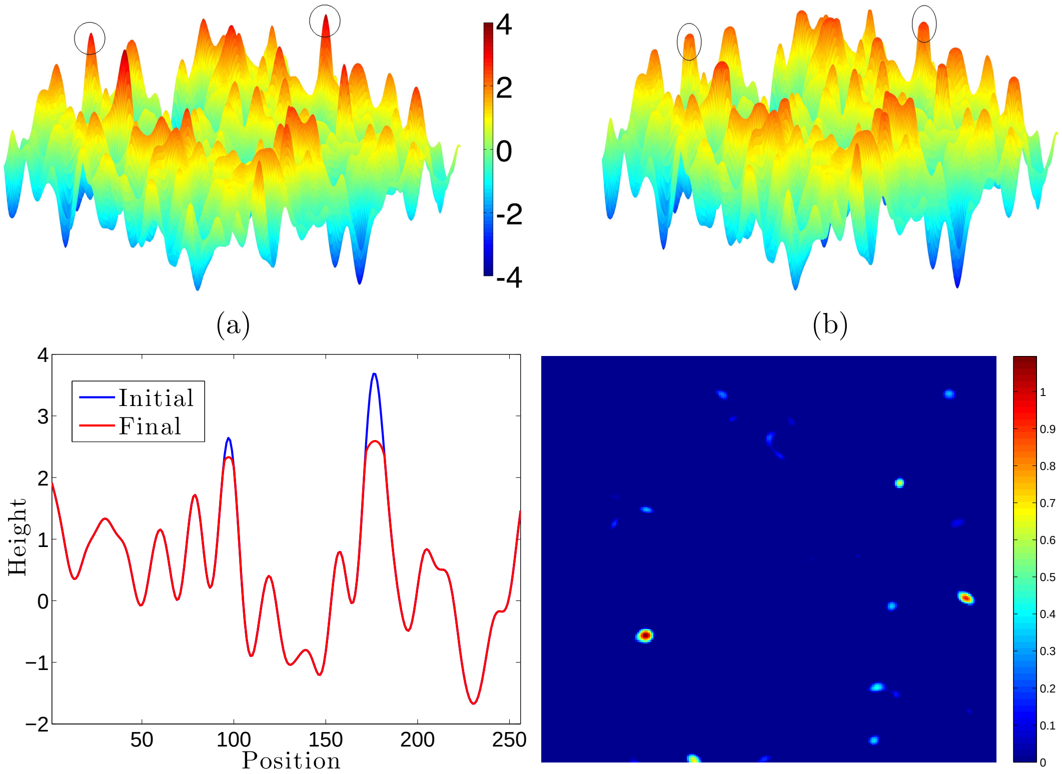

(a) (b)

(c) (d)

Figure 4.4: Evolution of the surface during sliding: (a) initially undeformed and (b) final deformed surfaces. The blunting of the peaks due to permanent deformation is evident (black circles). (c) A profile showing a section across the surface and (d) plastic deformation at the contacts.

4.4 Dependence on temperature

During sliding, the energy dissipated at the contacts can lead to a large increase in the temperature locally at the interface [30] and this can change the material properties. If the sliding speed is slow enough compared to the heat diffusion timescale, the temperature at the surface might reach a steady state that depends on the sliding speed. The dependence of the viscoplastic parameters on temperature has been well studied [86]. For example, the creep rate is observed to depend exponentially on the inverse temperature, $A_{cr} \propto e^{-Q/kT}$, where Q is an activation energy, k is the Boltzmann constant, and T is the temperature. Let us consider two temperatures,

T_{high} and T_{low}. For simplicity, we assume that $A_{cr} = 0.001$ at T_{low} and $A_{cr} = 0.1$ at T_{high}, n is the same at the two temperatures and there is no hardening. Such large changes in creep rates are not unreasonable. For example, in Figure 4.1, in the power-law creep regime, the strain rate changes from 0.01 to 1 over a temperature change of about 300K. Such changes in temperature have been measured in experiments [30].

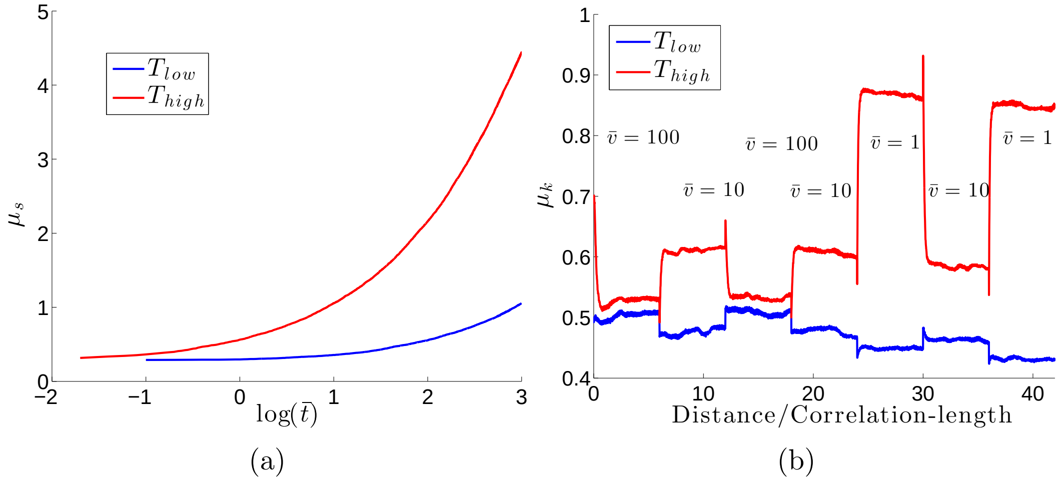

(a) (b)

Figure 4.5: Evolution of friction coefficient at two different temperatures: (a) static contact test and (b) velocity jump test.

The slope of the friction growth, $\beta = d\mu_s/d\log(\bar{t})$ (calculated in the part where the growth is logarithmic), is higher at the higher temperature (Figure 4.5a). $\beta = 0.59$ at T_{low} and 2.50 at T_{high}. A similar dependence on temperature is observed in some experiments [48].

In velocity jump tests, the system transitions from velocity-strengthening at the lower temperature and velocity-weakening at the higher temperature (Figure 4.5b). Such a dependence on temperature is seen in experiments [87, 8]. In some materials, the transition is ascribed to the onset of ductility [8], which matches with our model in that higher creep rates A_{cr} can be interpreted as the material being more ductile.

4.5 Concluding remarks

The results of the viscoelastic and viscoplastic formulations suggest that the qualitative features of evolution of friction are robust to the assumptions of the underlying time-dependent behavior. It seems that as long as the time-dependent behavior of individual contacts is rate-strengthening (higher forces when deformed at faster rates; this is true for both the viscoelastic and viscoplastic cases), we see the growth of static friction with time and the inverse relationship between the contact area and the sliding speed (which leads to the characteristic evolution in velocity jump tests). This hints that the reason many materials show similar macroscopic frictional behavior is the minimal restriction it places on the microscopic behavior.

Chapter 5

Inclusion of adhesive interactions

Adhesion plays an important role in many cases. In MEMS, hard disk drives and other such devices, stiction is a great problem [88, 89, 90]. Adhesion in biological systems like the gecko is a source of both fascination and inspiration [91, 92, 93].

Effects of adhesion are apparent in fluids; for example, the shape of a liquid drop, the contact (wetting) angle, hydrophobicity, and hydrophilicity are all dictated by the minimization of surface energy. In solids, apart from the surface energy, the elastic energy also plays a role and the two together determine the response [94].

Consider a solid of volume V and surface area A. If the typical strain is ϵ, then the elastic and surface energies are given by:

$$E_e = \frac{1}{2} K \epsilon^2 V, \quad E_s = \gamma A,$$

where E_e, E_s are the elastic and surface energies, K is the stiffness of the material, and γ is the surface energy per unit area. Consider the ratio of the two energies,

$$\frac{E_s}{E_e} = \frac{\gamma}{0.5 K \epsilon^2} \frac{A}{V}.$$

If γ/K is small, for surface energy to be important, the ratio of A/V should be large, and this happens at small length scales. For example, for many metals, this length scale is about 1-10 nm [95] and this is the reason that the the effects of surface energy are not important at macroscopic length scales in these materials. For soft materials, γ/K is large and effects of surface energy are important in such cases.

5.1 Previous studies

The problem of elastic contact of non-adhesive parabolic surfaces was solved by Hertz [96]. Around the 1970s, Roberts, Kendall, and others, in their experiments with rubber and glass spheres, observed that the contact area at low loads was larger than the predictions of Hertzian theory. Further, the contact area remained finite as the load was reduced to zero. Johnson et al. developed a model in which the contact area is determined by minimizing the total energy of the system, which has contributions from the elastic energy, the surface energy, and the potential energy [97]. The model, which has since been known as the JKR model, has been used widely. Around the same time, Derjaguin and others developed another model for adhesive contact (known as the DMT model) [98]. In the JKR model, the adhesive forces act only within the region of contact, whereas in the DMT model the attractive adhesive forces are active outisde the contact zone. Although the applicability of the two models was hotly debated, the connection between the two was pointed out by Tabor [99] and Maugis [100], and it was realized that the JKR model is appropriate for soft solids with large surface energy while the DMT model is appropriate for hard solids with small surface energy.

Roughness affects the adhesion between surfaces to a large extent and since most surfaces are rough, rough surface adhesion has been explored extensively. Fuller and Tabor experimentally studied the adhesion of smooth rubber spheres and flat rough rough perspex substrates [101]. They showed that even a roughness of the order of 1 μm reduces the adhesion strength (pull-off force) substantially. They also developed a model by substituting the Hertzian contacts in the Greenwood-Williamson model [102] by a JKR contact and found reasonable agreement with their experiments. Briggs and Briscoe, in reproducing the experiments of Fuller and Tabor, found that adhesion does not vary monotonically with roughness [103]. At small roughness, they found an increase in adhesion with increasing roughness. This non-monotonic variation of adhesion with roughness has been observed in many experiments since [104, 82, 105, 106, 107].

On the theoretical side, apart from the models of Fuller and Tabor, Persson and Tosatti proposed another model for the adhesive contact of fractal rough surfaces [108, 109]. For a given nominal area, increasing roughness increases the real area thus increasing adhesion. But increasing roughness also increases the elastic energy required to deform the asperities. In a certain range of parameters, the result of the combined effects of the above two effects is that adhesion increases with increasing roughness. Their model, however, is reversible in that all the elastic energy stored is employed in the peeling of contacts. The elastic adhesive contact problem with a single wavelength roughness was studied by Guduru [110] and Kesari et al. [111]. They showed that the presence of roughness can increase the adhesive pull-off force.

The relation between adhesion and friction has also been studied greatly. McFarlane and Tabor, in their experiments with indium and steel surfaces, showed that at low loads, the friction coefficient can be high [112]. Since friction is a dissipative process, it must be related not to adhesion itself but to the hysteresis in adhesion. A correlation between adhesion hysteresis and friction has been observed in some experiments [113, 114].

Here, the models of the previous chapters are extended to include adhesion. In the next section, we start with a single degree of freedom system. Depending on the surface energy, the system reproduces JKR and DMT like behaviors.

5.2 A single degree-of-freedom (DOF) system

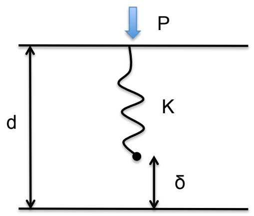

Figure 5.1: A single degree of freedom system. The total energy of the system is a sum of the elastic energy, which depends on the extension in the spring $d - \delta$, and the surface energy, which depends on δ.

Consider the single degree of freedom system shown in Figure 5.1. A linear spring of stiffness K hangs from a rigid surface, which is at a distance d from another rigid surface. The separation between the spring and the second rigid surface is δ. Without loss of generality, the undeformed length of the spring can be set to zero; the deformation in the spring is then $d-\delta$. We assume that there is a surface energy between the two surfaces that decays exponentially with δ. The total energy for the system is:

$$E = \frac{1}{2}K(d-\delta)^2 - \gamma e^{-\delta/\lambda},$$

where γ is the surface energy and λ is the length scale of the surface energy decay. Nondimensionalizing the above, we get:

$$\bar{E} = \frac{1}{2}(\bar{d}-\bar{\delta})^2 - \bar{\gamma} e^{-\bar{\delta}}, \tag{5.1}$$

where the lengths are nondimensionalized by λ, energy by $K\lambda^2$, and

$$\bar{\gamma} = \gamma / K\lambda^2$$

is the nondimensionalized surface energy. The rigidity of the second surface implies $\bar{\delta} \geq 0$.

For given dilatation $\bar{d}$, the equilibrium separation minimizes the total energy:

$$\bar{\delta}_{eq} = \min_{\bar{\delta}} \bar{E}(\bar{\delta}), \quad \bar{\delta} \geq 0, \tag{5.2}$$

where $\bar{\delta}_{eq}$ is the equilibrium separation. If $\bar{\delta} > 0$, no constraint force acts and the energy minimizer is the solution to

$$\frac{\partial \bar{E}}{\partial \bar{\delta}} = 0 \quad \text{or} \quad \bar{d} - \bar{\delta} = \bar{\gamma} e^{-\bar{\delta}}. \tag{5.3}$$

The stability criterion for the minimizer is that the second derivative is positive:

$$\frac{\partial^2 \bar{E}}{\partial \bar{\delta}^2} = 1 - \bar{\gamma} e^{-\bar{\delta}} > 0. \tag{5.4}$$

If $\bar{\gamma} < 1, 1 - \bar{\gamma} e^{-\bar{\delta}} > 0$, since $\bar{\delta} \geq 0$ and all energy minimizers all stable. If $\bar{\gamma} > 1$, the second derivative can become zero for positive $\bar{\delta}$. This corresponds to loss of stability. In the next two sections, we study the behavior of the system for $\bar{\gamma} < 1$ and $\bar{\gamma} > 1$, respectively.

5.2.1 Nondimensional surface energy $\bar{\gamma} < 1$

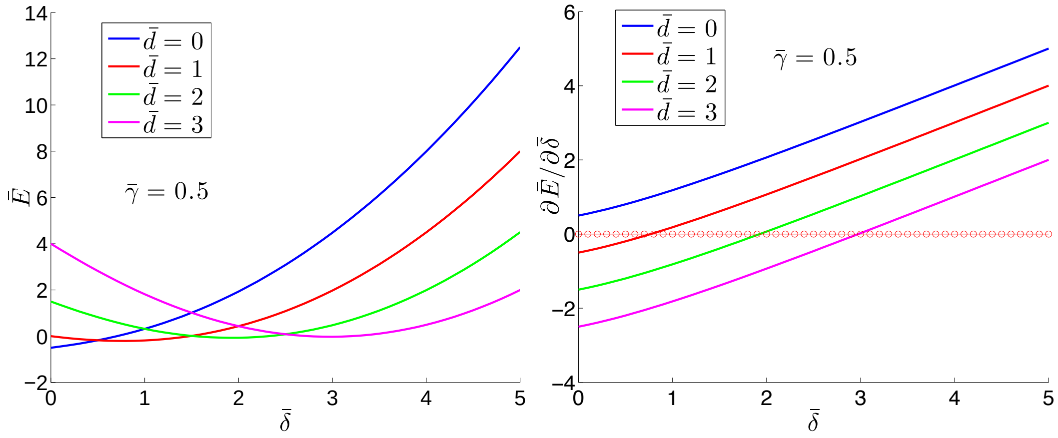

(a) Energy (b) First derivative

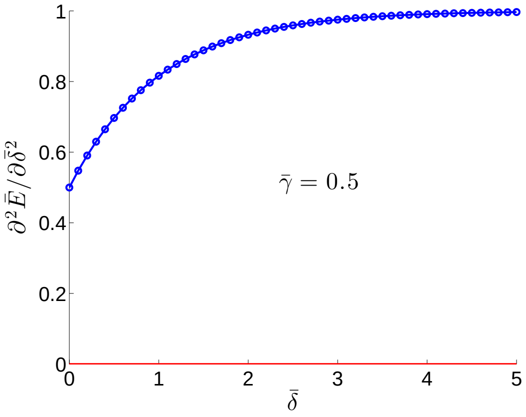

(c) Second derivative

Figure 5.2: (a) energy, (b) energy gradient, and (c) the second derivative as a function of the separation $\bar{\delta}$ for different dilatation $\bar{d}$ for $\bar{\gamma} < 1$. There is a unique minimizer for each $\bar{d}$ and it is stable.

When $\bar{\gamma} < 1$, for each dilatation $\bar{d}$, there is a unique energy minimum which corresponds either to the solution of $\partial \bar{E}/\partial \bar{\delta} = 0$ or the constraint $\bar{\delta} = 0$ (see Figure 5.2a). This can also be seen from Figure 5.2b where the energy gradient has a unique zero, or is positive everywhere in which case the minimizer is $\bar{\delta} = 0$. This minimum is stable since the second derivative is always postive (Figure 5.2c).

Consider a loading-unloading test performed by first decreasing the dilatation $\bar{d}$ and then increasing it. The equilibrium separation for each dilatation can be calculated using equation 5.2. The energy minimizer during loading and unloading curves are the same, and there is no hysteresis in the system (Figure 5.3). The response of the system when $\bar{\gamma} < 1$ is thus similar to the DMT model.

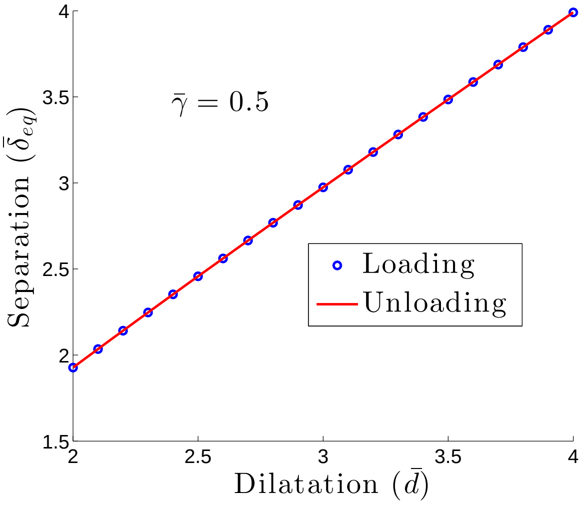

Figure 5.3: Equilibrium separation as a function of the dilatation. The loading and unloading curves are on top of each other, there is no hysteresis in the system.

5.2.2 Nondimensional surface energy $\bar{\gamma} > 1$

Now consider the more interesting case, $\bar{\gamma} > 1$. Figure 5.4 shows the energy, with its first and second derivatives as a function of the separation $\bar{\delta}$ for different values of $\bar{d}$. Let us consider a loading-unloading process. For a large dilatation (such as $\bar{d} = 3$ in the figure), there is a unique energy minimizer corresponding to $\partial \bar{E}/\partial \bar{\delta} = 0$ and it is stable (second derivative is positive). On decreasing $\bar{d}$, at some critical dilatation, this minimizer becomes unstable (second derivative becomes zero) and the first derivative of the energy is positive everywhere. Here, the minimum of the energy is at $\bar{\delta} = 0$. This critical state can be determined by setting the second derivative of energy to zero.

$$\frac{\partial^2 \bar{E}}{\partial \bar{\delta}^2} = 0 \implies \bar{\delta}_{\text{snap-in}} = \log(\bar{\gamma}), \quad \bar{d}_{\text{snap-in}} = 1 + \log(\bar{\gamma}). \tag{5.5}$$

This $\bar{\delta}_{\text{snap-in}}$ is finite and positive and increases with $\bar{\gamma}$. This means that the spring snaps into contact with the rigid surface when it is at a finite separation and the contact formation is not a gradual process as it is when $\bar{\gamma} < 1$. On further decrease of $\bar{d}$, the minimizer stays at $\bar{\delta} = 0$ and is stable.

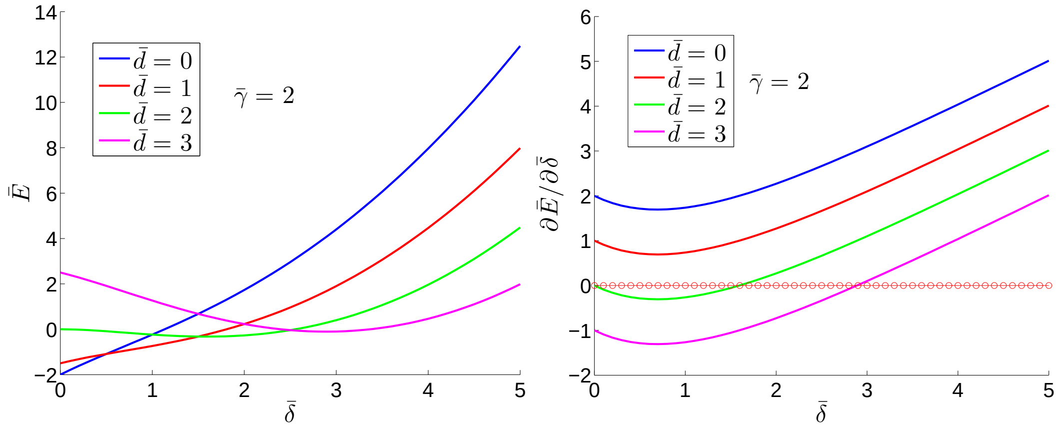

(a) Energy (b) First derivative

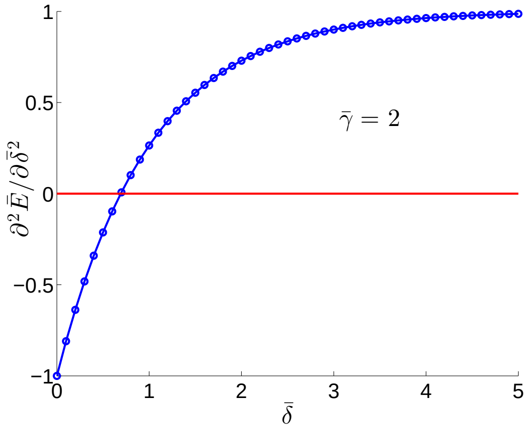

(c) Second derivative

Figure 5.4: (a) energy, (b) energy gradient, and (c) the second derivative as a function of separation $\bar{\delta}$ for different dilatations $\bar{d}$ for $\bar{\gamma} > 1$. The energy is non-convex and the system exhibits hysteresis, snapping into and out of contact at critical states.

Now, on unloading (increasing $\bar{d}$), the spring initially stays at $\bar{\delta} = 0$. With further increase of $\bar{d}$, a new minimum appears at a nonzero $\bar{\delta}$, but the system is stuck at the local minimum $\bar{\delta} = 0$ because there is an energy barrier to switch to the other minimum ($\partial \bar{E}/\partial \bar{\delta}|_{\bar{\delta}=0} > 0$). When $\partial \bar{E}/\partial \bar{\delta}|_{\bar{\delta}=0}$ becomes zero for the first time, the spring snaps out of contact and switches to the other energy minimizer. This snap-off point can be determined as:

$$\frac{\partial \bar{E}}{\partial \bar{\delta}}\left(\bar{\delta} = 0\right) = 0 \implies \bar{d}_{\text{snap-off}} = \bar{\gamma}. \tag{5.6}$$

Interestingly, this snap-off point is different from the snap-in point. For $\bar{\gamma} > 1$,

$$\bar{\gamma} > 1 + \log(\bar{\gamma}),$$

and thus, the snap-off dilatation is always larger than the snap-in dilatation.

Because of the snap-in and snap-off behavior, the equilibrium separation during loading and unloading are different and there is hysteresis in the system. This is clearly seen in Figure 5.5 which shows the equilibrium separation as a function of the dilatation. Outside of the snap-in/snap-off region, there is a unique minimizer and the loading-unloading process is reversible.

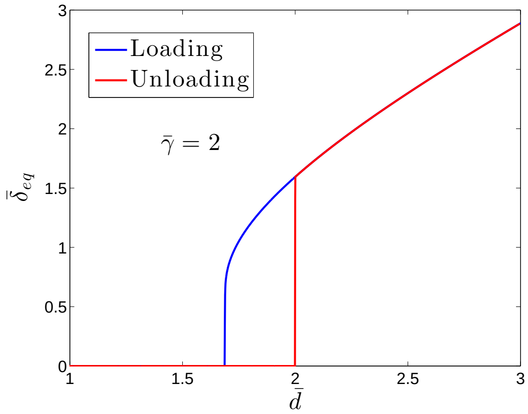

(a) Loading/Unloading

Figure 5.5: Equilibrium separation as a function of the dilatation during a loading-unloading cycle. The snap-in during loading and snap-off during unloading happen at different points and there is hysteresis in the system. Outside of this region, the system is reversible.

The evolution of force (which is equal to $\bar{d}-\bar{\delta}$, the deformation of the spring) also shows a similar hysteretic behavior (Figure 5.6). The force is tensile at large dilatation and increases on decreasing the dilatation, since the adhesive force becomes stronger. After snap-in, on further loading, the force starts becoming compressive (in Figure 5.6, we have not loaded the system enough for this to happen) because of the constraint force from the rigid surface. During unloading, the force becomes tensile again and reaches a maximum at the snap-off point.

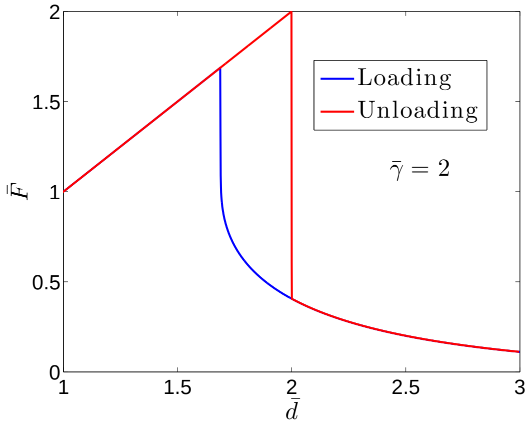

Figure 5.6: Evolution of force during the loading-unloading cycle. The adhesive tensile force is maximum at the snap-off point.

Energy dissipation The snapping into and out of contact are irreversible dissipative processes. Since the dilatation and separation before and after snap-in and snap-off are known, the elastic and surface energies, and thus the energy dissipated, can be calculated. These are given by:

$$\Delta\bar{E}_{\text{snap-in}} = \bar{\gamma} - \frac{1}{2} - \frac{1}{2}\left(1+\log(\bar{\gamma})\right)^2 \tag{5.7}$$

$$\Delta\bar{E}_{\text{snap-off}} = \bar{\delta}_{\text{snap-off}}\left(\bar{\gamma} - 1 - \bar{\delta}_{\text{snap-off}}\right), \tag{5.8}$$

where $\bar{\delta}_{\text{snap-off}}$ is the solution to,

$$\bar{\gamma} - \bar{\delta}_{\text{snap-off}} = \bar{\gamma}e^{-\bar{\delta}_{\text{snap-off}}}.$$

It is interesting to see if this dissipated energy is significant. If $\bar{\gamma}$ is big enough, the energy dissipated can be a significant fraction of or even larger than $\bar{\gamma}$, the reversible work of separation (Figure 5.7). For example, when $\bar{\gamma} = 5$, the total energy dissipated during a loading-unloading cycle is around $1.8\bar{\gamma}$.

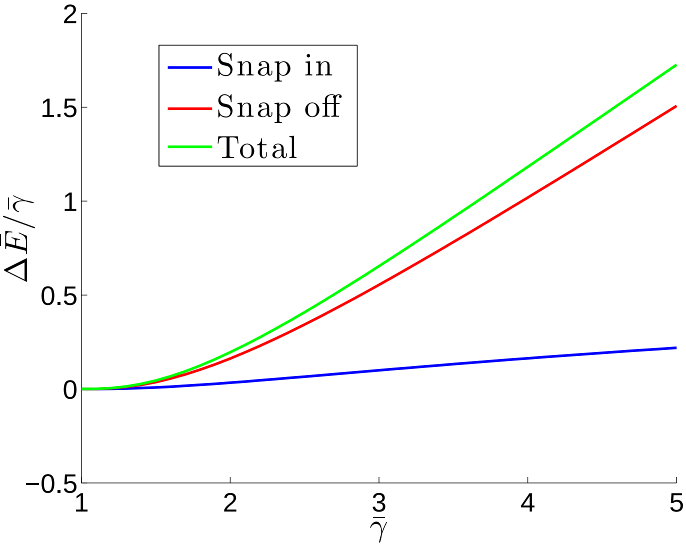

Figure 5.7: Energy dissipated during snap-in, snap-off, and their sum as a function of $\bar{\gamma}$. If $\bar{\gamma} \gg 1$, this dissipated energy can be significant compared to the reversible work of adhesion $\bar{\gamma}$.

Thus, when $\bar{\gamma} > 1$, the behavior of the system is JKR like. In the next section, we extend the above one degree of freedom system to an ensemble of non-interacting elements.

5.3 Ensemble of independent adhesive elements

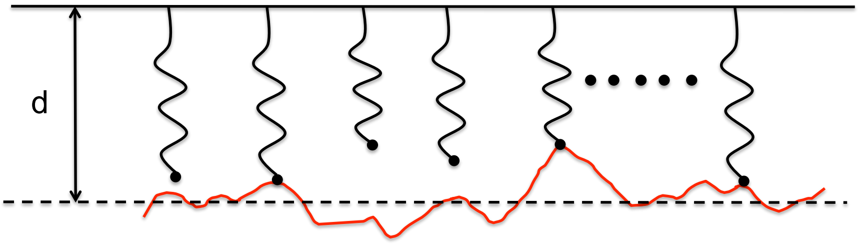

Figure 5.8: An ensemble of springs against a rough rigid surface. The response of each element is as in the previous section and there is no interaction between the elements.

Consider an ensemble of springs hanging from a flat rigid surface and sitting above a rough rigid surface. The rough surface has a probability distribution of heights $P(\bar{h})$. The distance between the flat surface and the mean height of the rough surface is $\bar{d}$. For each spring, if the height of the rough surface against it is $\bar{h}$, the energy is given by:

$$\bar{E} = \frac{1}{2}(\bar{d} - \bar{h} - \bar{\delta})^2 - \bar{\gamma} e^{-\bar{\delta}}, \tag{5.9}$$

where $\bar{\delta}$ is still the separation between the spring and the surface. From the energy, it follows that all of the analysis of the previous section carries through if $\bar{d}$ of the previous section is replaced by $\bar{d} - \bar{h}$. The force in the spring is now given by:

$$\bar{F}(\bar{h}) = \bar{d} - \bar{h} - \bar{\delta}.$$

We restrict our attention to the case $\bar{\gamma} > 1$. Thus, if the height of the rigid surface is $\bar{h}$, the snap-in and snap-off dilatation are given by:

$$\bar{d}_{\text{snap-in}} = 1 + \bar{h} + \log(\bar{\gamma}), \quad \bar{d}_{\text{snap-off}} = \bar{h} + \bar{\gamma}.$$

5.3.1 Loading

During loading, if the dilatation is $\bar{d}$, all springs with $\bar{\delta} \leq 1+\log(\bar{\gamma})$ snap into contact. Defining

$$\bar{h}_{\text{snap-in}} = \bar{d} - (1 + \log(\bar{\gamma})),$$

all springs where $\bar{h} \geq \bar{h}_{\text{snap-in}}$ are in contact at dilatation $\bar{d}$. The total force of the ensemble, $\bar{F}_N$, is given by:

$$\begin{aligned} \bar{F}_N(\bar{d}) &= \int_{-\infty}^{\infty} \bar{F}(\bar{h}) P(\bar{h}) \mathrm{d}\bar{h} \\ &= \int_{-\infty}^{\infty} (\bar{d} - \bar{h} - \bar{\delta}) P(\bar{h}) \mathrm{d}\bar{h} \\ &= \bar{d} - < \bar{h} > - \int_{-\infty}^{\infty} \bar{\delta} P(\bar{h}) \mathrm{d}\bar{h}. \end{aligned} \tag{5.10}$$

Without loss of generality $< \bar{h} >$ can be set to zero, since this is the same as using the level of mean heights as the reference level. If $\bar{h} \geq \bar{h}_{\text{snap-in}}$, the springs snap into contact and $\bar{\delta} = 0$. Otherwise, $\bar{\delta}$ is given by the solution to:

$$\bar{d} - \bar{h} - \bar{\delta} = \bar{\gamma} e^{-\bar{\delta}}.$$

Thus,

$$\bar{F}_N(\bar{d}) = \bar{d} - \int_{-\infty}^{\bar{h}_{\text{snap-in}}} \bar{\delta}(\bar{h}) P(\bar{h}) \mathrm{d}\bar{h}.$$

5.3.2 Unloading

Suppose we load up to a minimimum dilatation $\bar{d}_{\text{min}}$ and then start increasing the dilatation. All springs where the height of the rigid surface is greater than or equal to $\bar{h}_{\text{min}} = \bar{d}_{\text{min}} - (1 + \log(\bar{\gamma}))$ have snapped into contact. On unloading, some of these snap out of contact. So, for given $\bar{d}$ during unloading, we define $\bar{h}_{\text{snap-off}}$ as the height of the rough surface above which the springs are in contact and below which the springs have either snapped out of contact or never came into contact. It can be seen that:

$$\bar{h}_{\text{snap-off}} = \max(\bar{h}_{\min}, \bar{d} - \bar{\gamma}).$$

So, during unloading, the force is given by,

$$\begin{aligned}
\bar{F}_N(\bar{d}) &= \int_{-\infty}^{\infty} \bar{F}(\bar{h}) P(\bar{h}) \mathrm{d}\bar{h} \\
&= \int_{-\infty}^{\infty} (\bar{d} - \bar{h} - \bar{\delta}) P(\bar{h}) \mathrm{d}\bar{h} \qquad (5.11) \\
&= \bar{d} - \int_{-\infty}^{\max(\bar{h}_{\min}, \bar{d} - \bar{\gamma})} \bar{\delta} P(\bar{h}) \mathrm{d}\bar{h}.
\end{aligned}$$

5.3.3 Energy dissipation

In one loading-unloading cycle, if the minimum dilatation is $\bar{d}_{\min}$, all the springs where $\bar{h} \geq \bar{h}_{\min}$ snap into and out of contact. Thus, the total energy dissipated in one cycle is given by:

$$\Delta\bar{E}(\bar{d}_{\min}) = (\Delta\bar{E}_{\text{snap-in}} + \Delta\bar{E}_{\text{snap-off}}) \int_{\bar{h}_{\min}}^{\infty} P(\bar{h}) \mathrm{d}\bar{h}, \qquad (5.12)$$

where $\Delta\bar{E}_{\text{snap-in}}$ and $\Delta\bar{E}_{\text{snap-off}}$ are given by equation 5.7.

5.3.4 Force evolution

From here, the heights of the rigid surface has are assumed to have a Gaussian probability distribution with an rms roughness σ. Thus,

$$P(\bar{h}) = \frac{1}{\sqrt{2\pi}\sigma} e^{-\bar{h}^2/2\sigma^2}.$$

Consider a loading-unloading cycle of an ensemble of springs. The hysteresis in the individual springs manifests as a hysteresis is the global response (Figure 5.9). At a large dilatation, the force is initially tensile and on further loading, the springs snap into contact and are subsequently compressed. The total force reaches a tensile peak and then becomes compressive. After reaching a minimum dilatation, the system is unloaded and the springs remain in contact until their snap-off point is reached and thus, during unloading, the force is greater (more positive) than during loading. With further increase in dilatation, the force reaches a peak tensile value and then decays to zero. The tensile peak during unloading is greater than the peak achieved during loading. We define the peak tensile force during unloading as the adhesive strength ($\bar{F}_{\max}$) of the surface. We now study the dependence of the adhesive strength on $\bar{d}_{\min}, \bar{\gamma},$ and σ.

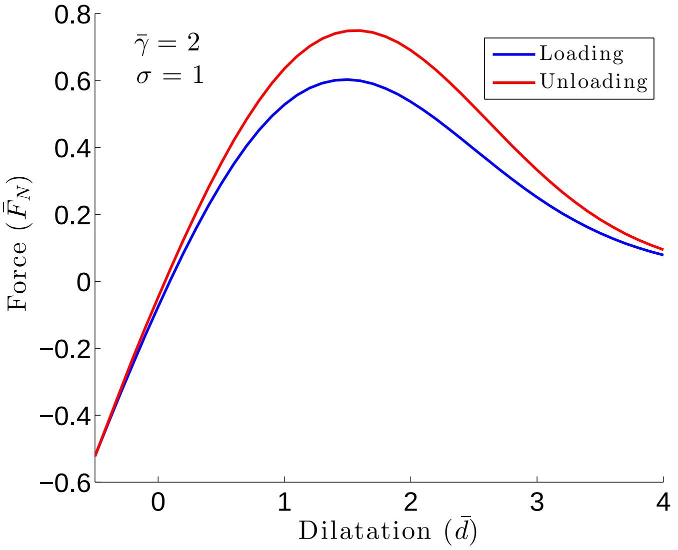

Figure 5.9: A typical loading-unloading process for the ensemble. The hysteresis of each element leads to the hysteresis in the ensemble response.

5.3.5 Depth-dependence of adhesive strength

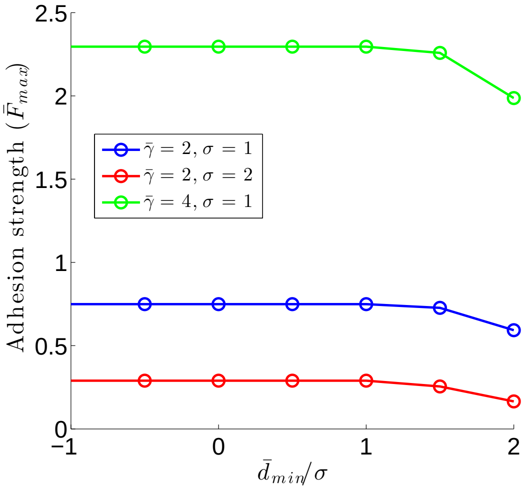

Figure 5.10: Dependence of the adhesion strength on (a) $\bar{d}_{\min}$, the minimum dilatation achieved during the loading phase. For $\bar{d}_{\min}/\sigma < 1$, the adhesive strength remains nearly constant.

The adhesive strength depends on $\bar{d}_{\min}$, the minimum dilatation achieved during the loading phase. With decreasing $\bar{d}_{\min}$, a larger fraction of the elements snap-into contact and contribute to adhesion, and thus the adhesive strength increases (Figure 5.10). For $\bar{d}_{\min}/\sigma < 1$, the adhesive strength remains nearly constant since the new springs that snap into contact when compressed beyond $\bar{d}_{\min}/\sigma = 1$ snap out of contact before the force peaks and thus do not contribute to the adhesive strength.

5.3.6 Dependence of adhesive strength on roughness

Experiments show that over a large range of roughness, the adhesion strength decreases with increasing surface roughness, but for a relatively short range it increases with increasing roughness [104, 82, 105, 106, 107]. In our model, $\bar{F}_{\max}$ decreases monotonically with increasing σ (Figure 5.11) which agrees with variation seen in experiments for a large range of roughness.

Our model does not include two potentially important factors, the spatial structure of roughness and elastic interactions between contacts. Our conjecture is that one or both of these is necessary for the non-monotonicity of adhesion strength.

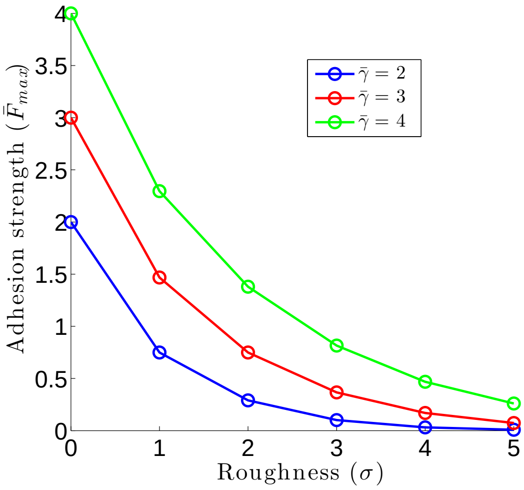

Figure 5.11: Dependence of $\bar{F}_{\mathrm{max}}$ on σ. The adhesion strength decreases monotonically with increasing roughness.

5.3.7 Depth-dependent energy dissipation

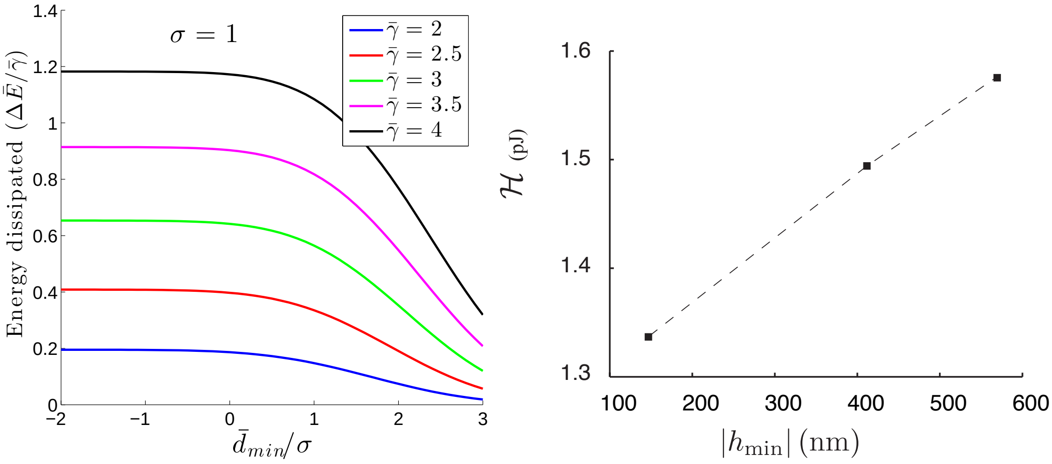

(a) (b)

Figure 5.12: Depth dependence of hysteresis during a loading-unloading cycle: (a) In our simulations, hysteresis increases with decreasing indentation depth and saturates to a constant value at about $\bar{d}_{\mathrm{min}}/\sigma = 0$. (b) In experiments of Kesari et al., hysteresis increases with the indentation depth (reproduced with permission from [107]). Note: Decreasing $\bar{d}_{\mathrm{min}}$ in (a) corresponds to increasing $|h_{\mathrm{min}}|$ in (b).

Kesari et al. [107] studied how the energy dissipated in a loading-unloading cycle depends on the minimum dilatation achieved during loading (Figure 5.12b). Figure 5.12a shows the energy dissipated during a loading-unloading cycle as a function of

$\bar{d}_{\min}$ in our model. When $\bar{d}_{\min}/\sigma$ is betwen 0 and 3, the energy dissipated variation is similar to what is observed in the experiments (Note: In Figure 5.12, decreasing $\bar{d}_{\min}$ in (a) corresponds to increasing $|h_{\min}|$ in (b)). For $\bar{d}_{\min}/\sigma < 0$, the energy dissipated is nearly constant since the probability density of heights is small in this region (note that when $\bar{d}_{\min} = 0$, all springs where $\bar{h} \geq -(1 + \log(\bar{\gamma}))$ have already snapped into contact).

5.3.8 Dependence of energy dissipation on surface roughness and surface energy

For a single element, the energy dissipated can be significant compared to the reversible surface energy (Section 5.2.2). The presence of roughness can reduce the dissipation considerably. Surprisingly, even for a rough surface, if $\bar{\gamma} \gg 1$, the dissipation can be a considerable fraction of, and even larger than, the reversible work of adhesion $\bar{\gamma}$ (Figure 5.13). For a given $\bar{d}_{\min}/\sigma$, the energy dissipated decreases with increasing roughness, and this decrease is stronger for larger $\bar{d}_{\min}/\sigma$.

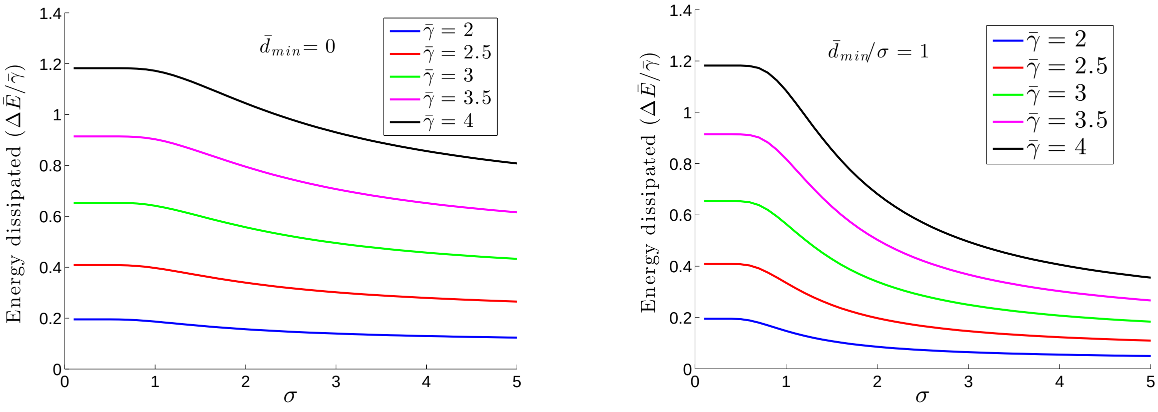

(a) (b)

Figure 5.13: Energy dissipated during a loading-unloading cycle as a function of σ for different $\bar{\gamma}$: (a) $\bar{d}_{\min} = 0$ and (b) $\bar{d}_{\min}/\sigma = 1$.

In this section, the linear elastic spring were non-interacting. In the next section, we extend the formulation to the contact of three dimensional rough surfaces, and incorporate long-range elastic interactions and inelastic (viscoelastic and viscoplastic) effects.

5.4 Extension to three dimensions

5.4.1 Formulation

The model here is an extension of the formulation presented in Section 3.2 in Chapter 3. First, the deformation is split into elastic and inelastic parts:

$$u_i(t) = u_i^e(t) + u_i^{in}(t). \tag{5.13}$$

For the elastic part, we have the following constitutive relation:

$$u_i^e(t) = C_{ij}^E F_j(t), \tag{5.14}$$

where C_{ij}^E is the elastic compliance matrix. Based on the material, an evolution law is prescribed for the inelastic deformation. For example, in the case of linear viscoelasticity,

$$u_i^{in}(t) = \int_0^t \left(\sum_j C(t-\tau, r_{ij}) F_j(\tau) \right) \mathrm{d}\tau, \tag{5.15}$$

where $C(t-\tau, r_{ij})$ is a viscoelastic kernel. For viscoplasticity, an incremental relation can be prescribed for the inelastic deformation. To include adhesion, we prescribe a constitutive relation corresponding to the surface forces. If the dilatation is d, the separation between an element and the rigid surface is given by $d - x_j^0 - y_j(t) - u_j(t)$, where x^0, y, and u are the undeformed length, the height of the rigid surface, and the total deformation, respectively. Following from the earlier sections, the adhesive surface energy E^s and force F^s are then given by:

$$E_j^s(t) = \gamma e^{-(d-x_j^0-y_j(t)-u_j(t))/\lambda}, \quad F_j^s(t) = \frac{\gamma}{\lambda} e^{-(d-x_j^0-y_j(t)-u_j(t))/\lambda}.$$

For elements in contact, the rigid surface applies a constraint force F^{const}. Including this, for each element:

$$\begin{aligned} F_j(t) &= F_j^s(t) + F_j^{const}(t) \\ &= \frac{\gamma}{\lambda} e^{-(d-x_j^0-y_j(t)-u_j(t))/\lambda} + F_j^{const}(t). \end{aligned} \tag{5.16}$$

Using this in equation (5.14),

$$\begin{aligned} u_i^e(t) &= C_{ij}^E \left[\frac{\gamma}{\lambda} e^{-(d-x_j^0-y_j(t)-u_j(t))/\lambda} + F_j^{const} \right] \\ &= C_{ij}^E \left[\frac{\gamma}{\lambda} e^{-(d-x_j^0-y_j(t)-u_j^e(t)-u_j^{in}(t))/\lambda} + F_j^{const} \right]. \end{aligned} \tag{5.17}$$

Differentiating the equation with respect to time,

$$\dot{u}_i^e(t) = C_{ij}^E \left[-\frac{\gamma}{\lambda^2} e^{-(d-x_j^0-y_j(t)-u_j(t))/\lambda} (\dot{d} - \dot{x}_j^0 - \dot{y}_j(t) - \dot{u}_j(t)) + \dot{F}_j^{const}(t) \right].$$

The above equation can be written as,

$$[K]\{\dot{u}^e\} = \{b\} + [C^E]\{\dot{F}^{const}\}, \tag{5.18}$$

where,

$$\{b\} = -\frac{\gamma}{\lambda^2} C_{ij}^E e^{-(d-x_j^0-y_j(t)-u_j(t))/\lambda} (\dot{d} - \dot{y}_j - \dot{u}_j^{in}), \tag{5.19}$$

and,

$$[K] = \delta_{ij} - \frac{\gamma}{\lambda^2} C_{ij}^E e^{-(d-x_j^0-y_j(t)-u_j(t))/\lambda} \text{ (no ‘j’ summation).}$$

Equation 5.18 is the governing set of ODEs for the system. Given the dilatation history $d(t)$, equation 5.18 determines the evolution of forces and deformations of the elements.

5.4.2 Numerical implementation

We use a first order explit Euler method to integrate the governing equations. The contact constraint has to be treated carefully. The governing equations are split into two parts corresponding to elements in and out-of contact. For the elements out of contact, the constraint force is zero. For elements in contact, the total deformation is determined from the kinematic constraint,

$$x_i^0 + u_i(t) + y_i(t) = d(t).$$

Using (1) to represent elements in contact and (2) for ones not in contact, equation 5.18 can be written as,

$$\begin{bmatrix} K_{11} & K_{12} \\ K_{21} & K_{22} \end{bmatrix} \begin{bmatrix} \dot{u}_1^e \\ \dot{u}_2^e \end{bmatrix} = \begin{bmatrix} C_{11}^E & C_{12}^E \\ C_{21}^E & C_{22}^E \end{bmatrix} \begin{bmatrix} \dot{F}_1^{const} \\ \dot{F}_2^{const} \end{bmatrix} + \begin{bmatrix} b_1 \\ b_2 \end{bmatrix}. \tag{5.20}$$

Assuming that elements in/out-of contact remain that way during a small time step,

$$\dot{u}_1^e = \dot{d} - \dot{y}_1 - \dot{u}_1^{in}, \quad \dot{F}_2^{const} = 0.$$

Now, $\dot{u}_2^e$ and $\dot{F}_1^{const}$ must be determined. Rearranging the linear system,

$$\begin{aligned} \begin{bmatrix} K_{11} & K_{12} \\ K_{21} & K_{22} \end{bmatrix} \begin{bmatrix} 0 \\ \dot{u}_2^e \end{bmatrix} - \begin{bmatrix} C_{11}^E & C_{12}^E \\ C_{21}^E & C_{22}^E \end{bmatrix} \begin{bmatrix} \dot{F}_1^{const} \\ 0 \end{bmatrix} = \begin{bmatrix} b_1 \\ b_2 \end{bmatrix} &- \begin{bmatrix} K_{11} & K_{12} \\ K_{21} & K_{22} \end{bmatrix} \begin{bmatrix} \dot{u}_1^e \\ 0 \end{bmatrix} \\ &+ \begin{bmatrix} C_{11}^E & C_{12}^E \\ C_{21}^E & C_{22}^E \end{bmatrix} \begin{bmatrix} 0 \\ \dot{F}_2^{const} \end{bmatrix}. \end{aligned}$$

Using $\dot{F}_2^{const} = 0$,

$$\begin{bmatrix} K_{11} & K_{12} \\ K_{21} & K_{22} \end{bmatrix} \begin{bmatrix} 0 \\ \dot{u}_2^e \end{bmatrix} - \begin{bmatrix} C_{11}^E & C_{12}^E \\ C_{21}^E & C_{22}^E \end{bmatrix} \begin{bmatrix} \dot{F}_1^{const} \\ 0 \end{bmatrix} = \begin{bmatrix} b_1 \\ b_2 \end{bmatrix} - \begin{bmatrix} K_{11} & K_{12} \\ K_{21} & K_{22} \end{bmatrix} \begin{bmatrix} \dot{u}_1^e \\ 0 \end{bmatrix}.$$

The left hand side can be written as a single matrix acting on a single vector,

$$\begin{bmatrix} K_{11} & K_{12} \\ K_{21} & K_{22} \end{bmatrix} \begin{bmatrix} 0 \\ \dot{u}_2^e \end{bmatrix} - \begin{bmatrix} C_{11}^E & C_{12}^E \\ C_{21}^E & C_{22}^E \end{bmatrix} \begin{bmatrix} \dot{F}_1^{const} \\ 0 \end{bmatrix} = \left(\begin{bmatrix} 0 & 0 \\ 0 & I \end{bmatrix} - [C^E] \begin{bmatrix} I & 0 \\ 0 & K^{surf} \end{bmatrix} \right) \begin{bmatrix} \dot{F}_1^{const} \\ \dot{u}_2^e \end{bmatrix}$$

where,

$$K_{ii}^{surf} = \frac{\gamma}{\lambda^2} e^{-(d - x_i^0 - y_i - u_i)/\lambda}$$

and

$$K_{ij}^{surf} = 0, \text{ if } i \neq j.$$

Defining the matrix K^{eff} as,

$$K^{eff} = \begin{bmatrix} 0 & 0 \\ 0 & I \end{bmatrix} - [C^E] \begin{bmatrix} I & 0 \\ 0 & K^{surf} \end{bmatrix},$$

the linear system that is solved to determine the unknown force and deformation rates is,

$$[K^{eff}] \begin{bmatrix} \dot{F}_1^{const} \\ \dot{u}_2^e \end{bmatrix} = \{b\} - \begin{bmatrix} K_{11} & K_{12} \\ K_{21} & K_{22} \end{bmatrix} \begin{bmatrix} \dot{u}_1^e \\ 0 \end{bmatrix}. \tag{5.21}$$

If γ/λ^2 is large enough, the matrix K^{eff} can become singular and this corresponds to the elements snapping into contact. We do not know how to estimate how large γ/λ^2 has to be for this. Here, only cases where this does not happen are considered.

Given the current state of the system, the dilatation d, the forces F_i, elastic and inelastic deformations u_i^e, u_i^{in}, and the constraint forces F_i^{const}, the steps involved a one time increment are:

1. Assume the elements in and out of contact remain that way during a small time step Δt. Given $\dot{d}$, the deformation rate for the elements in contact is,

$$\dot{u}_1 = \dot{d} - \dot{y}_1.$$

2. Compute the inelastic deformation rate $\dot{u}^{in}$ of all the elements (for example,

using a prescribed viscoelastic or viscoplastic equation).

3. Compute the elastic deformation rate for the elements in contact,

$$\dot{u}_1^e = \dot{u}_1 - \dot{u}_1^{in}.$$

4. Compute the right hand side of equation 5.21.

5. Solve the linear system for $\dot{F}_1^{const}, \dot{u}_2^e$.

6. Update all the forces and deformations and contact conditions. For the transitions from out-of-contact to in-contact, the kinematic condition can be used. For transitions from in-contact to out-of-contact, the fact that the constraint force cannot be positive (the rigid surface only pushes on the elements) is used.

5.4.3 Nondimensionalization

The equations are nondimensionalized in exactly the same way as Section 3.2.1 in Chapter 3. The nondimensionalized adhesion parameters are defined as:

$$\bar{\lambda} = \frac{\lambda}{L^*}, \quad \bar{\gamma} = \frac{\gamma}{2\pi G L^{*3}/(1-\nu)}.$$

5.4.4 Indentation of an elastic spherical surface

To study the effect of adhesion, we start with the indentation of a linear elastic sphere of radius 20. The adhesion parameters used are $\bar{\gamma} = 10^{-5}$ and $\bar{\lambda} = 0.1$. The surfaces are initially sufficiently separated for the adhesive interactions to be negligible and the forces and deformations of all the elements are initialized to zero. The surfaces are then brought into contact by decreasing the dilatation. As the dilatation is decreased, the adhesive interactions become stronger and the tensile force increases (Figure 5.14a). On further loading, some of the elements come into contact with the rigid surface and are compressed. The total force reaches a tensile peak and then becomes compressive. Since the adhesion forces are small enough not to cause any snap-in/snap-off instabilities, on unloading the force evolution retraces the loading path.

Figure 5.14b shows the force distribution across the contact at the minimum dilatation state. The forces are compressive at the center of the contact, but towards the edge and outside the contact the forces are tensile. This can be seen as a cohesive zone of an external crack. The strength and the decay rate of this cohesize zone are determined by $\bar{\gamma}$ and $\bar{\lambda}$. The JKR and DMT models can be seen as different limits of the cohesize zone (at least qualitatively). The JKR model is the limit of large $\bar{\gamma}$ and small $\bar{\lambda}$, whereas the DMT model is the limit of small $\bar{\gamma}$ and large $\bar{\lambda}$.

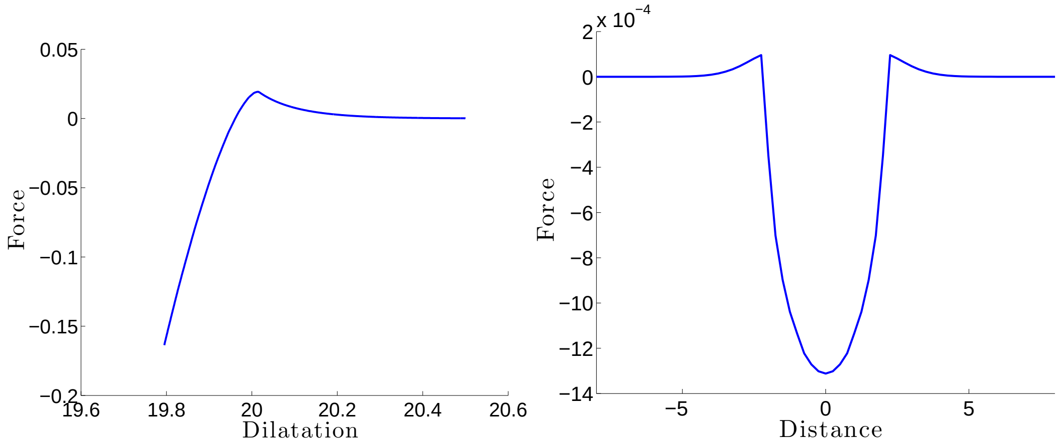

(a)

(b)

Figure 5.14: Indentation of an elastic sphere with adhesion: (a) force evolution with dilatation and (b) force distribution across the contact.

5.4.5 Effect of adhesion on rough surface friction

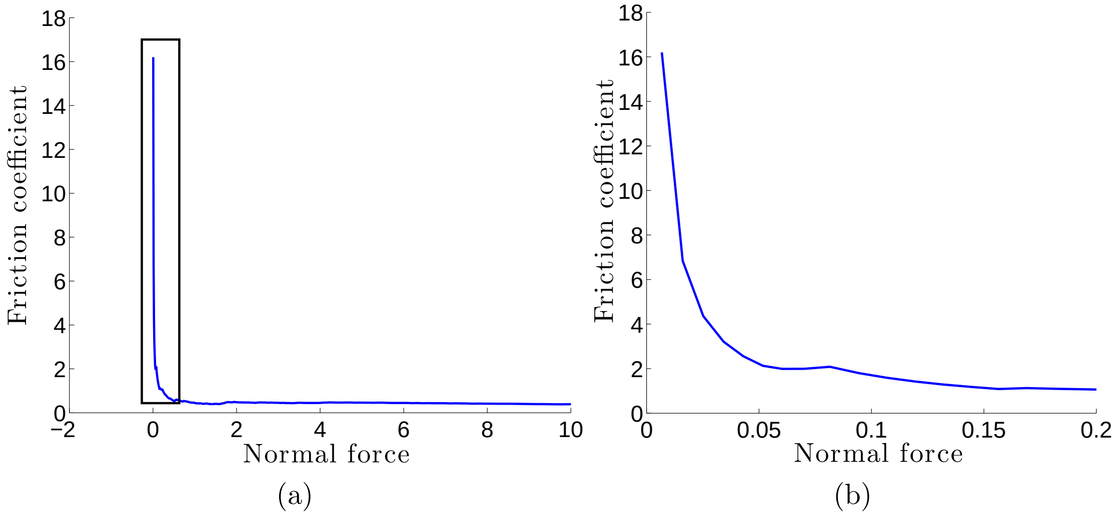

(a) (b)

Figure 5.15: Indentation test of a rough surface with adhesion: (a) Dependence of friction coefficient on the normal force. (b) Inset marked in (a).

In MEMS, NEMS and such systems, the interacting surfaces are not subjected to large loads. In such situations, the effect of adhesion can be significant. We perform an indentation test of two rough surfaces 256 × 256 in size ($\sigma = 1$), with adhesion parameters $\bar{\gamma} = 5 \times 10^{-4}, \bar{\lambda} = 0.1$ and Boussinesq elastic interactions. At small normal forces, effects of adhesion are important: the friction coefficient is high and shows marked normal force dependence (Figure 5.15). At large loads, the friction coefficient becomes nearly independent of the normal load.

A similar dependence of friction on the normal force was observed by McFarlane and Tabor in their experiments with steel and indium surfaces [112], although they explained the dependence based on work hardening of the material (indium is a soft solid, so effects of surface energy can be important).

5.4.6 Viscoelastic adhesive contact

Many materials where adhesion is important are also viscoelastic (polymers for example). To study the interaction between viscoelasticity and adhesion, we perform static contact simulations (see Section 3.4 of Chapter 3) of a viscoelastic material with a single relaxation timescale. In equation (5.15),

$$C(t-\tau, r_{ij}) = \frac{1-\nu}{2\pi G}\frac{1}{r_{ij}} \quad e^{-(t-\tau)}r_{ij} > 0.$$

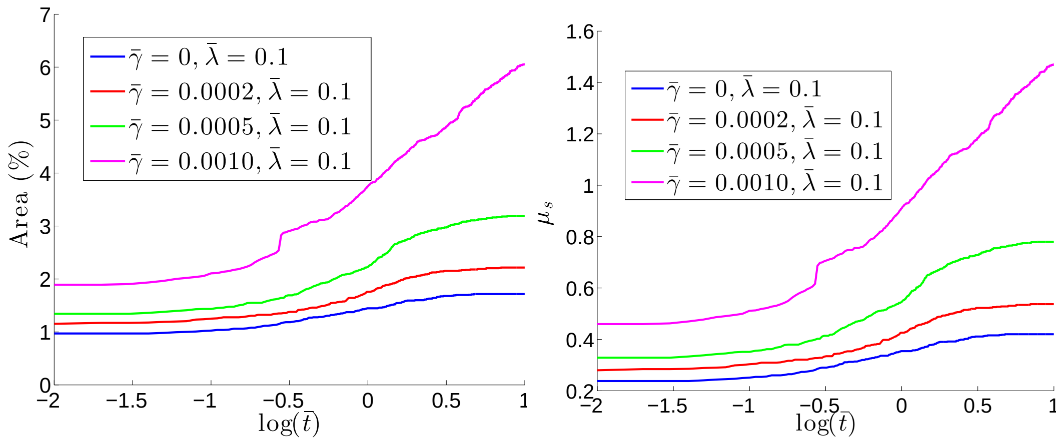

Figure 5.16: Effect of adhesion on friction evolution. The area of contact increases with increasing surface energy. The presence of adhesion also increases the timescale of friction evolution.

Adhesion affects the area and friction evolution in two ways (Figure 5.16). First, the area of contact increases with increasing surface energy. More interestingly, the timescale over which the evolution of area reaches steady state also increases with increasing surface energy. As can be seen in Figure 5.16, when $\bar{\gamma} = 0$ the friction evolution reaches steady state at about $\log \bar{t} = 1$, whereas when $\bar{\gamma} = 0.001$ the friction has not reached steady state at $\log \bar{t} = 1$. This effect of adhesion can be one of the reasons we see a long time of evolution of friction in some experiments [40].

5.5 Concluding remarks

In this chapter, models of the previous chapters were extended to include adhesive interactions. The importance of adhesion at small loads and its effects on static friction evolution were highlighted.

Chapter 6

A force threshold model for adhesion and mode I interfacial cracks

6.1 Introduction

Two popular models for adhesive contact are the JKR model [97] and the DMT model [98]. The connection between the two models was pointed out by Tabor [99]. Maugis showed that the two models can be seen as limiting cases of a Dugdale-type cohesive zone model [100].

In the JKR model, adhesive forces outside the contact zone are assumed to be zero. The stresses at the edge of the contact are tensile and infinite, similar to the stresses at the crack tip in linear elastic fracture mechanics. This chapter proposes a threshold force based model that is similar to the JKR model in that the adhesive forces are confined to the area of contact. A scaling of the threshold force with the discretization size that is very suggestive of linear elastic fracture mechanics emerges from the model. The formulation can also be used to study interfacial mode I cracks.

6.2 Formulation

We consider the contact of two surfaces. We assume one of the surfaces is rigid and represent the other by a set of discrete elements, as shown in Figure 6.1. The only internal degree of freedom of the elements is their length normal to the interface.

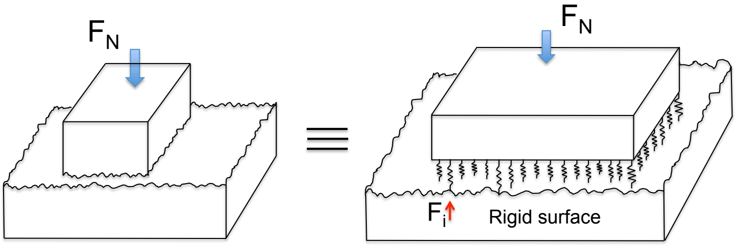

Figure 6.1: Contact of two rough surfaces; one of the rough surfaces is approximated by a set of discrete elements, the other surface is assumed to be rigid.

We assume constitutive equations of the form:

$$u_i = C_{ij} F_j, \tag{6.1}$$

where u_i is the deformation of the element 'i' , F_j is the force on element 'j', C_{ij} is the compliance that captures the effect of the force at location 'j' on an element located at 'i'. We consider two different forms of C_{ij}. The first one is local (called the no elastic interaction case),

$$C_{ij} = C_0 \delta_{ij},$$

and the second one is derived from the superposition of the Boussinesq solution for a point force in a semi-infinite half space (see 3.2 of Chapter 3 for more details) [115],

$$C_{ij} = \frac{1-\nu}{2\pi G}\frac{1}{r_{ij}}, \quad r_{ij} > 0.$$

The Boussinesq solution is singular at the point of application of the load, so the force F_i is interpreted not as a point load, but as a distributed constant pressure over a rectangular area. The displacements caused by such a pressure distribution was derived by Love [77]. This solution, which has a number of logarithmic terms in it, is close to the Boussinesq solution even for neighboring elements, but is not singular at the point of loading. Thus, in computing the displacements at element 'j' due to a force at 'i', we use the Boussinesq solution for all $i \neq j$ and the Love solution for $i = j$. Together, equation (6.1) is obtained (this is referred to as the Boussinesq interaction case).

Adhesion is included in the following manner. Each element is in contact can sustain a maximum tensile force F_{cr}. If the force on the element exceeds F_{cr}, it snaps out of contact and the force becomes zero. As a summary, the governing equations are:

$$
\begin{aligned}
u_i &= C_{ij} F_j, \\
F_i &\le F_{cr}, \\
x_i + y_i &\le d,
\end{aligned}
\tag{6.2}
$$

where $x_i = x_i^0 + u_i$ is the total length of the element 'i', y_i is the height of the rigid surface, and d is the dilatation, which is a measure of the separation between the two surfaces. The third equation is a kinematic constraint condition corresponding to the rigidity of one of the surfaces (the equality is satisfied when an element is in contact). Nondimensionalizing the above equations using L^* for length and F^* for force,

$$
\begin{aligned}
\bar{u}_i &= \bar{C}_{ij} \bar{F}_j, \\
\bar{F}_i &\le \bar{F}_{cr}, \\
\bar{x}_i + \bar{y}_i &= \bar{d}.
\end{aligned}
$$

For the case with Boussinesq interaction, with $F^* = 2\pi G/(1-\nu) L^{*2}$, $\bar{C}_{ij} = 1/\bar{r}_{ij}$.

6.3 Algorithm

The forces and the deformations of the elements are coupled if the elastic interactions are nonlocal (if $\bar{C}_{ij}$ is not diagonal). Thus, when an element snaps out of contact, it changes the forces and deformations of the other elements. Here we describe the algorithm used to handle this issue.

Differentiating the constitutive equation with respect to time (a dummy variable here),

$$\dot{\bar{u}}_i = \bar{C}_{ij}\dot{\bar{F}}_j. \tag{6.3}$$

Since we have to deal with the contact condition, equation (6.3) is split into two parts. Using (1) to represent elements in contact and (2) for ones not in contact,

$$\begin{bmatrix} \dot{\bar{u}}_1 \\ \dot{\bar{u}}_2 \end{bmatrix} = \begin{bmatrix} \bar{C}^E_{11} & \bar{C}^E_{12} \\ \bar{C}^E_{21} & \bar{C}^E_{22} \end{bmatrix} \begin{bmatrix} \dot{\bar{F}}_1 \\ \dot{\bar{F}}_2 \end{bmatrix}. \tag{6.4}$$

Suppose a displacement controlled test is performed by prescribing $\bar{d}(t)$. Given the current state $(\bar{u}_i^n, \bar{F}_i^n)$, the deformation and the forces on all the elements, each time increment involves the following steps:

1. Assume the elements in and out of contact remain that way during a small time step Δt. Given $\dot{\bar{d}}$, the deformation rate for elements in contact is given by:

   $$\dot{\bar{u}}_1 = \dot{\bar{d}}.$$

   For elements not in contact, the force is zero:

   $$\dot{\bar{F}}_2 = 0.$$

2. Determine $\dot{\bar{u}}_2, \dot{\bar{F}}_1$ by solving the linear system 6.4.

3. Make a temporary update of the forces:

   $$\bar{F}_i^{temp} = \bar{F}_i^n + \dot{\bar{F}}_i \Delta t.$$

4. Check if any of the forces have exceeded the critical force. If all elements satisfy the maximum force constraint, accept solution. Else, make corrections in two stages.

5. In the first step, apply a negative force of the same magnitude at those locations where the critical force is exceeded. This is to make sure the force after snap-off

is zero.

$$\text{If } \bar{F}_i^{temp} > \bar{F}_{cr}, \quad \bar{F}_i^{c1} = -\bar{F}_i^{temp},$$

where $\bar{F}^{c1}$ is the first correction force. Calculate the resulting deformations:

$$\bar{u}_i^{c1} = \bar{C}_{ij}\bar{F}_j^{c1}.$$

6. The first two of the three governing equations (6.2) are now satisfied. The last one is not, because of the deformation caused by the correction forces.

7. The kinematic condition for the elements that are in contact but did not snap must be satisfied . So, apply a second correction:

   $$\text{if in contact \& } \bar{F}_i^{temp} < \bar{F}_{cr}, \quad \bar{u}_i^{c2} = -\bar{u}_i^{c1}$$

   and compute the corresponding forces by solving,

   $$\bar{u}_i^{c2} = \bar{C}_{ij}\bar{F}_j^{c2},$$

   where $\bar{u}_i^{c2}, \bar{F}_i^{c2}$ are the second correction deformations and forces.

8. The final forces and deformations are:

   $$\bar{F}_i^{temp} = \bar{F}_i^{temp} + \bar{F}_i^{c1} + \bar{F}_i^{c2},$$

   $$\bar{u}_i^{temp} = \bar{u}_i^{temp} + \bar{u}_i^{c1} + \bar{u}_i^{c2}.$$

9. The forces $\bar{F}_i^{temp}$ may now exceed $\bar{F}_{cr}$. So, go back to step 4.

The above algorithm takes care of the transitions of an element from an in-contact to out-of-contact state. The transitions from out-of-contact to in-contact are made in an explicit way. After updating all the elements using the above algorithm, the kinematic constraint is used as a check for out-of-contact to in-contact transitions.

6.4 Indentation of a spherical surface

Here, we simulate a displacement controlled loading-unloading test of a sphere of radius 20 against a flat rigid surface (with Boussinesq interaction). The critical force $\bar{F}_{cr} = 5 \times 10^{-3}$. The two surfaces are initially apart and the forces and deformations of the elements are initialized to 0. The dilatation is then first decreased and then increased. The evolution of the forces and deformations are computed as outlined in Section 6.3.

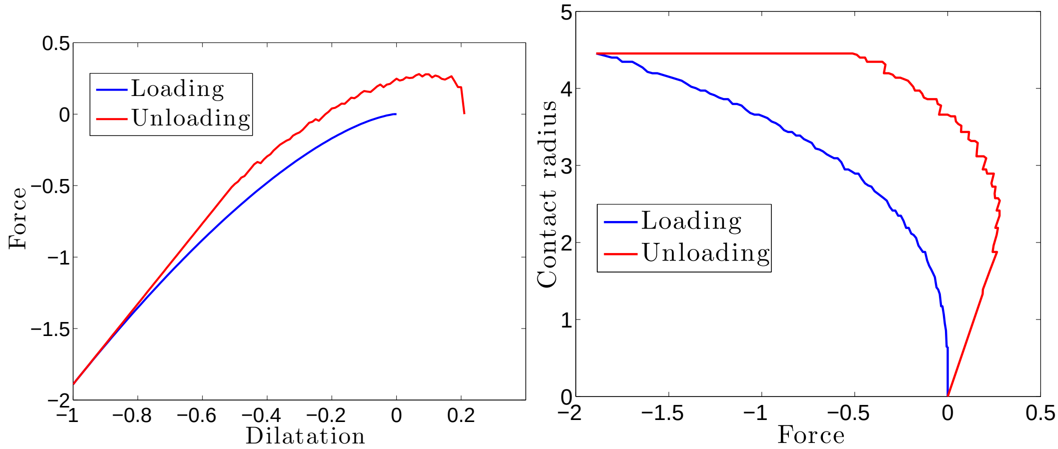

(a) (b)

Figure 6.2: Loading unloading test of a sphere against a rigid flat. Evolution of (a) force with dilatation during and (b) contact radius with force.

As the dilatation is decreased during the loading phase, the compressive force increases (Figure 6.2a). After reaching a minimum (−1 here), dilatation is increased. During unloading, the total force does not retrace the loading path. The elements in contact can sustain a tensile force up to F_{cr}. The hysteresis in the elements leads to the hysteresis of the force evolution. The unloading curve is always higher (force more positive) than the loading curve. As the surfaces are pulled apart, the force reaches a maximum positive value and then goes to zero as all the elements snap off. The snap-off of the elements can be seen as the small wiggles in the force evolution. The wiggles are present only in the unloading part of the curve.

Figure 6.2b shows the evolution of the contact radius with the force. During the loading phase, the compressive force and the contact radius increase. After reaching a minimum dilatation, the unloading phase begins. Initially, the contact radius remains constant as the force increases. This is the phase where none of the elements have broken contact. With further unloading, as the elements reach their critical force and start snapping off, the contact radius decreases and eventually goes back to zero.

6.5 Dependence on discretization size

To study the convergence behavior, the loading-unloading test of the previous section is repeated with different discretization sizes. The sphere is discretized using a grid of 64×64, 128×128, 256×256, and 512×512 elements with $\bar{F}_{cr} = 0.1$. The distance between the elements (Δ) corresponding to these are, $\Delta = 1$, $\Delta = 0.5$, $\Delta = 0.25$, and $\Delta = 0.125$, respectively.

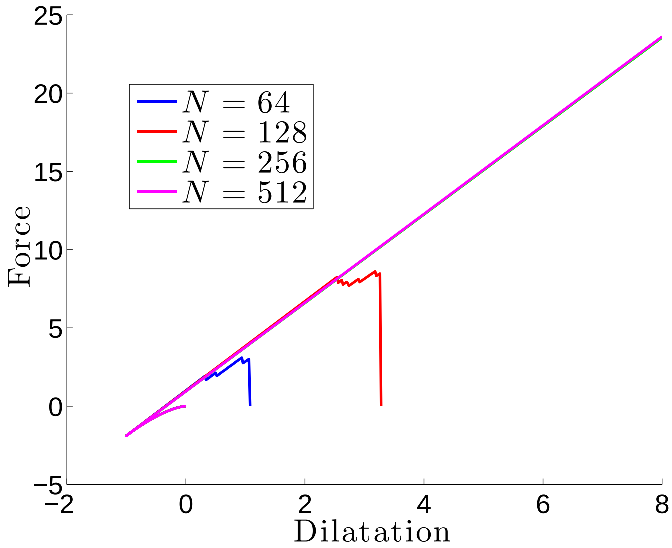

Figure 6.3: Force evolution with dilatation during a loading unloading test of a sphere at different discretizations. The unloading phase is discretization dependent and the maximum tensile force increases without bound with increasing N.

We find that the response is discretization dependent (Figure 6.3). During the loading and the initial part of the unloading phases, the four curves coincide with each other. But as the elements start snapping off, there is divergence between the curves. The maximum tensile force increases without bound with increasing N. For the curves corresponding to $N = 256$ and $N = 512$, no element has broken contact during the simulation (the $N = 256$ curve is not visible since it lies underneath the $N = 512$ curve).

The existence of the divergence only during the unloading phase suggests that for convergence, $\bar{F}_{cr}$ cannot be independent of the discretization size. Figure 6.3 suggests that $\bar{F}_{cr}$ must decrease with the discretization size. The question is, if there is one, what is the right scaling of $\bar{F}_{cr}$ with the discretization size?

6.6 Scaling of critical force with discretization size

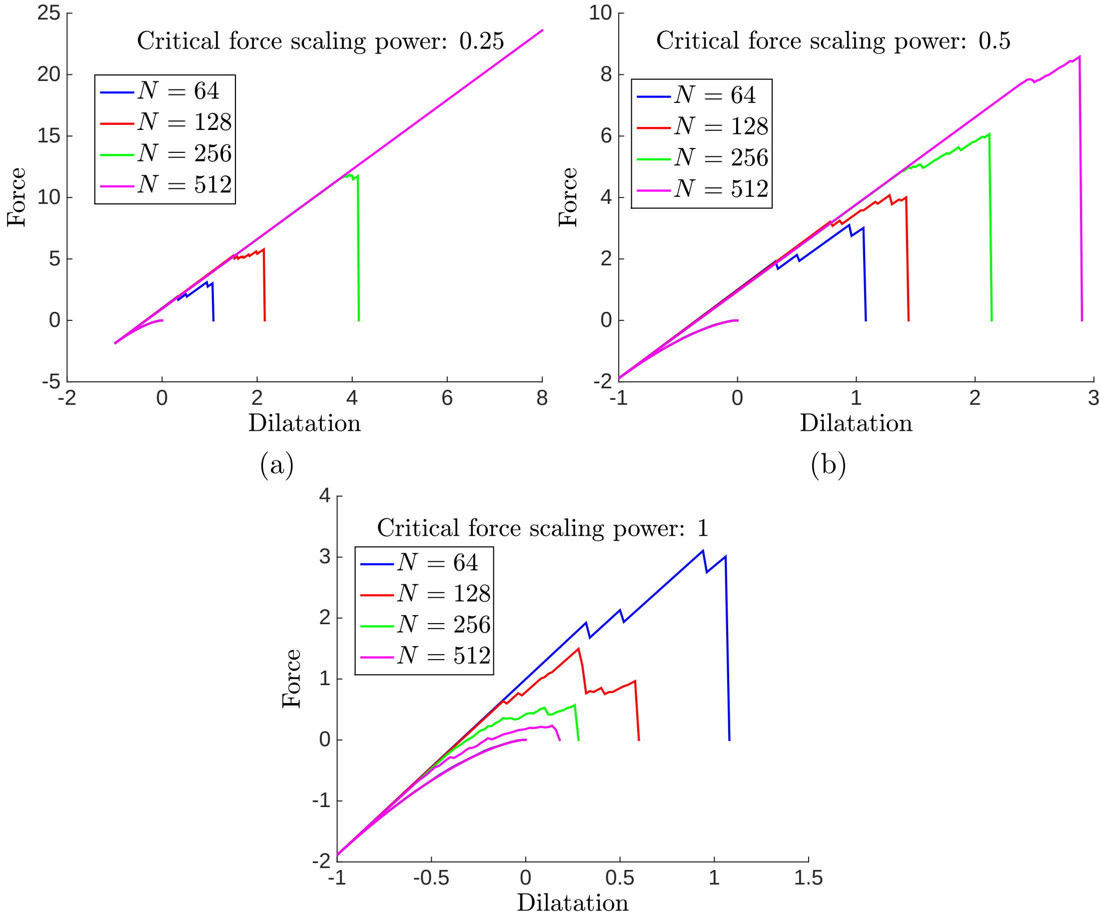

(a)

(b)

(c)

Figure 6.4: Evolution of force with dilatation for a loading-unloading test of a sphere with different scalings of the critical force: (a) $\alpha = 0.25$, (b) $\alpha = 0.5$, and (c) $\alpha = 1$.

We consider scalings of the form:

$$\bar{F}_{cr} = \bar{F}_{cr}^{0} A^{\alpha},$$

where $A = \Delta x \Delta y$ is the area of an element, and $\bar{F}_{cr}^{0}$ is a constant. The loading-unloading tests of the previous section are repeated but with different scalings: $\alpha = 0.25, 0.5$, and 1 (the previous section corresponds to $\alpha = 0$). $\bar{F}_{cr}^{0}$ is set to 0.1.

In all three cases, there is no convergence with increasing N during the unloading phase (Figure 6.4). There is however, something interesting to observe. For $\alpha = 0.25$ and $\alpha = 0.5$, the maximum tensile force increases with increasing N but the difference between the curves decreases as we go from $\alpha = 0.25$ to $\alpha = 0.5$. For $\alpha = 1$, the maximum tensile force decreases with increasing N. This suggests that maybe there is an α between 0.5 and 1 for which there is convergence with refinement.

6.7 Is 0.75 the magic number?

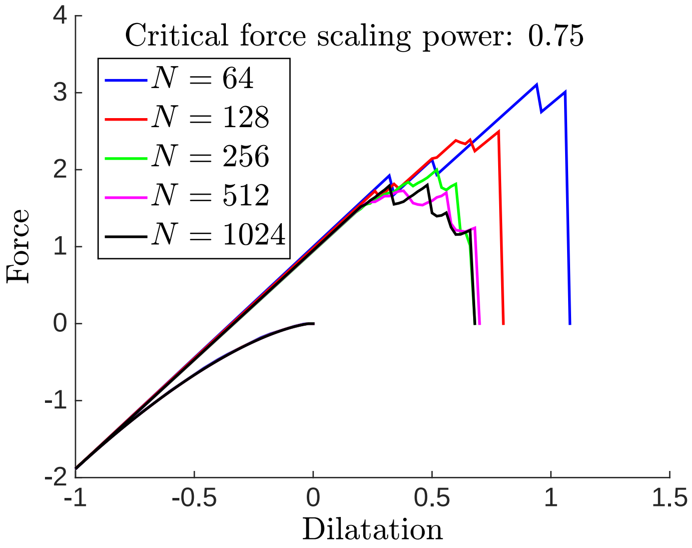

Figure 6.5: Evolution of force with dilatation for a loading unloading test of a sphere with $\alpha = 0.75$. The results seem to converge with increasing N and the maximum tensile force does not vary systematically with N (as it does in Figure 6.4).

Figure 6.5 shows the force evolution during the loading-unloading test for $\alpha = 0.75$ for different discretizations. Although the curves do not lie on top of each other, the maximum tensile force does not vary systematically with N (as it does in Figure 6.4). At this point, it looks like this is purely coincidental. For now, let us assume the scaling with $\alpha = 0.75$ is right:

$$\bar{F}_{cr} = \bar{F}_{cr}^{0} A^{0.75}.$$

This is the scaling for the critical force. Dividing by the area of the element A, the critical stress scales as:

$$\sigma_{cr} = \bar{F}_{cr}/A = \bar{F}_{cr}^{0} A^{-0.25},$$

where σ_{cr} is the critical stress. But $A = \Delta^2$, where Δ is the distance between the elements. Using this:

$$\sigma_{cr} = \frac{F_{cr}^{0}}{\sqrt{\Delta}} \tag{6.5}$$

This scaling is very suggestive of linear elastic fracture mechanics (LEFM)! In LEFM, the stress at the crack tip is given by (for mode I):

$$\sigma \propto \frac{K_I}{\sqrt{r}}, \tag{6.6}$$

where K_I is the mode I stress intensity factor and r is the distance from the crack tip. The criterion for crack propagation is that the stress intensity factor at the crack tip should equal the critical stress intensity factor:

$$K_I = K_{IC},$$

where K_{IC} is the critical stress intensity factor.

Comparing equations (6.5) and (6.6), it appears that with $\alpha = 0.75$, we have an approximation of linear elastic fracture mechanics with $\bar{F}_{cr}^{0}$ serving the role of K_{IC}. This also explains the divergence with varying N in Figures 6.3 and 6.4. Without the $\alpha = 0.75$ scaling, changing N is equivalent to changing K_{IC}.

To test if the above convergence is just an accident, we consider three other geometries: a flat surface, a surface with four hills, and a radial sinusoidal surface. Figures 6.6- 6.8 show the evolution of area and force for $\alpha = 0.75$ for the three cases. In each case, there is convergence with decreasing discretization size. This ensures that the convergence with the spherical surface is not restricted to that particular geometry.

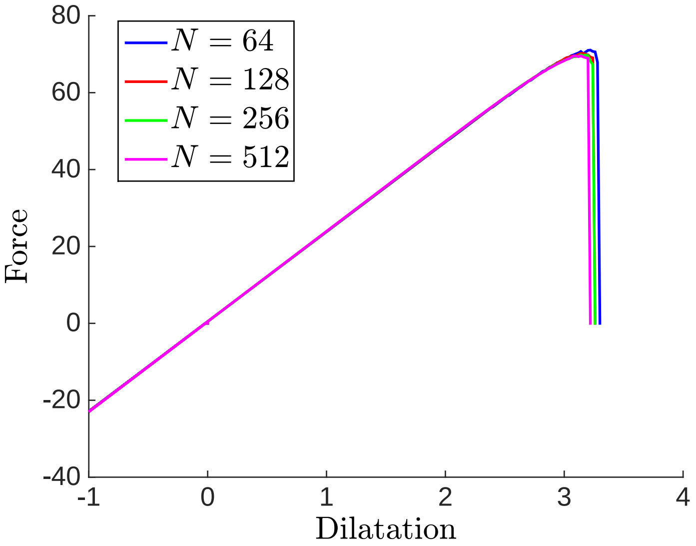

Figure 6.6: Evolution of force with dilatation for a flat surface.

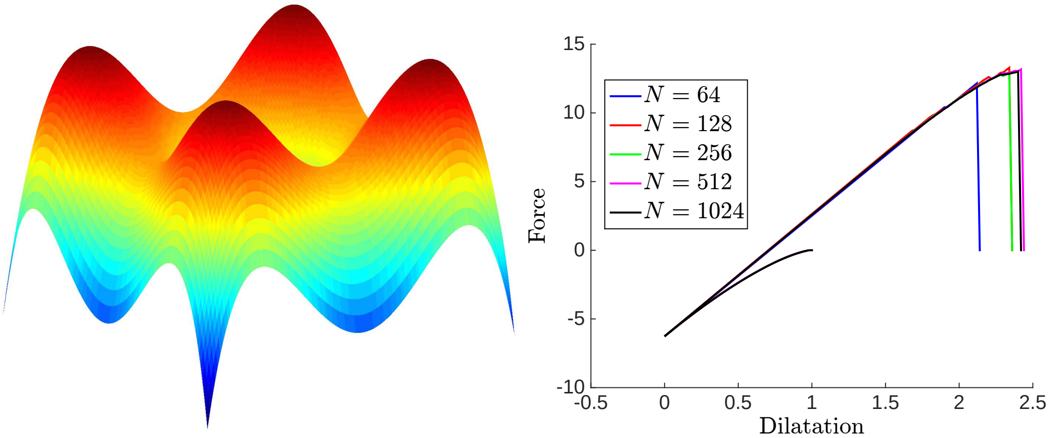

(a) (b)

Figure 6.7: (a) A surface with four hills and (b) its force evolution with dilatation.

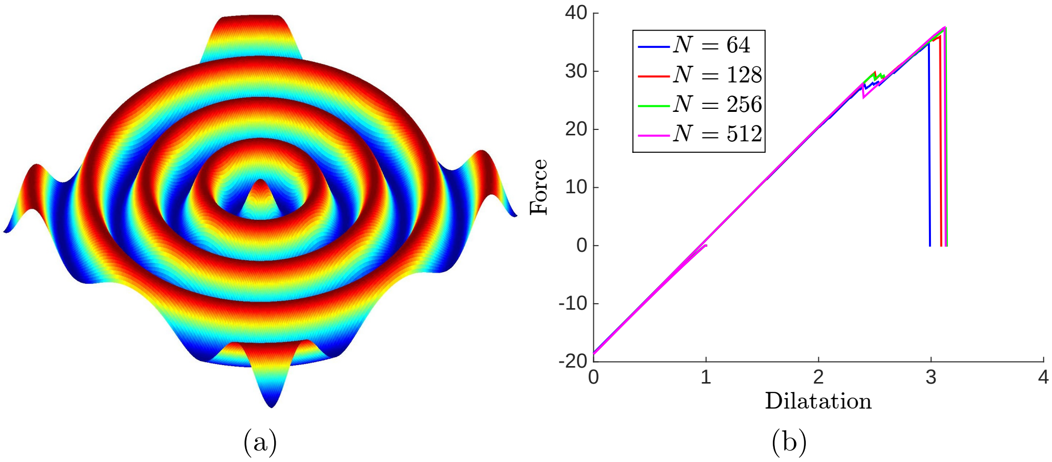

Figure 6.8: (a) A radial sinusoidal surface and (b) its force evolution with dilatation.

6.8 The case with no elastic interactions

Another way to test if the scaling is related to elasticity is to use a constitutive equation not derived from an elasticity solution. Here, constitutive equations with no elastic interactions are considered:

$$\bar{C}_{ij} = \bar{C}_0 \delta_{ij},$$

where $\bar{C}_{ij}$ is the compliance matrix in equation (6.1). If the scaling appears even here, then it probably is unrelated to LEFM.

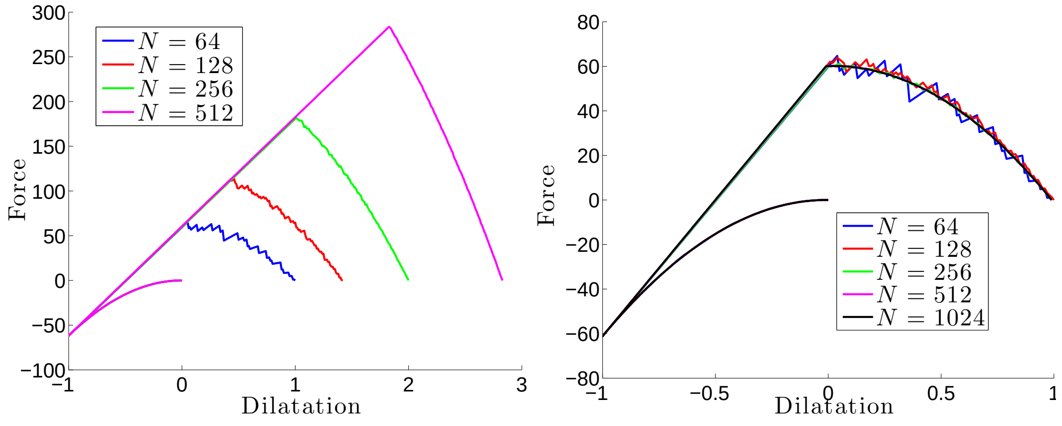

(a) (b)

Figure 6.9: Force evolution with dilatation for the case with no elastic interactions: (a) $\alpha = 0.75$ and (b) $\alpha = 1$. The absence of convergence for $\alpha = 0.75$ and convergence when $\alpha = 1$ suggests that the scaling is interwoven with the elasticity.

The loading-unloading tests are repeated for a sphere. In this case, there is convergence when $\alpha = 1$ and no convergence when $\alpha = 0.75$ (Figure 6.9). The convergence when $\alpha = 1$ is easily understood. Since $\bar{C}_{ij}$ is diagonal, each elements snaps off independently. On doubling N, each element at the larger discretization size is replaced by four smaller elements of one fourth the size. For the total force to the same, the critical force of the smaller elements must be one fourth the critical force of the larger one (apart from small variations corresponding to better geometric representation at the finer discretization).

This lends further support to our conjecture that the $\alpha = 0.75$ scaling with Boussinesq elastic interactions corresponds to an approximation of linear elastic fracture mechanics.

6.9 Concluding remarks

This chapter developed a force threshold based model that can be used to study adhesive contact and mode I interfacial cracks. The great advantage of the model is that it is conceptually simple and very easy to implement. There is strong evidence to think that the model approximates linear elastic fracture mechanics. It remains to be seen if there are deeper connections; such connections would also put the model on a more rigorous footing. It is also interesting to explore extensions of this model to mode II and mode III interfacial cracks.

Chapter 7

Conclusion

7.1 Summary

Our goal in this thesis was to develop a framework to study the interaction between surfaces during static and sliding contact. Our particular interest was in understanding the evolution of static and sliding friction.

The guiding principle was to determine the minimal features that still reproduce qualitatively the observed macroscopic frictional behavior. In that spirit, we showed in Chapter 2 that the collective behavior of one-dimensional independent viscoelastic elements reproduces the various experimentally observed features of static and sliding friction. The two important ingredients in this model, viscoelasticity and rough surfaces, are both necessary and, as we showed, sufficient to reproduce the qualitative behavior.

The next step was to develop the model further to be more representative of the physical system but also amenable to solutions by numerical methods. In Chapter 3, we did this by developing a boundary-element like method that incorporated three-dimensional rough surfaces and long-range elastic interactions. Since friction is affected by a large number of factors, we studied how the different aspects of frictional response, such as the duration of static friction growth, velocity-strengthening and weakening, characteristic slip distance, etc., are influenced by surface roughness, material properties, and the long-range interactions.

In Chapter 4, we included the effects of plasticity by using a viscoplastic material model. The similarity of frictional behavior with the two different material models, viscoelasticity and viscoplasticity, suggests that the qualitative aspects of macroscopic behavior are fairly robust with respect to the microscopic behavior of the contacts. This is probably why in experiments a similar behavior is seen across diverse materials such as rocks, metals, and polymers. In Chapter 5, we showed how adhesion can be included in the framework and studied how it affects friction.

In Chapter 6, we developed a threshold force based model for adhesion. Our goal was to study adhesion but we found a scaling for the critical force that is very suggestive of linear elastic fracture mechanics. It is very interesting that a rather ad hoc discrete model shows a scaling similar to that of a continuum theory. This hints that there are probably deeper connections between the two and that the discrete model can be derived as an approximation of the continuum theory. It also means that for problems of contact mechanics, such discrete models can be valuable tools in understanding various physical phenomena.

7.2 Future work

Here, we suggest a few extensions of the current framework.

7.2.1 Effects of shear forces at the contacts

In all our models, the only degrees of freedom for the discrete elements we have considered (forces and deformations) are normal to the interface. We calculate the shear forces and the friction coefficient as a postprocessing step. However, shear forces at the contacts cause deformations normal to the interface. One way to include the effect of shear forces is to provide the elements with horizontal degrees of freedom. We have used the Boussinesq solution of a point force (normal to interface) on an elastic half-space as the Green's function in our model. This can be replaced by an appropriate Green's function when shear forces are included [116, 115].

7.2.2 Effects of temperature

In our models, we have not considered the effect of temperature. In Chapter 4, we assumed isothermal conditions and, based on some assumptions on the dependence of viscoplastic properties on temperature, studied how friction might depend on temperature. A more realistic way to include effects of temperature would be the following: the heat dissipated at the contacts due to the shear forces and the corresponding increases in temperature are calculated. Then, to see how this heat diffuses, a Green's function corresponding to the diffusion of heat in a half-space due to a localized heat source can be used. This can be used to determine the evolution of temperature during sliding. Further, the material properties can be made temperature dependent. The resulting coupled system of equations can be solved numerically.

This adds another timescale to the ones in our model: the timescale of heat diffusion. The isothermal assumption we made is the limit of very small diffusion timescales (heat diffusion happens much faster than heat generation).

7.2.3 Sliding stability

It is well known that the stability of sliding is intricately related to the frictional properties and the phenomenological rate and state laws have been used in understanding the stability [36, 44, 117]. In this thesis, we have assumed that the surfaces slide at a constant velocity. This can be extended to study the sliding stability. As shown in Figure 7.1, a mass M subject to a normal force F_N, is driven by a spring of stiffness K at a driving speed v_k. The mass is sliding against a rough rigid surface. The governing equations are:

$$v_M = \dot{x}_M,$$

$$M\dot{v}_M = F,$$

$$F_f = \mu F_N,$$

where x_M, v_M are the position and velocity of the mass, F, F_f are the total and frictional forces, and μ is the friction coefficient. The total force can be calculated knowing the force in the spring $K(x_K - x_M)$, where x_K is the position of the spring, and the frictional force F_f.

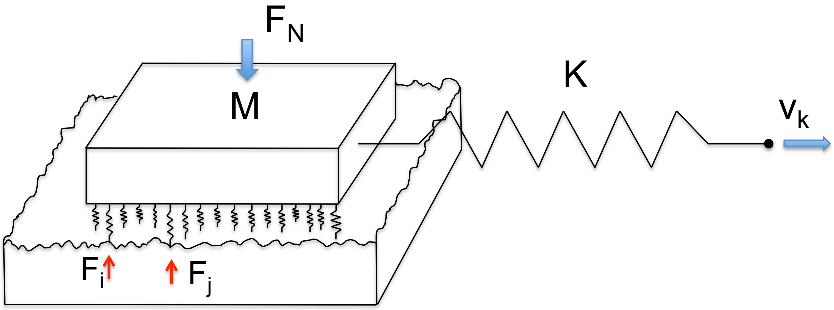

Figure 7.1: Extension of the framework proposed in this thesis to study sliding stability. The states of the mass M and the underlying discrete ensemble are evolved together.

The friction coefficient is determined by evolving the ensemble of discrete elements as in Chapters 3 and 4. The evolution of the ensemble and the evolution of the mass are thus coupled. The stability can properties can then be studied as a function of M, F_N, K, v_k, and the surface and material properties that determine the friction coefficient.

Some experiments show that the stability behavior is sensitive to noise in certain parameteric regime [117]. It would be interesting to see if this noise sensitivity comes from the noise in the rough surfaces.

Appendices

Appendix A

Rough surface generation

In the last few decades, there have been great advances in experimental techniques to probe surfaces. The development of Scanning Tunneling Microscopy (STM) and Atomic Force Microscopy (AFM) has allowed us to characterize the nature of rough surfaces with atomic scale resolution. At larger length scales, other stylus based and optical methods can be used. For a survey of the various surface characterization methods, see [81, 15].

Surface topography measurements using a variety of techniques have shown that rough surfaces have features at many length scales and are statistically self-affine (statistically similar appearance at different magnifications) [118, 15]. Thus, rough surfaces can be characterized as fractals [119]. An advantage of the fractal characterization is that the fractal parameters are intrinsic to the surface and scale independent. The power spectrum of a fractal surface decays as a polynomial in the spatial frequency and the power of the polynomial is related to the fractal dimension. The fractal characterization of surfaces has been used in many studies of contact [27, 120, 28].

Rough surfaces are also characterized as a stochastic process [56, 60, 57]. The stochastic process is defined by prescribing two functions. The first is the probability distribution of heights, and for many surfaces, this is seen to be Gaussian [26, 60]. The second function is the autocorrelation which describes the spatial features of roughness. For many surfaces, the autocorrelation decays as an Exponential or as a Gaussian [60, 66].

From a computational perspective, to study the contact of rough surfaces, it is important to generate surfaces with realistic topographies. In this thesis, we have used the stochastic characterization of rough surfaces. Here, we describe how we generate rough surfaces. We have used the method proposed by Hu and Tonder in the paper [121].

We would like to generate three-dimensional random surfaces with a Gaussian probability distribution of heights and an Exponential or Gaussian autocorrelation. The approach is to first generate a set of uncorrelated Gaussian random heights and then use a linear filter. Since the filter is linear, the final heights are linear combinations of Gaussian random variables and will thus also be Gaussian random numbers. The weights of the filter are chosen such that final heights have the desired autocorrelation.

Without loss of generality, the mean of the Gaussian probability distribution can be set to 0; this is equivalent to choosing the mean height level as the reference level to measure heights. That leaves one parameter, the standard deviation of the distribution, also known as the rms roughness of the surface. Given the standard deviation σ, we first generate a set of uncorrelated random numbers $\chi(k,l)$ with the probability distribution,

$$P(\chi) = \frac{1}{\sqrt{2\pi}\sigma} e^{-\frac{\chi^2}{2\sigma^2}}. \tag{A.1}$$

The indices (k,l) are the spatial indices along two orthogonal directions on the surface. We then use a linear filter to determine the final heights,

$$z(I,J) = \sum_{k=0}^{n-1}\sum_{l=0}^{m-1} h(k,l)\chi(I-k, J-l), \tag{A.2}$$

where $h(k,l)$ is the linear filter and $z(I,J)$ are the final heights. $h(k,l)$ must be determined such that $z(I,J)$ has the prescribed autocorrelation. Taking the Fourier transform on both sides of equation A.2,

$$Z(\omega_x,\omega_y) = H(\omega_x,\omega_y)X(\omega_x,\omega_y), \tag{A.3}$$

where $Z(\omega_x, \omega_y)$ and $X(\omega_x, \omega_y)$ are the Fourier transforms of the input and output sequences, respectively, and $H(\omega_x, \omega_y)$, called the transfer function, is given by,

$$H(\omega_x, \omega_y) = \sum_{k=0}^{n-1} \sum_{l=0}^{m-1} h(k, l) e^{-ik\omega_x} e^{-il\omega_y}. \tag{A.4}$$

For the linear filter A.2, if S_{zz} and $S_{\chi\chi}$ are the power spectral densites (PSD) of the output and input, respectively,

$$S_{zz}(\omega_x, \omega_y) = |H(\omega_x, \omega_y)|^2 S_{\chi\chi}(\omega_x, \omega_y). \tag{A.5}$$

For a stationary random process $z(I, J)$, the autocorrelation is defined as,

$$R_{zz}(k, l) = \mathrm{E}\{z(I, J) z(I + k, J + l)\},$$

where E{} denotes mathematical expectation. If we assume the process is ergodic,

$$R_{zz}(k, l) = \frac{1}{NM} \sum_{I=0}^{N-1} \sum_{J=0}^{M-1} z(I, J) z(I + k, J + l) \tag{A.6}$$

as $N, M \to \infty$. The Fourier transform of the autocorrelation is also the PSD,

$$S_{zz}(\omega_x, \omega_y) = \frac{1}{nm} \sum_{k=-n/2+1}^{n/2-1} \sum_{l=-m/2+1}^{m/2-1} R_{zz}(k, l) e^{-ik\omega_x} e^{-il\omega_y}. \tag{A.7}$$

Equations A.5 and A.7 can be used to establish a link between the prescribed autocorrelation and the weights of the linear filter. The power spectrum $S_{\chi\chi}(\omega_x, \omega_y)$ is a constant since the noise $\eta(k, l)$ is uncorrelated. This constant can be set to 1 since all operations are linear. This will change the rms roughness of the generated surface but that can be fixed by an appropriate scaling of the heights. The steps in determining the weights of the linear filter are:

1. Given the autocorrelation $R_{zz}(k, l)$, compute its fourier transform to get $S_{zz}(\omega_x, \omega_y)$ (Equation A.7).

2. Determine the PSD of the filter $H(\omega_x, \omega_y)$ using the Equation A.5 as,

$$H(\omega_x, \omega_y) = (S_{zz}(\omega_x, \omega_y))^{0.5}$$

3. Determing the filter $h(k, l)$ by an inverse Fourier transform of $H(\omega_x, \omega_y)$ (Equation A.4).

Using the uncorrelated heights $\chi(I, J)$ and the weights $h(k, l)$, the heights of the correlated surface $z(I, J)$ can be determined using the Equation A.2.

To minimize the effect of boundaries, we generate sufaces that are much larger than the surfaces required for our computation. For example, most of our calculations are done on systems of size 256×256 or 512×512. We generate surfaces of size 8000×8000 and extract surfaces of the desired size from the larger system. We also extract the smaller surfaces sufficiently far from the boundaries of the larger system (distance from the boundaries should be large enough for weights $h(k, l)$ to be negligible).

In Equation A.2, we have to pick values for n and m, the number of terms used in the filter. The filter weights $h(k, l)$ decay with increasing k and l. We choose n and m such that $h(k, l) < 10^{-5} h(0, 0)$.

A.1 Gaussian autocorrelation

For surfaces with Gaussian autocorrelation,

$$R_{zz}(\delta_x, \delta_y) = \mathrm{E}\{z(x, y) z(x + \delta_x, y + \delta_y)\} = \sigma^2 e^{-(\delta_x^2 + \delta_y^2)/\beta^2},$$

where β is called the correlation length. The power spectral density is given by its Fourier transform,

$$S(\omega_x, \omega_y) = \frac{1}{2} \sigma^2 \beta^2 e^{-\beta^2 (\omega_x^2 + \omega_y^2)/4}. \tag{A.8}$$

If we use N points to discretize a correlation length,

$$N \Delta x = \beta, \quad N \Delta y = \beta.$$

Using $\delta_x = k\Delta x, \delta_y = l\Delta y$,

$$R_{zz}(k,l) = \sigma^2 e^{-(k^2+l^2)/N^2}.$$

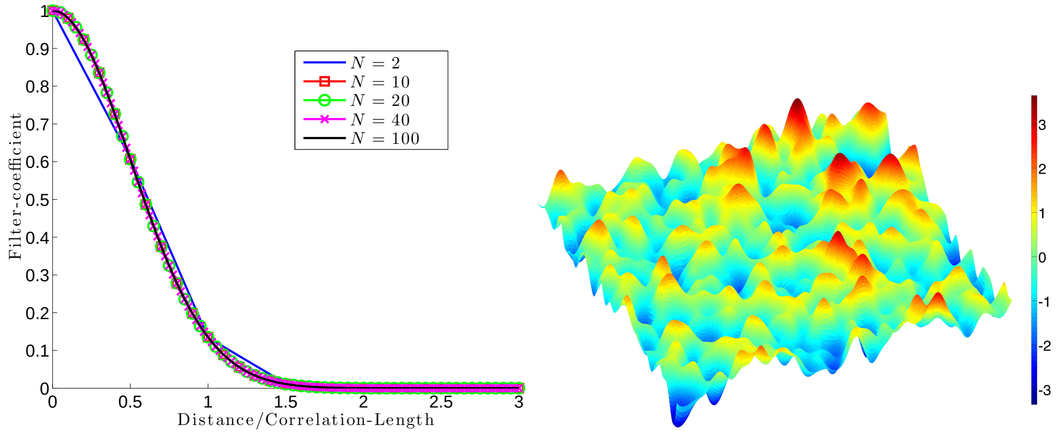

(a) (b)

Figure A.1: (a) Decay of filter coefficients with distance for the Gaussian autocorrelation. Points that are 3 or more correlation lengths apart can be considered to be independent of each other. (b) One realization of a rough surface with a Gaussian height distribution and a Gaussian autocorrelation.

Figure A.1a shows the decay of the filter coefficients with distance with different discretization sizes ($N = 2, 10, 20, 40, 100$). The highest resolved frequency using N points to discretize one correlation length is $\omega_{\max} = N/2\beta$. The filter coefficients decay rapidly with distance, and are very small at about three correlation lengths. This means that the surface heights of points that are three correlation lengths or more apart are effectively independent of each other. Further, beyond $N = 10$, there is little variation in the filter coefficients. This is because the power spectrum decays very rapidly (Equation A.8) with increasing spatial frequency and there is little contribution from the frequencies beyond that corresponding to $N = 10$. Figure A.1b shows one realization of a rough surface with a Gaussian distribution of heights and a Gaussian autocorrelation. The rms roughness of the surface $\sigma = 1$ and the correlation length $\beta = 10$.

A.2 Exponential autocorrelation

For surfaces with Exponential autocorrelation,

$$R_{zz}(\delta_x, \delta_y) = \mathrm{E}\{z(x,y)z(x+\delta_x, y+\delta_y)\} = \sigma^2 e^{-(\delta_x^2+\delta_y^2)^{1/2}/\beta},$$

where β is called the correlation length. The power spectral density is given by,

$$S(\omega_x, \omega_y) = \frac{2\pi\sigma^2\beta^2}{\left[1+\left(\omega_x^2+\omega_y^2\right)\beta^2\right]^{3/2}}. \tag{A.9}$$

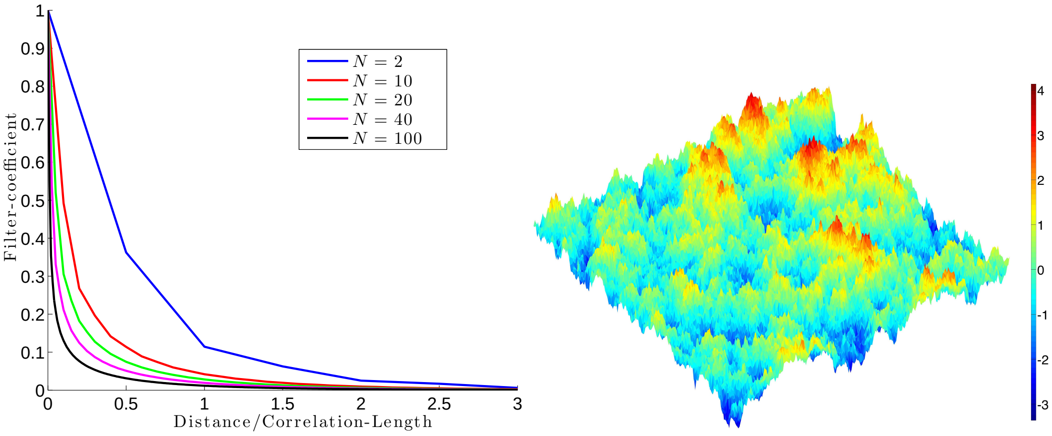

(a) (b)

Figure A.2: (a) Decay of filter coefficients with distance for the Exponential autocorrelation. Points that are 3 or more correlation lengths apart can be considered to be independent of each other. (b) One realization of a rough surface with a Exponential height distribution and a Exponential autocorrelation.

Figure A.2a shows the decay of the filter coefficients with distance with different discretization sizes ($N = 2, 10, 20, 40, 100$). In this case too, the filter coefficients decay rapidly with distance, and are very small at about three correlation lengths. However, we do not see the saturation beyond $N = 10$ (or any other frequency) we saw in the Guassian autocorrelation case. This is because the power spectrum decays only polynomially (Equation A.9). In fact, for $\left(\omega_x^2+\omega_y^2\right)^{1/2}\beta \gg 1$, the power spectrum decays as $1/\omega^3$ (where $\omega = (\omega_x^2+\omega_y^2)^{1/2}$). This corresponds to a fractal dimension of 2.5 (or a Hurst exponent of 0.5).

Figure A.2b shows one realization of a rough surface with an exponential distribution of heights and an exponential autocorrelation. The rms roughness of the surface is $\sigma = 1$ and the correlation length is $\beta = 10$.

Bibliography

[1] Duncan Dowson and Duncan Dowson. *History of tribology*. Longman London, 1979.

[2] M. Urbakh, J. Klafter, D. Gourdon, and J. Israelachvili. The nonlinear nature of friction. *Nature*, 430:525–528, July 2004.

[3] JH Dieterich. Applications of rate-and state-dependent friction to models of fault slip and earthquake occurrence. *Treatise on Geophysics*, 4:107–129, 2007.

[4] Nikhil S Tambe and Bharat Bhushan. Scale dependence of micro/nano-friction and adhesion of mems/nems materials, coatings and lubricants. *Nanotechnology*, 15(11):1561, 2004.

[5] IR McFadyen, EE Fullerton, and MJ Carey. State-of-the-art magnetic hard disk drives. *MRS Bulletin-Materials Research Society*, 31(5):379, 2006.

[6] Bharat Bhushan. Nanotribology and nanomechanics of mems/nems and biomems/bionems materials and devices. *Microelectronic Engineering*, 84(3):387–412, 2007.

[7] C Mathew Mate. Tribology on the small scale. *Oxford University Press, Oxford*, 2008.

[8] C. H. Scholz. Earthquakes and friction laws. *Nature*, 391(6662):37–42, January 1998.

[9] C Marone. Laboratory-derived friction laws and their application to seismic faulting. *ANNUAL REVIEW OF EARTH AND PLANETARY SCIENCES*, 26:643–696, 1998.

[10] Simon T Tse and James R Rice. Crustal earthquake instability in relation to the depth variation of frictional slip properties. *Journal of Geophysical Research: Solid Earth (1978–2012)*, 91(B9):9452–9472, 1986.

[11] Yoshihiro Kaneko, Jean-Philippe Avouac, and Nadia Lapusta. Towards inferring earthquake patterns from geodetic observations of interseismic coupling. *Nature Geoscience*, 3(5):363–369, 2010.

[12] Sylvain Barbot, Nadia Lapusta, and Jean-Philippe Avouac. Under the hood of the earthquake machine: toward predictive modeling of the seismic cycle. *Science*, 336(6082):707–710, 2012.

[13] Hiroyuki Noda and Nadia Lapusta. Stable creeping fault segments can become destructive as a result of dynamic weakening. *Nature*, 493(7433):518–521, 2013.

[14] H Peter Jost. Tribology - origin and future. *Wear*, 136(1):1–17, 1990.

[15] Bharat Bhushan. *Principles and applications of tribology.* John Wiley & Sons, 2013.

[16] J Scheibert, S Leurent, A Prevost, and G Debregeas. The role of fingerprints in the coding of tactile information probed with a biomimetic sensor. *Science Signalling*, 323(5920):1503, 2009.

[17] E Wandersman, R Candelier, G Debrégeas, and Alexis Prevost. Texture-induced modulations of friction force: the fingerprint effect. *Physical review letters*, 107(16):164301, 2011.

[18] Joseph M Romano, Kaijen Hsiao, Günter Niemeyer, Sachin Chitta, and Katherine J Kuchenbecker. Human-inspired robotic grasp control with tactile sensing. *Robotics, IEEE Transactions on*, 27(6):1067–1079, 2011.

[19] MC Mate and RW Carpick. A sense for touch. *Nature*, pages 8–9, 2011.

[20] Roland S Johansson and J Randall Flanagan. Coding and use of tactile signals from the fingertips in object manipulation tasks. *Nature reviews. Neuroscience*, 10(5):345–59, May 2009.

[21] Heinrich Hertz. Über die berührung fester elastischer körper. 1882.

[22] KL Johnson, K Kendall, and AD Roberts. Surface energy and the contact of elastic solids. *Proceedings of the Royal Society of London. A. Mathematical and Physical Sciences*, 324(1558):301–313, 1971.

[23] Bharat Bhushan. Contact mechanics of rough surfaces in tribology: single asperity contact. *Applied mechanics reviews*, 49:275, 1996.

[24] Izabela Szlufarska, Michael Chandross, and Robert W Carpick. Recent advances in single-asperity nanotribology. *Journal of Physics D: Applied Physics*, 41(12):123001, June 2008.

[25] J. F. Archard. Elastic deformation and the laws of friction. *Proceedings of the Royal Society of London. Series A. Mathematical and Physical Sciences*, 243(1233):190–205, 1957.

[26] J. A. Greenwood and J. B. P. Williamson. Contact of nominally flat surfaces. *Proceedings of the Royal Society of London. Series A. Mathematical and Physical Sciences*, 295(1442):300–319, 1966.

[27] A. Majumdar and B. Bhushan. Fractal model of elastic-plastic contact between rough surfaces. *Journal of Tribology*, 113(1):1–11, 1991.

[28] Bo NJ Persson. Theory of rubber friction and contact mechanics. *The Journal of Chemical Physics*, 115(8):3840–3861, 2001.

[29] M Ciavarella, G Demelio, JR Barber, and Yong Hoon Jang. Linear elastic contact of the weierstrass profile. *Proceedings of the Royal Society of London.*

Series A: Mathematical, Physical and Engineering Sciences, 456(1994):387–405, 2000.

[30] Frank Philip Bowden and David Tabor. The friction and lubrication of solids. *Clarendon Press, 1986*, page 374, 1986.

[31] B.N.J. Persson. *Sliding friction: physical principles and applications*. Nanoscience and technology. Springer, 2000.

[32] Ernest Rabinowicz. *Friction and wear of materials*, volume 2. Wiley New York, 1965.

[33] J. H. Dieterich. Time-dependent friction and the mechanics of stick-slip. *Pure and Applied Geophysics*, 116:790–806, July 1978.

[34] Christopher H Scholz. *The mechanics of earthquakes and faulting*. Cambridge university press, 2002.

[35] N. M. Beeler, T. E. Tullis, and J. D. Weeks. The roles of time and displacement in the evolution effect in rock friction. *Geophysical Research Letters*, 21:1987–1990, September 1994.

[36] A. Ruina. Slip instability and state variable friction laws. *Journal of Geophysical Research*, 881:10359–10370, December 1983.

[37] Vikas Prakash and Rodney J Clifton. Time resolved dynamic friction measurememts in pressure-shear. *ASME APPLIED MECHANICS DIVISION-PUBLICATIONS-AMD*, 165:33–33, 1993.

[38] MF Linker and JH Dieterich. Effects of variable normal stress on rock friction: Observations and constitutive equations. *Journal of Geophysical Research: Solid Earth (1978–2012)*, 97(B4):4923–4940, 1992.

[39] RSH Richardson and H Nolle. Surface friction under time-dependent loads. *Wear*, 37(1):87–101, 1976.

[40] J. H. Dieterich. Time-dependent friction in rocks. *J. Geophys. Res.*, 77:3690–97, 1972.

[41] J. H. Dieterich and B. D. Kilgore. Direct observation of frictional contacts: New insights for state-dependent properties. *Pure and Applied Geophysics*, 143:283–302, March 1994.

[42] J. H. Dieterich. Modeling of rock friction 1. Experimental results and constitutive equations. *Journal of Geophysical Research*, 84:2161–2168, May 1979.

[43] James H. Dieterich. *Constitutive Properties of Faults With Simulated Gouge*, pages 103–120. American Geophysical Union, 1981.

[44] AL Ruina. Stability of steady frictional slipping. *Journal of applied mechanics*, 50:343–349, 1983.

[45] David A Lockner, Carolyn Morrow, Diane Moore, and Stephen Hickman. Low strength of deep san andreas fault gouge from safod core. *Nature*, 472(7341):82–85, 2011.

[46] Y Brechet and Y Estrin. The effect of strain rate sensitivity on dynamic friction of metals. *Scripta metallurgica et materialia*, 30(11):1449–1454, 1994.

[47] Y Estrin and Y Bréchet. On a model of frictional sliding. *pure and applied geophysics*, 147(4):745–762, 1996.

[48] P Berthoud, T Baumberger, C Gsell, and J-M Hiver. Physical analysis of the state-and rate-dependent friction law: Static friction. *Physical review B*, 59(22):14313, 1999.

[49] T. Baumberger, P. Berthoud, and C. Caroli. Physical analysis of the state- and rate-dependent friction law. ii. dynamic friction. *Phys. Rev. B*, 60:3928–3939, Aug 1999.

[50] Thibaut Putelat, Jonathan H.P. Dawes, and John R. Willis. On the microphysical foundations of rate-and-state friction. *Journal of the Mechanics and Physics of Solids*, 59(5):1062 – 1075, 2011.

[51] EA Jagla. Towards a modeling of the time dependence of contact area between solid bodies. *Journal of Statistical Mechanics: Theory and Experiment*, 2010(06):P06006, 2010.

[52] CY Hui, YY Lin, and JM Baney. The mechanics of tack: viscoelastic contact on a rough surface. *Journal of Polymer Science Part B: Polymer Physics*, 38(11):1485–1495, 2000.

[53] Srivatsan Hulikal, Kaushik Bhattacharya, and Nadia Lapusta. Collective behavior of viscoelastic asperities as a model for static and kinetic friction. *Journal of the Mechanics and Physics of Solids*, 76:144–161, March 2015.

[54] James H Dieterich and Brian D Kilgore. Imaging surface contacts: power law contact distributions and contact stresses in quartz, calcite, glass and acrylic plastic. *Tectonophysics*, 256(1):219–239, 1996.

[55] L Cheng, X Xia, LE Scriven, and WW Gerberich. Spherical-tip indentation of viscoelastic material. *Mechanics of materials*, 37(1):213–226, 2005.

[56] Michael S Longuet-Higgins. The statistical analysis of a random, moving surface. *Philosophical Transactions of the Royal Society of London. Series A, Mathematical and Physical Sciences*, pages 321–387, 1957.

[57] Richard S Sayles and Tom R Thomas. Surface topography as a nonstationary random process. 1978.

[58] P Ranganath Nayak. Random process model of rough surfaces. *Journal of Lubrication Technology*, 93:398, 1971.

[59] PR Nayak. Random process model of rough surfaces in plastic contact. *Wear*, 26(3):305–333, 1973.

[60] David John Whitehouse and JF Archard. The properties of random surfaces of significance in their contact. *Proceedings of the Royal Society of London. A. Mathematical and Physical Sciences*, 316(1524):97–121, 1970.

[61] James R. Rice, Nadia Lapusta, and K. Ranjith. Rate and state dependent friction and the stability of sliding between elastically deformable solids. *Journal of the Mechanics and Physics of Solids*, 49(9):1865 – 1898, 2001.

[62] Lior Kogut and Izhak Etsion. A semi-analytical solution for the sliding inception of a spherical contact. *Journal of tribology*, 125(3):499–506, 2003.

[63] JF Archard. Single contacts and multiple encounters. *Journal of Applied Physics*, 32(8):1420–1425, 1961.

[64] JT Oden and JAC Martins. Models and computational methods for dynamic friction phenomena. *Computer methods in applied mechanics and engineering*, 52(1):527–634, 1985.

[65] Hannes Risken. *The Fokker-Planck equation: Methods of solution and applications*, volume 18. Springer Verlag, 1996.

[66] JA Ogilvy and JR Foster. Rough surfaces: Gaussian or exponential statistics? *Journal of Physics D: Applied Physics*, 22(9):1243, 1989.

[67] Toshihiko Shimamoto. Transition between frictional slip and ductile flow for halite shear zones at room temperature. *Science*, 231(4739):711–714, 1986.

[68] W Yan and K Komvopoulos. Contact analysis of elastic-plastic fractal surfaces. *Journal of Applied Physics*, 84(7):3617–3624, 1998.

[69] S Hyun, L Pei, J-F Molinari, and MO Robbins. Finite-element analysis of contact between elastic self-affine surfaces. *Physical Review E*, 70(2):026117, 2004.

[70] PK Gupta and JA Walowit. Contact stresses between an elastic cylinder and a layered elastic solid. *Journal of Tribology*, 96(2):250–257, 1974.

[71] MN Webster and RS Sayles. A numerical model for the elastic frictionless contact of real rough surfaces. *Journal of Tribology*, 108(3):314–320, 1986.

[72] Ning Ren and Si C Lee. Contact simulation of three-dimensional rough surfaces using moving grid method. *TRANSACTIONS-AMERICAN SOCIETY OF MECHANICAL ENGINEERS JOURNAL OF SOLAR ENERGY ENGINEERING*, 115:597–597, 1993.

[73] Y Ju and TN Farris. Spectral analysis of two-dimensional contact problems. *Journal of tribology*, 118(2):320–328, 1996.

[74] IA Polonsky and LM Keer. A Fast and Accurate Method for Numerical Analysis of Elastic Layered Contacts. *Journal of tribology*, 122(January), 2000.

[75] Geng Liu, Qian Wang, and Shuangbiao Liu. A three-dimensional thermal-mechanical asperity contact model for two nominally flat surfaces in contact. *Journal of tribology*, 123(3):595–602, 2001.

[76] Can K Bora, Michael E Plesha, and Robert W Carpick. A numerical contact model based on real surface topography. *Tribology Letters*, 50(3):331–347, 2013.

[77] Augustus Edward Hough Love. The stress produced in a semi-infinite solid by pressure on part of the boundary. *Philosophical Transactions of the Royal Society of London. Series A, Containing Papers of a Mathematical or Physical Character*, pages 377–420, 1929.

[78] Satish Balay, Shrirang Abhyankar, Mark F. Adams, Jed Brown, Peter Brune, Kris Buschelman, Victor Eijkhout, William D. Gropp, Dinesh Kaushik, Matthew G. Knepley, Lois Curfman McInnes, Karl Rupp, Barry F. Smith, and Hong Zhang. PETSc Web page. `http://www.mcs.anl.gov/petsc`, 2014.

[79] Leslie Greengard and Vladimir Rokhlin. A fast algorithm for particle simulations. *Journal of computational physics*, 73(2):325–348, 1987.

[80] Alexander T Ihler. An overview of fast multipole methods. *Area Exam, April*, 2004.

[81] Tom Thomas. *Rough surfaces second edition*. London: Imperial College Press, 1999.

[82] Ho-Cheol Kim and Thomas P. Russell. Contact of elastic solids with rough surfaces. *Journal of Polymer Science Part B: Polymer Physics*, 39(16):1848–1854, August 2001.

[83] YZ Hu and K Tonder. Simulation of 3-d random rough surface by 2-d digital filter and fourier analysis. *International Journal of Machine Tools and Manufacture*, 32(1):83–90, 1992.

[84] James R. Rice, Nadia Lapusta, and K. Ranjith. Rate and state dependent friction and the stability of sliding between elastically deformable solids. *Journal of the Mechanics and Physics of Solids*, 49(9):1865 – 1898, 2001.

[85] Vikas Prakash and Rodney J Clifton. Time resolved dynamic friction measurememts in pressure-shear. *ASME Applied Mechanics Division-publications-AMD*, 165:33–33, 1993.

[86] Harold J Frost and Michael F Ashby. Deformation mechanism maps: the plasticity and creep of metals and ceramics. 1982.

[87] ML Blanpied, DA Lockner, and JD Byerlee. Fault stability inferred from granite sliding experiments at hydrothermal conditions. *Geophysical Research Letters*, 18(4):609–612, 1991.

[88] CH Mastrangelo. Adhesion-related failure mechanisms in micromechanical devices. *Tribology Letters*, 3(3):223–238, 1997.

[89] Roya Maboudian and Roger T Howe. Critical review: adhesion in surface micromechanical structures. *Journal of Vacuum Science & Technology B*, 15(1):1–20, 1997.

[90] Frank W DelRio, Maarten P de Boer, James A Knapp, E David Reedy, Peggy J Clews, and Martin L Dunn. The role of van der waals forces in adhesion of micromachined surfaces. *Nature materials*, 4(8):629–634, 2005.

[91] Kellar Autumn, Yiching A Liang, S Tonia Hsieh, Wolfgang Zesch, Wai Pang Chan, Thomas W Kenny, Ronald Fearing, and Robert J Full. Adhesive force of a single gecko foot-hair. *Nature*, 405(6787):681–685, 2000.

[92] Matthias Scherge, Stanislav Gorb, and Stanislav N Gorb. *Biological micro-and nanotribology*. Springer Science & Business Media, 2001.

[93] AK Geim, SV Dubonos, IV Grigorieva, KS Novoselov, AA Zhukov, and S Yu Shapoval. Microfabricated adhesive mimicking gecko foot-hair. *Nature materials*, 2(7):461–463, 2003.

[94] Kevin Kendall. Adhesion: molecules and mechanics. *Science*, 263(5154):1720–1725, 1994.

[95] Ernest Rabinowicz. Friction and wear of materials. 1965.

[96] Heinrich Hertz. Über die berührung fester elastischer körper. 1882.

[97] KL Johnson, K Kendall, and AD Roberts. Surface energy and the contact of elastic solids. In *Proceedings of the Royal Society of London A: Mathematical, Physical and Engineering Sciences*, volume 324, pages 301–313. The Royal Society, 1971.

[98] Boris V Derjaguin, Vladimir M Muller, and Yu P Toporov. Effect of contact deformations on the adhesion of particles. *Journal of Colloid and interface science*, 53(2):314–326, 1975.

[99] D Tabor. Surface forces and surface interactions. *Journal of colloid and interface science*, 58(1):2–13, 1977.

[100] Daniel Maugis. Adhesion of spheres: the jkr-dmt transition using a dugdale model. *Journal of Colloid and Interface Science*, 150(1):243–269, 1992.

[101] KNG Fuller and DFRS Tabor. The effect of surface roughness on the adhesion of elastic solids. In *Proceedings of the Royal Society of London A: Mathematical, Physical and Engineering Sciences*, volume 345, pages 327–342. The Royal Society, 1975.

[102] JA Greenwood and JBP Williamson. Contact of nominally flat surfaces. *Proceedings of the Royal Society of London. Series A. Mathematical and Physical Sciences*, 295(1442):300–319, 1966.

[103] G.A.D Briggs and B.J Briscoe. The effect of surface topography on the adhesion of elastic solids. 10:2453, 1977.

[104] K. N. G Fuller and A D Roberts. Rubber rolling on rough surfaces. *Journal of Physics D: Applied Physics*, 14(2):221–239, February 1981.

[105] Romana Santos, Stanislav Gorb, Valérie Jamar, and Patrick Flammang. Adhesion of echinoderm tube feet to rough surfaces. *The Journal of experimental biology*, 208(Pt 13):2555–67, July 2005.

[106] P.R. Guduru and C. Bull. Detachment of a rigid solid from an elastic wavy surface: Experiments. *Journal of the Mechanics and Physics of Solids*, 55(3):473–488, March 2007.

[107] Haneesh Kesari, Joseph C Doll, Beth L Pruitt, Wei Cai, and Adrian J Lew. Role of Surface Roughness in Hysteresis during Adhesive Elastic Contact. *Philosophical magazine letters*, 90(12):891–902, December 2010.

[108] B. N. J. Persson and E. Tosatti. Qualitative theory of rubber friction and wear. *The Journal of Chemical Physics*, 112(4):2021, 2000.

[109] B N J Persson. Adhesion between an elastic body and a randomly rough hard surface. *The European physical journal. E, Soft matter*, 8(4):385–401, July 2002.

[110] P.R. Guduru. Detachment of a rigid solid from an elastic wavy surface: Theory. *Journal of the Mechanics and Physics of Solids*, 55(3):445–472, March 2007.

[111] Haneesh Kesari and Adrian J. Lew. Adhesive Frictionless Contact Between an Elastic Isotropic Half-Space and a Rigid Axi-Symmetric Punch. *Journal of Elasticity*, 106(2):203–224, March 2011.

[112] JS McFarlane and D Tabor. Relation between friction and adhesion. *Proceedings of the Royal Society of London. Series A. Mathematical and Physical Sciences*, 202(1069):244–253, 1950.

[113] Manoj K Chaudhury and Michael J Owen. Adhesion hysteresis and friction. *Langmuir*, 9(1):29–31, 1993.

[114] Shinji Yamada and Jacob Israelachvili. Friction and adhesion hysteresis of fluorocarbon surfactant monolayer-coated surfaces measured with the surface forces apparatus. *The Journal of Physical Chemistry B*, 102(1):234–244, 1998.

[115] Kenneth Langstreth Johnson and Kenneth Langstreth Johnson. *Contact mechanics*. Cambridge university press, 1987.

[116] Augustus Edward Hough Love. *A treatise on the mathematical theory of elasticity*. Cambridge University Press, 2013.

[117] F Heslot, T Baumberger, B Perrin, B Caroli, and C Caroli. Creep, stick-slip, and dry-friction dynamics: Experiments and a heuristic model. *Physical review E*, 49(6):4973, 1994.

[118] A Majumdar and CL Tien. Fractal characterization and simulation of rough surfaces. *Wear*, 136(2):313–327, 1990.

[119] Benoit B Mandelbrot. *The fractal geometry of nature*. Macmillan, 1983.

[120] Arunava Majumdar and Bharat Bhushan. Role of fractal geometry in roughness characterization and contact mechanics of surfaces. *Journal of Tribology*, 112(2):205–216, 1990.

[121] Y.Z Hu and K Tonder. Simulation of 3-d random rough surface by 2-d digital filter and fourier analysis. 32(1):83–90, 1992.